New Aspects in Limestone Dissolution for Wet Flue Gas Desulfurization

Claudio A. Carletti G.

PhD Thesis in Process Design and Systems Engineering
Faculty of Science and Engineering
Åbo Akademi University

Åbo, Finland 2015

New Aspects in Limestone Dissolution for Wet Flue Gas Desulfurization

Claudio A. Carletti G.

PhD Thesis in Process Design and Systems Engineering
Faculty of Science and Engineering
Åbo Akademi University

Åbo, Finland 2015

ISBN 978-952-12-3281-7
Painosalama Oy
Åbo 2015

To the memory of Giuseppe & Paolo Carletti, and to Gustavo Guerrero

Preface

The present work was carried out at the Process Design and Systems Engineering Laboratory, Åbo Akademi University, under the supervision of Professor Tapio Westerlund and Docent Cataldo De Blasio during the period 2012-2015. A research visit to Bologna University, Italy, was also carried out during January-July 2013 at the Department of Civil, Chemical, Environmental and Materials Engineering (DICAM).

It is with my deepest gratitude that I would like to acknowledge Professor Tapio Westerlund for giving me the opportunity to work during this period at the Process Design and Systems Engineering Laboratory. Professor Tapio Westerlund and Docent Cataldo "Dino" De Blasio are gratefully acknowledged for their support and guidance throughout the years I have spent at ÅAU. I am grateful to Professors Giuseppina Montante and Alessandro Paglianti from Bologna University for their guidance and for inviting me to spend a research period at the DICAM laboratory. Full time research would not have been possible without financial support, therefore the Graduate School in Chemical Engineering is gratefully acknowledged (GSCE, 2012-2015). The Walter Alström Foundation is as well acknowledged.

In addition, I would like to acknowledge Professor Tapio Salmi, Professor Dmitry Yu. Murzin and Docent Henrik Grénman, for their collaborative work. I would like to express my gratitude also to Frej Bjondahl, Jarl Ahlbeck, Lauri Järvinen, Professor Ron Zevenhoven, Professor Olav Eklund, Professor Hannu Toivonen, and Professor Henrik Saxén, who have also been related directly or indirectly to this work, also Kurt Lundqvist is thanked for experimental guidance and help. Jan Kronqvist is acknowledged for his help as well as Professor Frank Pettersson for his fruitful advice. Ermei Mäkilä, Sten Linholm and Linus Silvander are as well acknowledged for their collaborative work. Andreas Lundell, Anders Skjäl, Mikael Nyberg, and Daniel Legendre are thanked for their tips and help.

I would like to thank my friends at “AST”, and “RT" who have collaborated; Otto, Axel, Mikael, for their support, help, time spent during "kaffepaus" both discussing academic-related matters and sometimes less relevant but nonetheless also interesting issues. Special thanks also to Jürgen, Juan Pablo, Jon San Juan, Gerson, Heidi, David, Heini, Sonja, Mika, Mikko, Virpa, Alice, to my friends at the DICAM laboratory, to my cousin Daphne, and to many more whose friendship has contributed to make this possible.

I would like to acknowledge my former Professors from my “alma mater”, Universidad Simón Bolívar, Venezuela. Special thanks to Professors Ursula Ehrmann, Sabrina Di Scipio, María Gabriela Gómez, and Alexis Bouza, who contributed even before the beginning of this work.

My warmest gratitude goes to my parents and family for their love and endless support and to my brother Riccardo, whose sailing endeavors and Atlantic crossings have always inspired me: TFDWYT!

And lastly but most importantly, I thank my girlfriend Oona for her love and patience, kiitos kaikesta!

Åbo, September 2015

Claudio A. Carletti G.

Svensk sammanfattning

Fortsättningsvis tillgodoses största delen av världens energibehov genom förbränning av fossila bränslen, dessutom forsätter världens totala energibehov att öka. Eftersom förbränning av fossila bränslen som t.ex. olja och kol orsakar utsläpp av svaveldioxid som är skadligt för både människa och natur, finns det fortfarande ett akut behov av forskning och utveckling av metoder för svavelrening. De vanligaste teknikerna för svavelrening är våt- och semitorrskrubbning, där svaveldioxiden absorberas av en skrubbervätska. Det är allmänt känt att våtskrubbning är en av de effektivaste teknikerna för svavelrening både ekonomiskt och tekniskt sett samt den mest använda. Våtskrubbningsprocessen har dock flera nackdelar, som dess höga vatten- och energiförbrukning. I större kraftverk går ca 1-3% av dess eleffekt åt till rökgasreningsprocessen, vilket kraftigt motiverar utveckling av nya reningsprocesser samt effektivering av existerande reningsanläggningar. Skrubbervätskan som till huvudsak består av vatten innehåller vanligtvis även kalcium vars syfte är att binda svavlet. Kalciumet kan tillsättas i flera former varav bränd kalk och kalksten är de vanligaste. Kalksten används ofta i svavelreningsprocessen p.g.a. dess låga pris och för att den ger upphov till den användbara biprodukten gips.

Kalkstenens upplösningshastighet är en de av faktorer som kraftigast påverkar reningsprocessen. En detaljerad experimentell karakterisering och analys av kalkstenspartiklar i fast form och i vätskeform har utförts i detta arbete. En experimentell metod för att studera kalkstenens upplösningshastighet vid låg till obegränsad massöverföring har även utvecklats i detta arbete. Metoden möjliggör identifieringen av systemoberoende kinetiska parametrar, vilka kan användas för att undersöka reningsprocesser samt för att planera nya reningsanläggningar. Kinetiska modeller utvecklades genom att använda kalkstenpartiklars specifika yta, som mättes genom kväveadsorption. För att uppskatta specifika ytan görs ofta antagandet att kalkstenspartiklarna är sfäriskt formade. Mätningarna med kväveadsorption resulterade dock i en större specifik yta än den som fås med antagandet om sfäriska partiklar. Partiklarna visade sig också vara icke porösa vilket ledde till slutsatsen att den större specifika ytan beror på en grov och ojämn yta. även dynamiken för högdensitets blandningar av vätska och fasta partiklar undersöktes experimentellt. Efter att de kinetiska parametrarna bestämts experimentellt utvecklades en skrubbermodell för att kunna minimera elförbrukningen av en i driftvarande skrubber. Skrubbermodellen användes för att formulera ett optimeringsproblem vars lösning ger driftparameterar som ger minimal elförbrukningen. Detta komplicerade optimeringsproblem löstes med deterministiska metoder i programpaketet GAMS. Från

lösnigen framgår att elförbrukningen kan minskas genom att mala kalkstenen till lagom stora partiklar vilka ger en tillräcklig specifika yta. Resultaten indikerar att partikelstorleken som ger en tillräcklig specifik yta beror direkt på egenskaper hos stenmaterialet. Från resultaten framgår att elenergi kan sparas genom att inte mala kalkstenen mer än nödvändigt.

Från resultaten i denna avhandling framgår att upplösning av kalksten kan undersökas under förhållanden där upplösningshastigheten inte påverkas av extern massöverföring vilken i sin tur beror på omblandningen. Genom att kombinera experimentellt bestämda modeller med matematisk optimering erhölls en djupare insikt i hur olika råmaterial påverkar processen och hur driftparameterar bör justeras för att minska elförbrukningen.

Contents

List of Figures

List of Tables

CHAPTER 1

Introduction

The impact that mankind has had on the environment through industrialization, is worrying, especially due to the evidence on climate change. One of the consequences attributed to climate change is global warming, however, this is a subject that could be deeply discussed but is outside the scope of this thesis. Nonetheless, some facts cannot be neglected, one of these facts being the enormous amount of gaseous emissions produced as residue of anthropogenic activities. The annual SO_2 emissions have been estimated to be approximately 160 million tons out of which roughly half are product of industrial activity [Stultz and Kitto, 2005]. It has been estimated by the World Coal Institute that in 2005 the most common energy sources were fossil fuels having a share of 34.3% oil, 25.1% coal and 20.9% gas [Shafiee and Topal, 2008]. The industrial sectors that contribute the most to the SO_2 emissions, are the metallurgical ore refining and the power industry that use sulfur-containing fuels as raw material. It has been claimed that coal represents about 70 % of the proven fossil fuel resources [Franco and Diaz, 2009]. In spite of the important and necessary efforts that have been made to introduce competitive clean and renewable energy sources in the market, it has been estimated by the International Energy Agency that by 2030, only 14% of the worldwide energy demand will be satisfied by renewable energies while 83% of the demand will still be supplied by fossil fuels [Shafiee and Topal, 2008]. It has been stated that because coal will likely remain as one of the principal sources of primary energy, due to its low cost among other factors, it will have an important role in medium-to-long term production of energy. As it is well-known, coal is classified as an "unclean" technology because coal burning produces SO_2, NO_x, particulate matter plus approximately 800 g of CO_2 per kWh produced [Franco and Diaz, 2009].

Sulfur dioxide emissions are harmful both to the environment and to human health. Acid rain is produced mainly by NO_x and by SO_2 oxidation in the atmosphere. The pH of rain is naturally acidic, of about 5.7, due to the equilibrium of carbon dioxide and carbonic acid (liquid phase) in the atmosphere. Even though no pH value has been

established as the minimum threshold for rain to be considered acidic, it has been stated by the authorities that rain starts to be an environmental hazard when its pH drops to about 4.6 [Stultz and Kitto, 2005]. Acidic rain causes known negative effects such as deterioration of natural water systems, crop yield reduction, damaging of sculptures and buildings among others. Furthermore, SO_2 in the atmosphere can be harmful to humans by affecting the respiratory tract when present at high concentrations. It has been reported that in several episodes, in Europe and the USA during the 1900s, industrial waste has been presumably the cause of death of tens, possibly thousands of people [Manahan, 1999], the SO_2 concentrations were as high as 38 ppm when its normal concentration in the atmosphere is estimated to be between $10^{-5} - 10^{-4}$ ppm [Seinfeld, 1986].

Factories, power plants, and companies in general may pollute lakes, rivers, oceans and the atmosphere because these goods (water, and air) have no market price, hence, their are treated as free. The effect of economic activities that do not have a market price are not reflected in economic decisions, and are known in economics as externalities. Therefore, it is the government that is required to enforce pollution control, hence, creating what is known as a negative externality to ensure that companies pollute less; this control is achieved through fines, regulations and/or pollution taxes [Chang, 2014]. Even though preserving the natural environment may seem obvious, to some people, given that it is of paramount importance to the current society as well as future generations, it is only through negative externalities that pollution control can be enforced. In the United States, a control regulation for SO_2 emissions was introduced by amendments to the Clean Air Act in 1970, 1977 and 1990. Furthermore, in Japan, the Stationary Emission Standards of 1970 introduced the first emission regulations while in the Federal Republic of Germany an SO_2 Emission Regulation directive was introduced in 1983. Most of the industrialized countries as well as some developing countries have adopted emission regulations since the 1980s [Stultz and Kitto, 2005]. It has been estimated that for the period 1980-2004, the contribution of European emissions to the global SO_2 emissions were halved within this 25 year period [Vestreng et al., 2007]. Figure 1.1 presents the data reported by Vestreng et al. [2007] for the SO_2 emissions of some European countries, the data report errors between 3-25 %.

1.1 Aim of the work

A considerable amount of research and development has been devoted in the past 30-40 years to SO_2 emission regulation and control and, research in these topics is still highly encouraged. This is due to the fact that, as aforementioned, the trends in fossil fuel consumption will not decrease in the near future as it is estimated that energy demand will continuously increase [Shafiee and Topal, 2008]. Furthermore, it has been estimated that the power consumed by the OECD countries to reduce sulfur dioxide emissions during one year (2011) is in the order of a magnitude of 64 TWh, and this consumption figure is comparable to the residential power consumed in one year in Finland (2013) (**Paper V**).

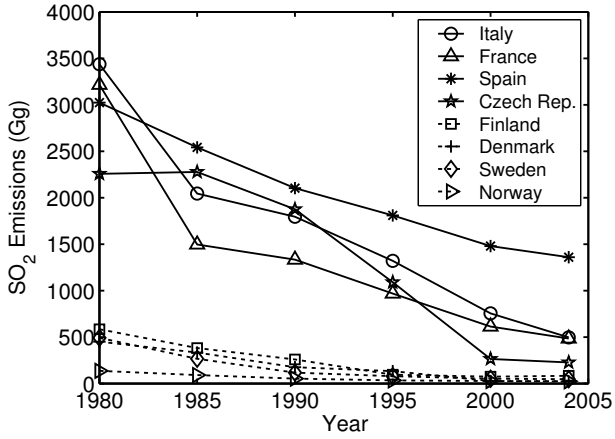

Figure 1.1: Reported SO_2 emissions for the period 1980-2004, data from Vestreng et al. [2007].

Wet Flue Gas Desulfurization (WFGD) technologies have been estimated to provide a removal efficiency rate for SO_2 of 95% or even higher [Srivastava et al., 2001]. In spite of the high removal efficiency of this technology, further research into WFGD has been motivated by the considerable amount of power consumed in the scrubber operation, which can be up to 2% of the total in a 500 MWe power plant [Stultz and Kitto, 2005] or even up to 3% in some cases [Hrastel et al., 2007]. It is thus evident that any improvement in the operation of this technique regarding power efficiency or water consumption is highly motivated considering the trends in the usage of sulfur-containing fuels in the near future.

The aim of this work was to attain a deeper understanding of the physical and chemical phenomena involved in limestone dissolution, which has been regarded as one of the rate determining steps in WFGD applications. More precisely, limestone dissolution has been acknowledged to be among the most essential kinetics involved in the process [Ukawa et al., 1993]. The main objective was to study the kinetics and mass transfer of limestone dissolution and the mixing dynamics of dense systems. This was in order to apply this knowledge to the optimization of certain parameters in the operation of a WFGD scrubber by minimizing the power consumption of the process. In order to attain the main objective, the work was divided into several parts, including extensive characterization of the limestone samples studied, kinetic and mass transfer modeling, dense-slurry suspension dynamics through Electrical Resistance Tomography (ERT) and deterministic (with both global and local solvers) optimization of a WFGD case-study.

1.2 Structure of the thesis

The thesis is composed of five (5) peer-reviewed articles, and the summary part of the thesis that is intended to provide an explanation of the motivations behind each article as well as indicating the clear connection between them.

The thesis is structured into seven (7) chapters was done with the intention of addressing every aspect of the research, hence some chapters may be dedicated to one topic alone while other chapters are more interconnected. Chapter 2 gives the theoretical background of limestone dissolution and Wet Flue Gas Desulfurization which are covered in **Papers I-III** and **Paper V**. Chapter 3 gives a description of the characterization methods employed to study both the solid and liquid phases reported in **Papers I-III** and **Paper V**. Chapter 4 describes the modeling of chemical kinetics and mass transfer, and also includes a description of the mixing dynamics and mass transfer correlations encompassed in **Papers I-V**. In Chapter 5, solid-liquid suspension dynamics are discussed which concerns all the papers, but more especially **Papers IV, V**. Furthermore, Electrical Resistance Tomography (ERT) which was used to study solids distribution and mixing dynamics of dense systems in **Paper IV** is also presented in Chapter 5. Finally, Chapter 6 describes the case-study and the optimization model developed, it is therefore concerned directly with **Paper V**, however it is also related to **Papers I-III**. Finally, the conclusions of the work are presented in Chapter 7.

1.3 List of publications

Paper I Carletti C., Grénman H., De Blasio C. and Westerlund T. Limestone dissolution study for Wet Flue Gas Desulfurization under turbulent regimes above critical suspension speed. *Computer Aided Chemical Engineering*, Vol. 32, pp. 301-306, 2013.

Paper II Carletti C., De Blasio C., Grénman H. and Westerlund T. On modelling the roles played by diffusive and convective transport in limestone dissolution for wet flue gas desulphurisation. *Chemical Engineering Transactions*, Vol. 43, pp. 2131-2136, 2015.

Paper III Carletti C., Grénman H., De Blasio C., Mäkilä E., Salonen J., Murzin D. Yu., Salmi T. and Westerlund T. Revisiting the dissolution kinetics of limestone–experimental analysis and modeling. *Journal of Chemical Technology and Biotechnology*, available online 9 June, DOI: 10.1002/jctb.4750, 2015.

Paper IV Carletti C., Montante G., Westerlund T. and Paglianti A. Analysis of solid concentration distribution in dense solid-liquid stirred tanks by electrical resistance tomography. *Chemical Engineering Science*, Vol. 119, pp. 53-64, 2014.

Paper V Carletti C., De Blasio C., Mäkilä E., Salonen J. and Westerlund T. Optimization of a wet flue gas desulfurization scrubber through mathematical modeling of limestone dissolution experiments. *Industrial & Engineering Chemistry Research*, available online 30 September, DOI: 10.1021/acs.iecr.5b02691, 2015.

1.4 List of related contributions

1. De Blasio C., Carletti C., Järvinen L. and Westerlund T. Evaluating the Reactivity of Limestone Utilized in Flue Gas Desulfurization. An Application of the Danckwerts Theory for Particles Reacting in Acidic Environments and Agitated Vessels with Archimedes Number Less than 40. *Computer Aided Chemical Engineering*, Vol. 29, pp. 1225-1229, 2011.

2. Järvinen L., Leiro J., Bjondahl F., Carletti C. and Eklund O. XPS and SEM study of calcite bearing rock powders in the case of reactivity measurement with HCl solution. *Surface and Interface Analysis*, Vol. 44, No. 5, pp. 519-528, 2012.

3. De Blasio C., Carletti C., Lundqvist K., Saeed L., Westerlund T. and Fogelholm C.J. Modeling the dissolution of carbonate minerals utilized in Flue Gas Desulfurization scrubbers. A stepwise titration technique applied to low Grashof-Reynolds ratio. *Computer Aided Chemical Engineering*, Vol. 31, pp. 465–469, 2012.

4. Carletti C., Bjondahl F., De Blasio C., Ahlbeck J., Järvinen L. and Westerlund T. Modeling limestone reactivity and sizing the dissolution tank in Wet Flue Gas Desulfurization scrubbers, *Environmental Progress & Sustainable Energy*. Vol. 32, No. 3, pp. 663-672, 2013.

5. De Blasio C., Carletti C., Westerlund T. and Järvinen M. On modeling the dissolution of sedimentary rocks in acidic environments. An overview of selected mathematical methods with demonstration of a case study. *Journal of Mathematical Chemistry*, Vol. 51, pp. 2120–2143, 2013.

6. De Blasio C., Carletti C., Westerlund T. and Mika Järvinen. Step-wise titration of sedimentary rocks utilized in wet flue gas desulfurization with hydrochloric acid under semi-low reaction regime and turbulent conditions. Modeling reaction kinetics in batch stirred reactors. *5th International Conference on Applied Energy ICAE2013*, South Africa, 2013.

7. Carletti C., Montante G., Westerlund T. and Paglianti A. Solid concentration distribution in slurry stirred tanks. *13th International Conference on Multiphase Flow in Industrial Plants MFIP13*, Sestri Levante, Italy, 17–19 September 2014. Oral Presentation.

8. Carletti C., Grénman H., De Blasio C., Salmi T., Murzin D. Yu. and Westerlund T. A novel reactor setup for studying limestone dissolution kinetics. *21st International Conference on Chemical Reactors, CHEMREACTOR21*, Delft, The Netherlands, 22–25 September 2014. Poster presentation.

9. Järvinen L., Leiro J., Bjondahl F., Carletti C., Lundin T., Gunnelius C., Smått J-H. and Eklund O. Characterisation of dolomites before and after reactivity measurement with HCl solution. *Surface and Interface Analysis*, Vol. 47, pp. 284–294, 2015.

10. De Blasio C., Carletti C., Lundell A., Visuri V-V.., Kokkonen T., Westerlund T., Fabritus T. and Järvinen M. Employing a step-wise titration method used under semi-slow reaction regime for evaluating the reactivity of limestone and dolomite in acidic environment. *Submitted to Minerals Engineering*, under revision, 2015.

11. Carletti C., Montante G., De Blasio C., Paglianti A. Liquid mixing dynamics in slurry stirred tanks based on electrical resistance tomography. Submitted to *Chemical Engineering Science*, 2015.

1.5 Contributions of the candidate

Paper I The candidate performed the experimental work and was responsible for the preparation of the samples Wolica (LJJ-16C) and Parainen (LJJ-09C) which were also used in the rest of the work. The sample preparation consisted of crushing, grinding and sieving the samples. The experimental systematic approach was supervised and developed along with the co-authors. Moreover, the particle size distribution (PSD) measurements were done by co-authors. The candidate was mainly responsible for the writing of the manuscript, co-authors were actively involved in in providing suggestions that improved the manuscript.

Paper II The candidate performed the experimental work and was responsible for developing the models presented. Moreover, the candidate also proposed the use of the modified Peclet number, introduced in **Paper IV**, which provided a direct link between the proposed models and the stirring performance. The PSD measurements presented in this article and in the following were performed by the candidate. The candidate was mainly responsible for the writing of the manuscript, co-authors were actively involved in providing suggestions that improved the manuscript.

Paper III The kinetic modeling was developed by the candidate and co-authors, the candidate was responsible for the experimental work regarding limestone dissolution. Moreover, the nitrogen adsorption analysis was performed by the co-authors who also contributed to the interpretation of the results and the link to the model. The candidate was mainly responsible for the writing of the manuscript, co-authors were actively involved in providing suggestions that improved the manuscript.

Paper IV The candidate prepared (by sieving) the particles which were used as the dispersed phase. Moreover, all the experiments were performed by the candidate along with the particle size distribution analysis. The candidate was actively involved in the interpretation of the data on solid axial concentration, the study of the different mixing indexes and the preparation of the tomograms. The co-authors were involved in further analyzing the tomography data by deriving the link between the mixing index and the cloud height. Furthermore, the co-authors also developed the concept of the modified Peclet and the visualization of the iso-surfaces. The co-authors were mainly responsible for the writing of the manuscript,

the candidate was actively involved in providing suggestions that improved the manuscript.

Paper V The candidate was responsible for the experiments in this work and for developing and implementing the kinetic model. Furthermore, the optimization model was developed along with the co-authors who motivated the search of the local and global optimum. Furthermore, the nitrogen adsorption analysis was performed by the co-authors along with the correct interpretation of the data. The candidate was mainly responsible for the writing of the manuscript, co-authors were actively involved in providing suggestions that improved the manuscript.

CHAPTER 2

Theoretical background

Several methods have been adopted in power plants that are fired with sulfur-containing fossil fuels to control emissions of SO_2 since the introduction of the first emissions regulations in the 1970s-80s. Among the variety of methods used, the most important are classified according to Kaminski [2003] in:

- Switching of fuel or fuel blending
- Preparation of coal
- Modernization of the boiler
- Change of technology
- Flue gas desulfurization

Of the above-mentioned methods, Flue Gas Desulfurization is regarded as one of the techniques applied most often. More precisely, it has been reported that Wet Flue Gas Desulfurization (WFGD) accounts for approximately 87% of the industrial capacity installed worldwide [Guelli U. Souza et al., 2010]. This figure has also been estimated to be even higher than 90% [Hrastel et al., 2007]. Moreover, it has been stated that more than 80% of the utilities with installed FGD technology employ a calcium-based non-regenerable sorbent. The most common calcium-based sorbents are lime (CaO) and limestone, (mainly $CaCO_3$), however, ashes containing high amounts of calcium and magnesium have also been adopted as sorbent [Gutiérrez Ortiz et al., 2006]. Limestone has been widely employed for WFGD applications because of its low cost and also because of the possibility of producing gypsum as a by-product; gypsum, has a market value when it contains only low amounts of impurities [Gutiérrez Ortiz et al., 2006].

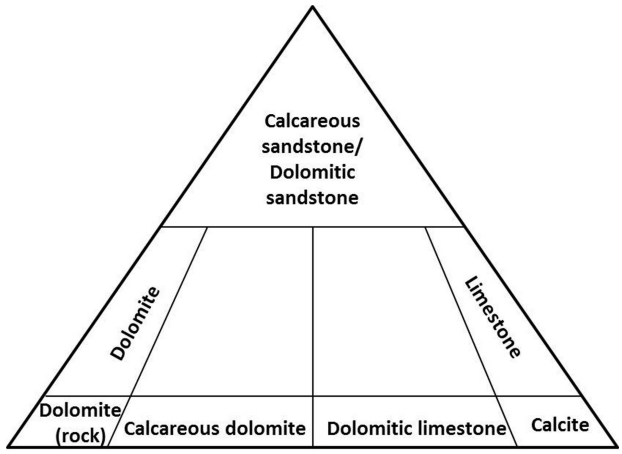

Figure 2.1: Classification of carbonate rocks based on their mineral content, adapted from Tegethoff et al. [2001].

2.1 Calcium carbonate rocks

Calcium carbonate, $CaCO_3$, is a very common compound on Earth, so far it is believed that $CaCO_3$ exists only on Earth and possibly on Mars. The elements that form calcium carbonate are particularly important for organic and inorganic materials on planet Earth and have their origin in the interior of giant stars. Calcium carbonate is a compound that can be present in three different crystal modifications: aragonite, calcite or vaterite. Every mineral variety of $CaCO_3$ is characterized by the fact that they present specific crystal systems, i.e. trigonal for calcite, rhomboid for aragonite and hexagonal for vaterite. The specific densities of these minerals are 2720, 2940 and 2720 (kg/m^3) respectively [Tegethoff et al., 2001]. The densities of the samples used in this work were measured and will be presented in the following chapter, Chapter 3. Based on the specific densities it can be inferred that the main mineral present in the samples is calcite, however, this was also confirmed by X-Ray Diffraction. Limestone can be composed of different minerals and in different proportions; besides calcite, limestone can also be composed of dolomite mineral ($CaMg(CO_3)_2$) which has a trigonal-rhombohedral crystal system.

Limestone can be classified according to different criteria, e.g. according to structure, texture, or carbonate content. A classification of limestone according to the calcite mineral, dolomite mineral and insoluble minerals (such as quartz) content is shown in Figure 2.1 [Tegethoff et al., 2001]. The purity of limestone can be judged according to the calcium carbonate content or the equivalent CaO, for instance, a sample containing >98.5% $CaCO_3$ or >55.2 CaO is classified as a very high purity limestone [Tegethoff et al., 2001]. According to the previous criteria, and the characterization presented in Chapter 3, the samples studied in this work correspond to very high purity samples.

Almost all limestones originate from sedimentation, except carbonatites. Marble, on the other hand, also has a sedimentary origin, however, after being forming by sedimen-

tation it has undergone metamorphism by means of high temperature and/or pressure. Sedimentation has generally two stages, first loose materials are deposited and subsequently during diagenesis the consolidation which forms the rock occurs. The deposits of $CaCO_3$ can be produced by chemical precipitation, organogenic sedimentation or through biochemical processes. The different organisms that are present as carbonate shells are characterized by the different $CaCO_3$ minerals they produce, e.g. calcite with little magnesium is most common in corals and sponges while aragonite is also present in corals, sponges and in mollusks [Tegethoff et al., 2001].

Limestone, or $CaCO_3$ is a very versatile compound, it is a raw material that has become indispensable in the modern world as a filler as well as a coating pigment. It has even been stated that there is hardly an industry that does not depend to a greater or lesser extent on this compound. The list of applications or industries where limestone is employed as a raw material is extremely long. Some examples include: mortar and flooring plaster in the building industry, production of sodium carbonate and calcium carbide in the chemical industry, as rock-dust barriers to increase safety in the mining industry, for fire extinguishing, in explosives, as abrasive material and in flushing liquids for gas and oil drilling holes, in fertilizers, and in chemicals for environmental protection and many others [Tegethoff et al., 2001].

2.2 Wet Flue Gas Desulfurization

Flue Gas Desulfurization (FGD) consists of using certain sorbent(s) to capture the SO_2 from the flue gases. FGD technologies are classified according to the following:

- Semi-dry scrubbing
- Dry scrubbing
- Wet scrubbing
- Regenerable processes

Among these processes, WFGD achieves one of the highest removal efficiencies, as has been mentioned previously. The WFGD method has been acknowledged as being highly reliable [Zhong et al., 2008] and, one of the most effective methods as well as being among the least expensive (to operate) [Olausson et al., 1993]. Furthermore, it has been stated that the efficiency and reliability of this technology has improved considerably in the past 20 years [Dou et al., 2009]. The most common WFGD system is the counter-current spray scrubber; other designs include venturi, mobile packed beds, and static beds [Brogren and Karlsson, 1997]. One of the advantages of the WFGD method in contrast to other methods is the possibility of retrofiting it in operating utilities. A schematic representation of a counter-current WFGD scrubber is presented in Figure 2.2.

In the counter-current spray tower, as in the one shown in Figure 2.2, the flue gases enter from the middle point of the absorber and exit from the top. The absorber is divided into two zones, the upper zone is the absorption zone and the lower zone is

the dissolution/crystallization zone (reaction tank). The scrubbers are self-supported, the diameter varies from 6-24 m and the height reaches up to 46 m [Stultz and Kitto, 2005]. Pulverized limestone, with diameters usually of $< 44\ \mu$m, plus water form the fresh slurry that is pumped into the reaction tank. It is then subsequently recirculated to the upper section where the slurry is sprayed in counter-current mode into the flue gases. The scrubber is a three-phase system where calcium sulphite ($CaSO_3$) and bisulfite ($Ca(HSO_3)_2$) are produced after reacting with the (SO_2) in the flue gas [Gutiérrez Ortiz et al., 2006]. The main components in the absorber are the slurry recirculation pumps, the slurry spray nozzles, the moisture separator, the perforated trays which increase the gas-liquid contact area, the air injection system (in case of forced oxidation) and the tank agitators. The power consumption of some of the previously mentioned components of the WFGD system was studied and minimized by means of optimization in this work (**Paper V**), and the detailed results are reported in Chapter 6.

The following reactions take place in the gas/liquid contact zone [Stultz and Kitto, 2005]:

Dissolution of gaseous SO_2,

$$SO_{2(g)} \rightleftharpoons SO_{2(aq)} \tag{2.2.1}$$

Hydrolysis of SO_2,

$$SO_{2(aq)} + H_2O_{(l)} \rightleftharpoons HSO^-_{3(aq)} + H^+_{(aq)} \tag{2.2.2}$$

Dissolution of limestone,

$$CaCO_{3(s)} + H^+_{(aq)} \rightleftharpoons Ca^{2+}_{(aq)} + HCO^-_{3(aq)} \tag{2.2.3}$$

Acid-base neutralization,

$$HCO^-_{3(aq)} + H^+_{(aq)} \rightleftharpoons CO_{2(aq)} + H_2O_{(l)} \tag{2.2.4}$$

Stripping of CO_2,

$$CO_{2(aq)} \rightleftharpoons CO_{2(g)} \tag{2.2.5}$$

The following reactions occur in the reaction tank [Stultz and Kitto, 2005]:

Dissolution of limestone,

$$CaCO_{3(s)} + H^+_{(aq)} \rightleftharpoons Ca^{2+}_{(aq)} + HCO^-_{3(aq)} \tag{2.2.6}$$

Acid-base neutralization,

$$HCO^-_{3(aq)} + H^+_{(aq)} \rightleftharpoons CO_{2(aq)} + H_2O_{(l)} \tag{2.2.7}$$

Stripping of CO_2,

$$CO_{2(aq)} \rightleftharpoons CO_{2(g)} \tag{2.2.8}$$

Sulfite oxidation,

$$O_{2(g)} + 2HSO^-_{3(aq)} \rightleftharpoons 2SO^{2-}_{4(aq)} + 2H^+_{(aq)} \tag{2.2.9}$$

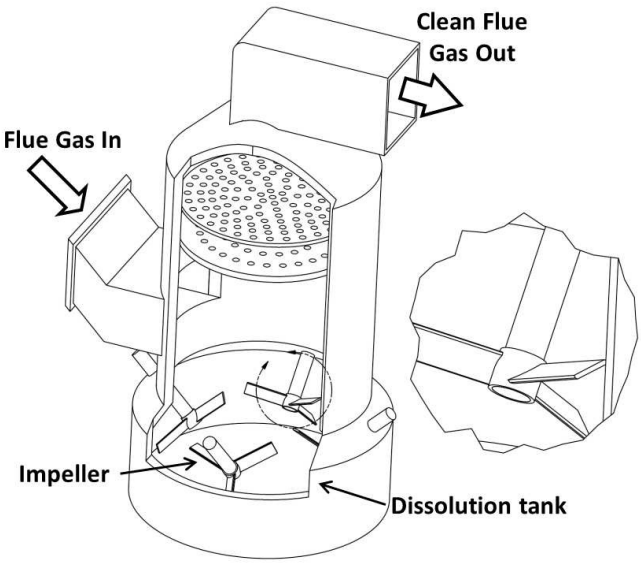

Figure 2.2: Schematic representation of a WFGD scrubber.

Precipitation of gypsum,

$$Ca^{2+}_{(aq)} + SO^{2-}_{4(aq)} + 2H_2O_{(aq)} \rightleftharpoons CaSO_4 \cdot 2H_2O_{(s)} \tag{2.2.10}$$

Finally, the overall chemical reaction in WFGD with forced oxidation can be expressed as,

$$CaCO_{3(s)} + SO_{2(g)} + (1/2)O_{2(g)} + 2H_2O_{(l)} \rightleftharpoons CaSO_4 \cdot 2H_2O_{(l)} + CO_{2(g)} \tag{2.2.11}$$

It has been stated that, the following physico-chemical phenomena represent the rate determining steps within the WFGD process [Bravo et al., 2002]:

- SO_2 diffusion through the gas film
- Dissolution of SO_2 in the liquid
- The first and second dissociation of SO_2
- $CaCO_3$ dissolution
- The diffusion of SO_2 and other ions in the liquid bulk

The inlet flue gas temperature can be between 121 and 177 °C, but after entering the scrubber the gas is cooled to its adiabatic saturation temperature. When the flue gases leave the absorber, also droplets ($< 20\ \mu$m) may be carried along even after going through a moisture separator. The residual SO_2 and the humidity carried in the outlet gas flow, can produce an acidic environment that can damage the stack materials, therefore, the gases are either reheated or the stack is protected with lining materials [Stultz and Kitto, 2005].

2.3 Limestone dissolution

Limestone is a very versatile and abundant material, thus, it is not surprising that it has been studied over the years in a wide variety of fields and under different topics. Limestone can be used to treat metal-acid wastewaters by neutralization through its dissolution [Barton and Vatanatham, 1976], and therefore has been studied when developing in-situ permeable reactive barriers (PRBs) for waste water bioremediation [Gibert et al., 2003]. Commonly, limestone is dissolved in the laboratory by using e.g. HCl or H_2SO_4, however, studies that concern demineralization of bio-polymers which contain $CaCO_3$ have employed additives such as carboxyphosphonates, hydrocarboxilates and polycarboxilates. In such cases, organic additives were employed since the inorganic strong acids would have deteriorated the bio-polymer matrix [Demadis et al., 2008]. The dissolution of calcite deposits in boilers or heat exchangers have been achieved by using additives such as ethylenediamine tetraacetate and hence avoiding the use of strong acids which can damage the equipment [Perry IV et al., 2005]. Calcium carbonate solubility has also been assessed with the intention of anticipating potential scaling problems in oil wells [Coto et al., 2012]. Calcium carbonate dissolution has also been widely studied within the field of geology, e.g. dissolution rates of natural systems have been assessed through modeling dissolution with rotating discs and powder samples [Plummer et al., 1978], [MacInnis and Brantley, 1992]. The relationship between mass transfer mechanisms and surface reaction has been studied in the conditions under Earth's surface for the dissolution of calcite mineral [Berner, 1978]. Comprehensive works have been performed studying carbonate diagenesis of minerals present in limestones such as calcite, dolomite and aragonite [Busenberg and Plummer, 1986]. The equilibrium of the systems $CaCO_3$-CO_2-H_2O [Plummer and Busenberg, 1982], and CaO-CO_2-H_2O [Langmuir, 1968], which are fundamental for understanding carbonate geological behavior in natural environments has also been studied. Furthermore, extensive reviews regarding limestone dissolution studies have been presented [Morse and Arvidson, 2002], [Morse et al., 2007]. According to some review studies, although hundreds of research papers have been written regarding limestone dissolution, there are still some aspects that need to be studied in more detail [Morse and Arvidson, 2002]. Differences between laboratory results and field dissolution of minerals have also been reported. Thus, some authors have looked at the predictability of the dissolution rates [Fischer et al., 2012]. Stochastic approaches have also been presented [Lüttge et al., 2013]. It has been stated that some studies measured rates of diffusion instead of surface kinetics as reported [Lund et al., 1973], [Williams et al., 1970]. It has been concluded that limestone dissolution kinetics are important or at least appealing due to the carbonate accumulation in marine sediments, geochemical cycles, and the characteristics of the bedrock in petroleum reservoirs [Morse and Arvidson, 2002].

The previously mentioned studies are examples of some of the wide variety of research that has been devoted to the study limestone dissolution within different fields. In the literature, it has been reported that the reactivity of limestone is directly linked to the alkalinity provided its capability to neutralize the acid created during the hydrolysis

of SO_2 [Brown et al., 2010]. Therefore, a variety of studies have dealt with limestone dissolution for WFGD, e.g. the works by Chan and Rochelle [1982], Toprac and Rochelle [1982], Gage and Rochelle [1992], Ukawa et al. [1993], Ahlbeck et al. [1993], Kiil et al. [1998], Shih et al. [2000], Pepe [2001], Siagi and Mbarawa [2009], Altun [2014], to mention some examples. Even though the first studies date back approximately 30 years, the field has remained quite active. This is due to the need for FGD systems to be improved and the need to develop new methods to characterize the absorbent and its reactivity. An example of these types of efforts is the study of the buffering effect that some organic acids (e.g. adipic acid) have, by influencing the pH between the gas-liquid interface and the bulk, thus enhancing the FGD removal efficiency [Eden and Luckas, 1998]. It has been claimed that in some studies the SO_2 removal efficiency was increased from 78% up to 90% by the use of these buffering agents [Frandsen et al., 2001]. Some studies have focused on investigating the dissolution rates of samples with different sources, such as South African samples [Siagi and Mbarawa, 2009], Turkish samples [Hoşten and Gülsün, 2004] and Chinese samples [Xiang et al., 2009] among others. In several works, the inhibition of calcite dissolution has been studied, and it was found that dissolved metals such as scandium, zinc, copper, iron, manganese, and magnesium inhibited the dissolution. Moreover, it has been stated that species such as Al^{3+} and F^- inhibit the process under WFGD conditions [Gage and Rochelle, 1992].

Limestone dissolution modeling has been approached in a variety of ways in the literature. The experimental conditions and methods have also varied, some examples are: dissolution of rotating discs [Bjerle and Rochelle, 1984], [Sjöberg and Rickard, 1985], powder samples suspended in slurries [Morse, 1974], parallel plate method [Williams et al., 1970], free-drift method and pH-stat method [Plummer et al., 1978], step-wise tritation method [Ahlbeck et al., 1993], Atomic Force Microscopy (AFM) [Ruiz-Agudo et al., 2009] and fixed-bed dissolution [Lancia et al., 1997].

The shrinking-sphere model, or 2/3 order kinetics, has been applied in several works [Shih et al., 2000], [Siagi and Mbarawa, 2009], [Sun et al., 2010], [Altun, 2014]. This model assumes that the particles are spherical with smooth surfaces and that the surface of reaction (for an ideal sphere) diminishes as a function of conversion [Levenspiel, 1999]. The film theory model has been used to model limestone dissolving from a rotating cylinder into the bulk [Wallin and Bjerle, 1989]. An alternative theory to the film theory is Danckwert's theory of penetration (originally derived for gas-liquid systems) which has also been adopted for limestone dissolution [De Blasio et al., 2012]. The penetration theory model deals with convective mass transfer plus a chemical reaction and assumes that with a rapid chemical reaction the component will disappear after penetrating only a short distance into the medium of absorption. This theory is also known as the renewal theory since it is stated that mass transfer surface is renewed in a transient mode [Welty et al., 2014]. Furthermore, the transition state theory (TST) has also been applied in mineral dissolution/precipitation and more precisely for limestone dissolution [Schott et al., 2012], [Järvinen, 2015]. The TST, first proposed by Eyring in 1934 is a statistical-mechanical theory used to estimate the rate constant of chemical reactions by addressing a condition of dynamical instability. Firstly, the TST assumes a quasi-equilibrium

Table 2.1: Some activation energy values reported in the literature.

Reference	E_a (kJ/mol)	Experimental
King and Liu [1933]	25	Rotating disc, marble
Sjöberg [1976]	35	Ground sample, calcite, 8<pH<10
Plummer et al. [1978]	8.4	Ground sample, pH<3.5
Chan and Rochelle [1982]	16.7	Ground sample, pH<5
Alkattan et al. [1998]	19 ± 4	Rotating disc, 1<pH<3
Morse and Arvidson [2002]	8-60	Review (calcite)
Gledhill and Morse [2006]	21 ± 1	Calcite powder, pH<6.5
Xiang et al. [2009]	30/21	Presence/absence of sulfite, pH 5.5

between the species formed from the reactants (transition-state species) and secondly, that the concentration of these species does not vary during the reaction [Arnaut et al., 2006]. Generally, limestone dissolution has been modeled as a first order reaction with respect to H^+ for low values of pH [Barton and Vatanatham, 1976], [Plummer et al., 1978] and [Ahlbeck et al., 1995]. The order of reaction has been investigated and under different conditions was found to be close to or approaching one [Fusi et al., 2012]. An important experimental result, which has been reported in several studies, is that the dissolution rate has been found to depend on the degree of agitation [Sjöberg and Rickard, 1983], [Pepe, 2001], [Xiang et al., 2009] and [Fusi et al., 2012]. The above-mentioned result indicates that dissolution is controlled by mass transfer rather than kinetics, this aspect is addressed in this work (**Papers I-III, V**) and it is presented in the following chapters. Furthermore, different apparent activation energies have also been reported for limestone (and dolomite) dissolution, under different experimental conditions, some apparent activation energy values reported in the literature are presented in Table 2.1.

Some studies on calcite dissolution have reported apparent activation energies dependent on pH [Plummer et al., 1978], [Sjöberg and Rickard, 1984b], and for dolomite samples pH-dependent activation energies have also been reported [Gautelier et al., 1999]. An extended version of Table 2.1 is presented in the Supporting Information of **Paper III**. Based on the apparent activation energies found, several assumptions regarding mass-transfer and chemical reaction limitations have been made in the literature. In general, limestone dissolution is separated into different phenomena. Three different regions under which the pH dependence varies, have been proposed according to Plummer et al. [1978] and Sjöberg and Rickard [1984b]. The main conclusion has been to regard limestone dissolution as proportional to the activity of H^+ at low values of pH (generally below pH 3.5 at 25 °C) and that it is controlled by mass transfer at low values of pH while at higher values it enters a transition zone and finally becomes completely controlled by surface kinetics [Plummer et al., 1978], [Sjöberg and Rickard, 1984b]. In this work, it was intended to assess limestone dissolution under a regime where mass transfer (enhanced by means of mechanical agitation) would not control the dissolution, thus, the main idea was to study the kinetics under this regime by coupling both mass transfer and kinetics.

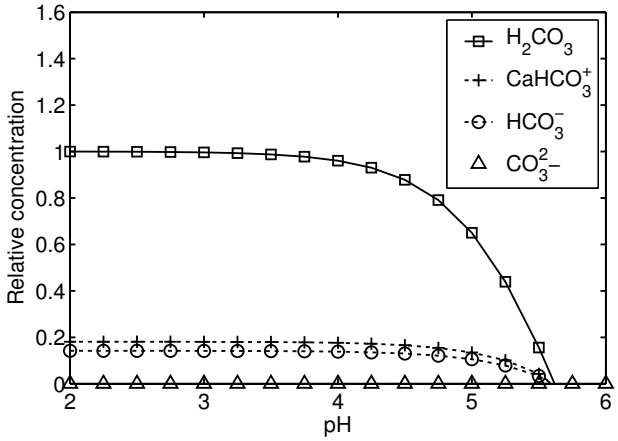

Figure 2.3: Relative equilibrium vs. pH at 25 °C.

The equilibrium concentration of the species involved in limestone dissolution changes as a function of hydronium ion concentration (or pH), as has been shown in the literature [Ahlbeck et al., 1995]. Furthermore, the relative equilibrium concentrations have been calculated for a system with the species: CO_3^{2-}, H_2CO_3, HCO_3^-, $CaHCO_3^+$, and H^+ by using the equilibrium constants derived by Plummer and Busenberg [1982]. The equilibrium curves are shown in Figure 2.3 for a fixed Ca^{2+} concentration of 0.01 M. As can be seen in Figure 2.3, the concentration of H_2CO_3 varies as a function of pH. This is important since it shows that the equilibrium of H_2CO_3 can also influence limestone dissolution and furthermore, that the stoichiometry of the reaction may change with the pH, as is presented in **Paper III**. The following reactions are expected to occur in limestone dissolution [Shih et al., 2000],

$$CaCO_{3(s)} \rightleftharpoons Ca^{2+}_{(aq)} + CO^{2-}_{3(aq)} \tag{2.3.1}$$

$$CO^{2-}_{3(aq)} + H^{+}_{(aq)} \rightleftharpoons HCO^{-}_{3(aq)} \tag{2.3.2}$$

$$HCO^{-}_{3(aq)} + H^{+}_{(aq)} \rightleftharpoons H_2CO_{3(aq)} \tag{2.3.3}$$

$$H_2CO_{3(aq)} \rightleftharpoons CO_{2(aq)} + H_2O(l) \tag{2.3.4}$$

$$CO_{2(aq)} \rightleftharpoons CO_{2(g)} \tag{2.3.5}$$

It can be observed in the reaction scheme for limestone dissolution, reactions (2.3.1)-(2.3.5), that CO_2 is produced, as has already been mentioned, thus, it can influence the pH of the reaction. Therefore, it becomes important to consider the rate at which CO_2 is desorbed in reaction (2.3.5). It has been reported in the literature that the rate of production of CO_2 and H_2O in reaction (2.3.4) is slow, while reactions (2.3.2)-(2.3.3) are instantaneous [Sjöberg and Rickard, 1984a]. Mainly two approaches have been employed in the literature when dealing with CO_2 and the carbonic acid equilibrium. Firstly, it has been claimed that the partial pressure of CO_2 can be maintained in a constant state

by bubbling CO_2 into the solution [Morse, 1974]. Secondly, N_2 has been pumped into the solution also to maintain a constant p_{CO_2} [Chan and Rochelle, 1982], [Toprac and Rochelle, 1982].

In this research work, several aspects regarding limestone dissolution were investigated. Both mass transfer enhancement by means of mechanical agitation and the desorption of CO_2 until achieving a kinetic regime were studied. Furthermore, modeling of the non-ideal surface of the particles, which are non-spherical (as will be shown in Chapter 3) was also performed. Finally, it has been reported in literature that the results derived from dissolution experiments with suspended particles may be subject to considerable uncertainties, due to the complex hydrodynamics of the system [Sjöberg and Rickard, 1983]. In this work, the uncertainties of the complex hydrodynamic system were kept under consideration, and the choice of powder samples was also maintained and motivated in order to emulate the WFGD system.

CHAPTER 3

Characterization

The different characterization methods for both the solid and liquid-phase that have been used during the experimental section of the work are described here. The main methods used to characterize the limestone samples were: Scanning Electron Microscopy (SEM) coupled with Energy Dispersive X-ray Spectrometry (EDX), Inductively Coupled Plasma-Optical Emission Spectrometry (ICP-OES) and Nitrogen adsorption. Nonetheless, information on the mineral phases has also been obtained by X-Ray Diffraction (XRD), and bulk composition was also estimated by X-Ray Fluorescence (XRF). More detailed information on these two methods can be found in a previous work by Järvinen [2015].

The samples employed were chosen since they are both quite pure in $CaCO_3$ but have, at the same time, a different geological background and provenience which is translated into having a different surface morphology and reactivity. Other works have studied a wider variety of samples, as in the work by De Blasio [2010]. However, the preferred choice was to characterize extensively and study two samples with the objective of developing a method that could be applied to other samples as well. The Parainen sample comes from Finland and is a metamorphic sample from the proterozoic age (1900 Ma). On the other hand, the Wolica sample comes from Poland, which has been used for WFGD applications and is a sedimentary limestone from the Jurassic age (150 Ma). Calcite is the main mineral present in the samples studied and this was confirmed by XRD; moreover, a little quantity of the quartz mineral was found in the Parainen sample [Järvinen et al., 2012]. The bulk composition (wt %) of the main metal oxides present in the samples along with the sample density and the total $CaCO_3$ composition was estimated by means of the ASTM C602 standard; these are presented in Table 3.1. The sample densities were measured with a helium pycnometer by means of the volumetric displacement method down to $\pm$ 1 (kg/m^3).

Table 3.1: Sample type, XRF composition (wt%), ASTM C602 $CaCO_3$ content, and density.

Sample	CaO wt%	MgO wt%	SiO wt%	Al_2O_3 wt%	$CaCO_3$ %	ρ (kg/m^3)
Parainen	54.5	0.59	0.5	0.13	98.5	2720
Wolica	55.2	0.32	0.05	0.01	99.1	2703

3.1 Surface morphology and composition

In this study, the surface of the particles has been investigated by means of Scanning Electron Microscopy (SEM) which consists of striking the surface of the samples with a high-energy electron beam and scanning a part of the backscattered or secondary electrons. At the same time, X-rays are produced and can be analyzed, thus providing a non-destructive means of measuring the sample's surface on the micrometer scale [Gill, 1997]. Moreover, X-ray Photoelectron Spectroscopy (XPS) has also been used in studies related to this work to characterize limestone and dolostone surfaces [Järvinen et al., 2012], [Järvinen et al., 2015].

3.1.1 Scanning Electron Microscopy

The Scanning Electron Microscope produces an electron beam from the tip of a tungsten filament at approximately 2400 °C, and subsequently this strong electric field, which is the result of a high voltage difference, accelerates the electrons converting the electron cloud into a divergent electron beam. The SEM image is produced by forming a convergent electron beam that strikes the surface of the sample, which is attained by means of two to four cylindrical electromagnets (magnetic lenses) [Gill, 1997]. After striking the specimen with the electron beam, three type of electrons are emitted, and the SEM images are the result of the scanning of the electron beam and detecting the

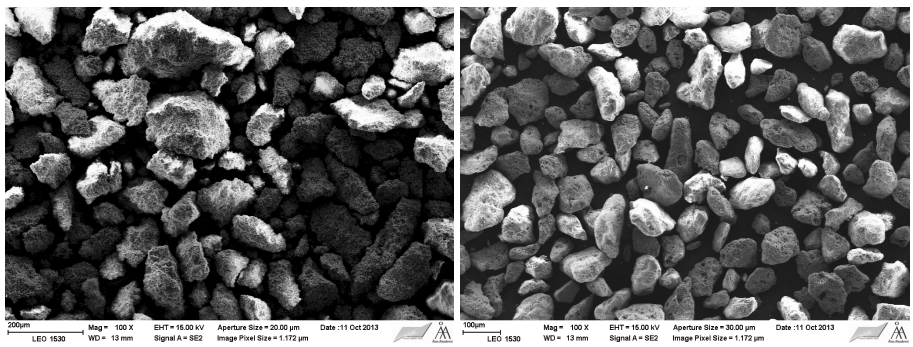

(a) Wolica small unreacted **(b)** Wolica small 30% conversion

Figure 3.1: SEM image (100x) of the small size fraction of the Wolica sample, before (a), and after reaction for 30% conversion (b).

backscattered or secondary electrons [Järvinen, 2015]. The samples are analyzed in a vacuum chamber in order to avoid collision between the electron beam and air molecules. Some examples of the SEM images before and after reaction for the Wolica sample and for different conversions (free-drift method, **Paper III**) are shown in Figures 3.1 and 3.2.

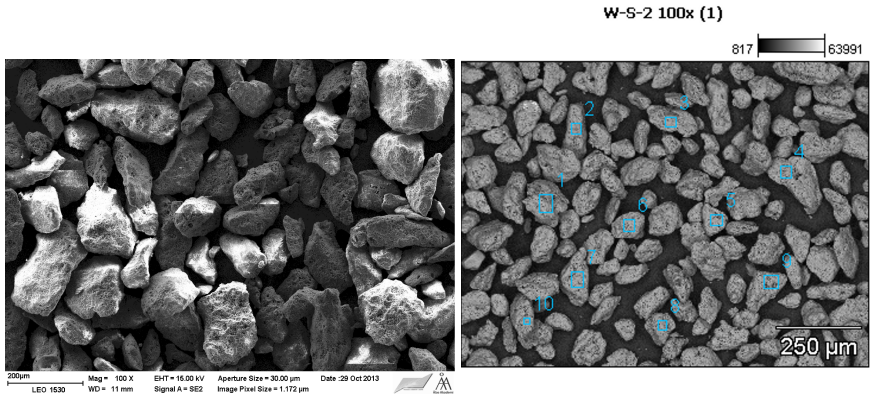

(a) Wolica small 60% conversion **(b)** Wolica small, EDX

Figure 3.2: SEM image (100x) of the small size fraction of the Wolica sample, after reaction 60% conversion (a), and SEM image for EDX (b).

The SEM images in Figure 3.1 indicate that the surface on the particles is rough and irregular, and some elongation can also be observed. The surfaces seem to become smoother after the reaction, as shown in Figure 3.1(b) and 3.2(a). Some examples of the SEM images before and after the reaction for the Parainen sample and for different conversions (free-drift method, **Paper III**) are also shown in Figures 3.3 and 3.4.

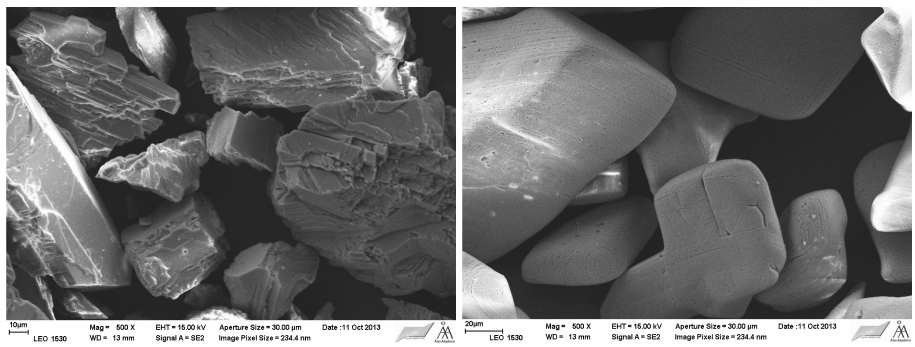

(a) Parainen small unreacted **(b)** Parainen small 30% conversion

Figure 3.3: SEM image (500x) of the small size fraction of the Parainen sample, before (a), and after reaction for 30% conversion (b).

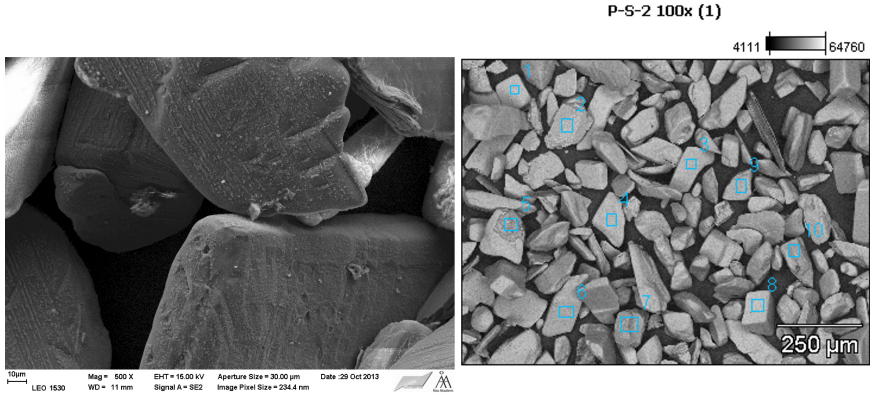

(a) Parainen small 60% conversion **(b)** Parainen small, EDX

Figure 3.4: SEM image (500x) of the small size fraction of the Parainen sample, after reaction 60% conversion (a), and SEM image (100x) for EDX (b).

The morphology of both type of samples differs considerably, this can be confirmed when comparing Figure 3.1 with Figure 3.3. The Parainen samples seem to have euhedral shapes while the Wolica samples are less uniform or more anhedral. Furthermore, the surface roughness of both samples means that there is a greater surface area available for the reaction than if the particle surfaces where spherical, which is the assumption of the shrinking sphere model [Levenspiel, 1999]. The particles are non-porous which has been confirmed by nitrogen adsorption (**Paper III, V**), and will be described in detail in section 3.3. More details about the surface area will be discussed in Chapter 4 and a comparison between surface areas measured by assuming smooth spherical particles and Nitrogen adsorption is presented in Table 3.2.

3.1.2 Energy Dispersive X-ray diffraction

In the Energy Dispersive X-ray diffraction (EDX) method an X-ray spectrometer analyzes the X-rays produced by scanning the surface with the electron beam and translates it into individual peaks of the spectrum. Subsequently, the concentration of the elements can be obtained from the energy peak intensities [Gill, 1997]. An example of an EDX spectra is presented in Figure 3.5, furthermore, examples of the squared areas where the surface composition was analyzed are presented in Figure 3.2 (b) and Figure 3.4 (b).

The kinetic energy of the electrons that hit the samples should be between 15-30 keV in order to produce the required excitation to produce the X-rays. Furthermore, the electrons of the incident electron beam can penetrate into the surface by up to approximately 1 μm in the sample's surface [Gill, 1997]. The depth of the X-ray generation volume depends on the type of sample and elements on the surface. In some cases, the EDX method can measure the composition of the sample up to some nm or even μm into the sample's core.

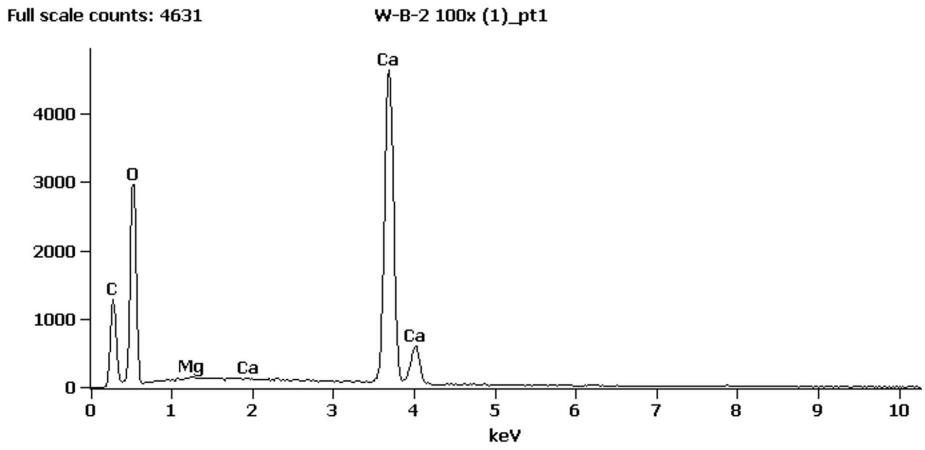

Figure 3.5: EDX spectrum for Wolica large after 30% conversion.

In every EDX measurement 10 squared areas on the samples were analyzed, as can be observed in Figures 3.2 (b) and 3.4 (b). The spectrum presented in Figure 3.5 is the spectra which resulted from the X-rays produced after exiting one of the ten aforementioned squared surfaces. It is also important to consider that the carbon detected in the spectra comes partly from the carbon coating used when preparing the sample, for this reason the results are treated as qualitative results rather than quantitative.

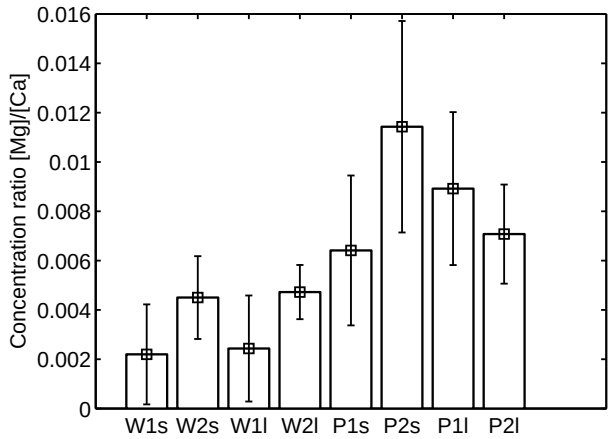

Figure 3.6: Ratios between Mg and Ca compositions at the surface by EDX for Wolica and Parainen small before (W1s, P1s) and after the reaction (W2s, P2s). For Wolica and Parainen large before (W1l, P1l) and after the reaction (W2l, P2l) in the free-drift experiments.

Ratios between Magnesium and Calcium compositions at the surface of the samples before and after reaction can be observed in Figure 3.6, from the free-drift experiments (**Paper III**). The trends found in Figure 3.6 would indicate that the Mg to Ca ratio in-

creases after reaction, which is supported by the fact that calcium is more easily dissolved than magnesium [Järvinen et al., 2012]. It has also been claimed that the presence of magnesium in limestone samples could reduce its reactivity [Hoşten and Gülsün, 2004]. Furthermore, the dissolution rate of limestone (calcite and aragonite) has been found to be 100 times faster than that of dolomite under similar experimental conditions [Busenberg and Plummer, 1986], [Lund et al., 1973]. However, the experimental errors also imply that this trend could be similarly vice-versa, therefore, from these experimental results it can be assured that the ratios remain approximately constant, also by considering the trend in the case of the Parainen large sample (P1l and P2l). Even though the results presented in Figure 3.6 are qualitative, they can be also be compared to the ratios of Ca to Mg measured by means of Inductively Coupled Plasma-Optical Emission Spectroscopy (ICP-OES), which will be described in the following section 3.2. A comparison between composition at the surface and in the bulk of the solution are presented in Figure 3.8.

3.2 Inductively Coupled Plasma-Optical Emission Spectrometry

Inductively Coupled Plasma-Atomic Emission Spectrometry (ICP-AES), also known as Inductively Coupled Plasma-Optical Emission Spectrometry (ICP-OES) is a method which has been established as a one of the most widely used elemental analysis techniques after the 1980s. The ICP-OES method measures the atomic spectra of the elements that are required to be determined. The ICP apparatus is composed of a source unit providing the energy (excitation system), which is commonly composed of argon plasma, the spectrometer, and a computer that converts the signal (spectral lines) produced by the spectrometer into elemental concentrations.

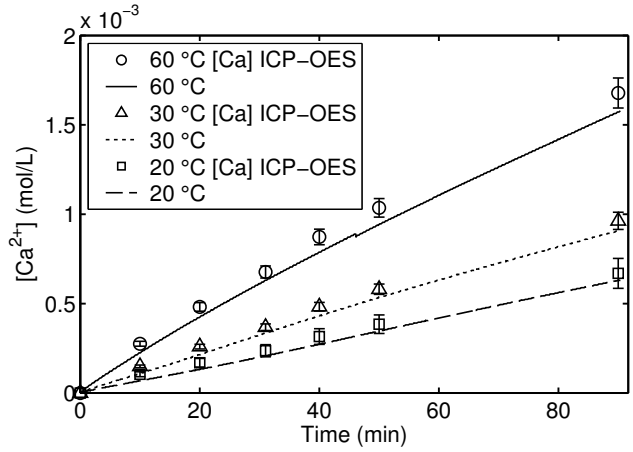

Figure 3.7: ICP-OES measurements of selected points during pH-stat experiments at different temperatures, Parainen small.

The ICP method consists of supplying energy (by the ICP) to the atoms in their ground-state, so that the electrons are then promoted to the higher-energy levels that are vacant. When the atoms return to a lower energy state the effect of the electrons dropping down produces energy which is radiated in the form of a photon. A light of a specific wavelength is generated for each electron drop. The energy that is radiated produces spectral lines that are specific for every element, which leads to the detection of the element [Walsh, 1997]. Selected points were measured by means of ICP-OES, both to estimate the actual stoichiometry of the reaction in the free drift method **(Paper III)** and to confirm the assumed stoichiometry at a fixed pH level **(Paper V)**. An example of the ICP-OES results are presented in Figure 3.7. The ICP-OES results of Calcium and Magnesium compositions in the bulk (solution) were compared to the surface concentrations provided by EDX measurements for the pH-stat experiments, the results are shown in Figure 3.8.

The results presented in Figure 3.7 show a satisfactory agreement between the Ca concentration estimated by means of the ICP-OES method and the curves which were obtained by assuming 2:1 H^+: Ca^{2+} stoichiometry and estimating the dissolved Ca^{2+} from the amount of HCl added. More details on the pH-stat experiments performed to produce the results in Figure 3.7 are presented in Chapter 4. The results presented in Figure 3.8 (**Paper V**) are in agreement with the ones presented in Figure 3.6 (**Paper III**) since the trends indicate an increment in the Mg to Ca ratio. Nonetheless, due to the experimental errors in the measurements this trend cannot be confirmed, thus it can be stated that the ratios before and after the experiments remain approximately constant.

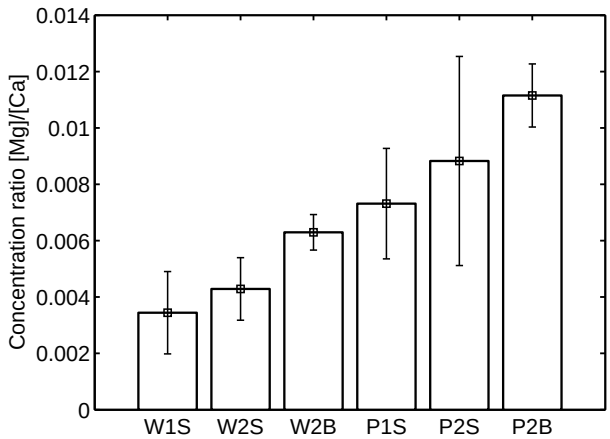

Figure 3.8: Ratios between Mg and Ca compositions at the surface (measured by EDX) for Wolica and Parainen before (W1S, P1S) and after the reaction (W2S, P2S), and in the bulk solution (measured by ICP-OES) for Wolica and Parainen (W2B, P2B).

3.3 Nitrogen adsorption

The nitrogen adsorption method estimates the area and porosity of solid samples by means of adsorbing and desorbing a gas onto the solid's surface. Many gases could be used for this purpose, however, nitrogen has remained the one most commonly applied. The nitrogen adsorption method that is commonly applied today was developed from the work Langmuir conducted on monolayer adsorption. The Langmuir model, also known as the ideal monolayer adsorption model, assumes complete monolayer coverage at the plateau of the isotherm [Sing, 2001]. The Langmuir isotherm was also adapted in this work for modeling solid-liquid reactions (**Paper III**) which will be explained in section 4.4.1. In 1938, the work by Brunauer, Emmet and Teller [Brunauer et al., 1938], provided theoretical support to extend Langmuir's model to multilayer adsorption. Their model introduced an equation, which has since then been widely applied, to estimate surface areas and is known as the BET equation. The method consists in adsorbing nitrogen at 77 K on the sample's surface, the BET model assumes that the first adsorbed layer (monolayer in the Langmuir's model) provides one site for the second and other subsequent layers [Noll et al., 1991]. The equation for the BET isotherm is [Brunauer et al., 1938],

$$\frac{p}{v(p_o - p)} = \frac{1}{v_m C_{BET}} + \frac{C_{BET} - 1}{v_m C_{BET}} \frac{p}{p_o} \tag{3.3.1}$$

where v and v_m are the adsorbed weight and monolayer weight (or monolayer capacity) respectively, C_{BET} is the BET constant, p is the equilibrium pressure and p_o is the saturation pressure at the temperature of measurement. The plot of $\frac{p}{v(p_o - p)}$ against $\frac{p}{p_o}$ should provide a straight line from which the values of v_m and C_{BET} can be estimated [Brunauer et al., 1938]. The BET theory can be applied successfully to a limited range of pressure ratios, where the upper bound has usually been reported as $p/p_o \sim 0.3$ [Sing, 2001]. Subsequently, the surface area, SSA_{BET} can be estimated by means of the equation [Sing, 1985],

$$SSA_{BET} = \frac{v_m N_a \sigma_{BET}}{M_{abs}} \tag{3.3.2}$$

where N_a is the Avogadro's number, σ_{BET} is the effectively occupied area in the complete monolayer ($\sigma_{BET}(N_2)$=0.162 nm^2) [De Blasio et al., 2012] and M_{abs} is the molar mass of the absorbate. The first part of the isotherm, by the inflection point, is used to estimate the surface area by means of the BET equation [Brunauer et al., 1938]. The results presented in Figure 3.9 indicate that for the Wolica sample the SSA remains approximately constant until a 60% conversion, while for the Parainen sample it is approximately constant up to a 30-40% conversion.

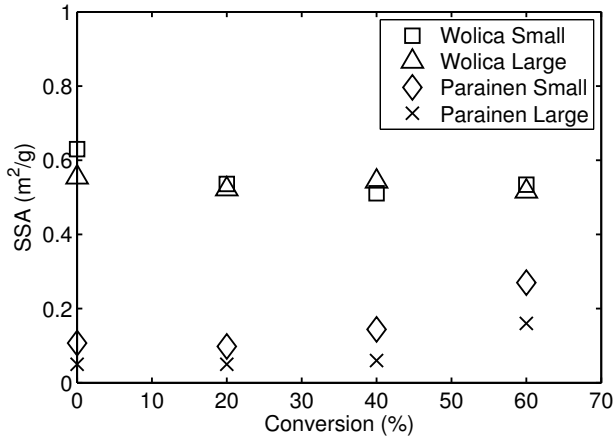

Figure 3.9: SSA Nitrogen adsorption measurements after different conversions. The marker size has been adjusted to include the experimental error of the measurements.

3.4 Particle size analysis by laser diffraction

The dissolution rates of limestone have been regarded as highly dependent on the size distribution of the particles, as this directly affects the Wet Flue Gas Desulfurization Process [Toprac and Rochelle, 1982], [Ukawa et al., 1993], [Ye and Bjerle, 1994], [Sun et al., 2010]. It has been proposed by Gbor and Jia [2004] that implementing or neglecting particle size distribution (PSD) in fluid-solid reactions could result in shifts between finding either chemical reaction or diffusion layer control (in the case of shrinking core model). Particle size distribution (PSD) can be and has been estimated by means of laser diffraction in limestone-water slurry applications. Laser diffraction belongs to the family of "field scanning methods" for particle size measurement. More specifically, laser diffraction is a method that employs low angle laser light scattering to estimate the volumetric distribution of the sample.

Table 3.2: Specific Surface Area comparison and pore volume.

	Wolica small	Parainen small
SSA_{BET}(m^2/g)	0.60	0.105
SSA_{PSD}(m^2/g)	0.0287	0.0217
Pore volume (m^3/g)	<0.002	<0.001

Light striking a particle is partly absorbed, reflected, transmitted and diffracted. The laser diffraction method interprets the scattering patterns of the diffracted light by assuming optically homogeneous and spherical particles. The Mie or Fraunhofer theories are used to perform the deconvolution of the scattering pattern. The Fraunhofer theory assumes that particles are opaque (or assumes that no refraction occurs), and

large with respect to the wavelength of the light employed. The Mie theory is a more refined theory which considers refraction, however, it requires knowledge of both the real and imaginary absorption parts of the refractive index [Allen, 1997]. A typical laser beam employed has a fixed wavelength of 0.63 μm [Rhodes, 1998], and therefore the Frounhofer approximation requires particles to be larger than approximately 25 μm. The working principle of the method relies on the fact that when the laser beam passes through a suspension, the diffraction angle is inversely proportional to the particle size. Modern equipment which use the Mie theory can estimate particle sizes in the range of 0.1-2000 μm [Rhodes, 1998]. Both theories have been employed in this work; the Fraunhofer theory was used in **Paper I**, while the Mie theory was used in **Paper II-V**. Two examples of PSD measurement before and after the reaction (free-drift method, **Paper III**) are presented in Figure 3.10. Furthermore, a comparison between the SSA measured by Nitrogen adsorption and laser diffraction are presented in Table 3.2.

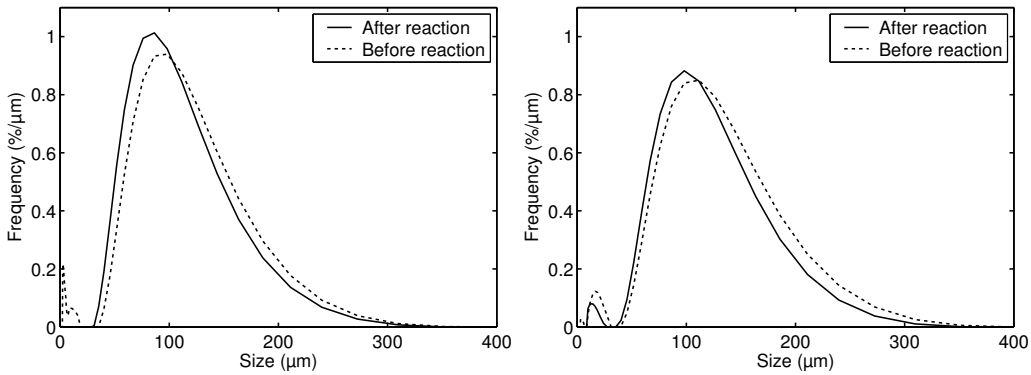

(a) Wolica small **(b)** Parainen small

Figure 3.10: Particle size distribution measured by laser diffraction, before and after experiments (free-drift) for Wolica and Parainen samples

The results presented in Table 3.2 indicate that the surface area measured by means of nitrogen adsorption (SSA_{BET}) is at least one order of magnitude larger than the one estimated by means of PSD (SSA_{PSD}) by assuming spherical and smooth particles. The particles are considered to be non-porous, provided the low porosity values presented in Table 3.2. The fact that the particles are non-porous, implies that there is practically no internal surface area available for reaction. Therefore, it is assumed that the difference between the SSA_{BET} and SSA_{PSD} is due to surface roughness, which can also be seen from the SEM images presented in section 3.1.1. The estimation of particle roughness has been considered earlier in the literature, and a roughness factor (or surface factor) has been proposed as the ratio of the measured surface by gas adsorption and the estimated geometric surface [Sing, 1985]. In this work, a surface factor was implemented for limestone dissolution (**Paper V**) and it is described in detail in Chapter 4.

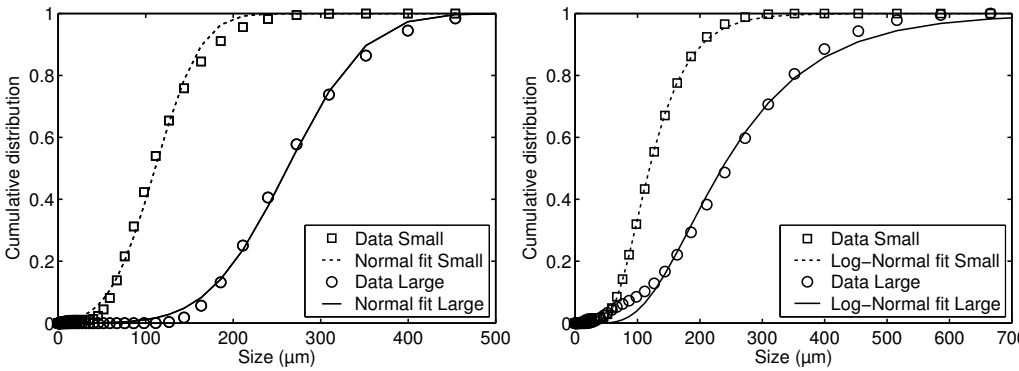

(a) Wolica small **(b)** Parainen small

Figure 3.11: Cumulative PSD and fits measured by laser diffraction, before and after the experiments (free-drift) for the Wolica and Parainen samples

The PSD data has been used in this work to directly estimate the surface areas of the reaction (**Paper V**) or to estimate mean particle sizes. Two types of probability density functions (PDF) have been considered and the cumulative distribution function (CDF) fitted the data. The Normal CDF can be written according to,

$$F(d_p \mid \sigma_1, \mu_1) = \frac{1}{2}\left(1 + \mathrm{erf}\left(\frac{d_p - \mu_1}{\sigma_1\sqrt{2}}\right)\right) \tag{3.4.1}$$

The Log-Normal cumulative density function is a modification of the Normal (or Gaussian) distribution, because of the nature of the logarithmic function, it automatically considers only positive values of the particle sizes. Or in other words, while the Gaussian distribution extends from -∞ to ∞, the Log-Normal distribution goes from 0 to ∞,

$$F(d_p \mid \sigma_2, \mu_2) = \frac{1}{2}\left(1 + \mathrm{erf}\left(\frac{\ln(d_p) - \mu_2}{\sigma_2\sqrt{2}}\right)\right) \tag{3.4.2}$$

where μ_1, μ_2 and σ_1, σ_2 are the characteristic parameters of the PDFs, erf is the error function and d_p is the particle diameter. Fits of the Normal and Log-Normal CDF for the Wolica and Parainen sample before the reaction (**Paper III**) are shown in Figure 3.11. The CDFs, equations (3.4.1) and (3.4.2) were fitted to the data by minimizing the sum of squared errors. As can be seen in Figure 3.11 the fit of both types of CDFs to the data is quite satisfactory. The two CDF were expected to give good representations of the data since in the literature it has been stated that powders produced by grinding should fit Log-Normal distributions, and in the case of a narrow particle size range, also a Normal distribution [Black et al., 1996].

The PSD data was fitted to the CDFs, equations (3.4.1) and (3.4.2), as it has been mentioned above. Furthermore, the Normal probability density function is expressed according to,

$$f(d_p \mid \sigma_1, \mu_1) = \frac{1}{\sigma_1\sqrt{2\pi}} \exp\left(\frac{-(d_p - \mu_1)^2}{2{\sigma_1}^2}\right) \tag{3.4.3}$$

While the Log-Normal probability density function is expressed according to,

$$f(d_p \mid \sigma_2, \mu_2) = \frac{1}{d_p\sigma_2\sqrt{2\pi}} \exp\left(\frac{-\left(\ln(d_p) - \mu_2\right)^2}{2{\sigma_2}^2}\right) \tag{3.4.4}$$

Figure 3.10 shows the data of the PDF.

CHAPTER 4

Modeling

It is very common to encounter solid-liquid reactions in the industry, since a considerable number of chemicals, which are produced world-wide, are obtained through processes involving solid-liquid systems. Some examples of such processes that are often encountered in the industry include: leaching, dissolution of solids, precipitation, and crystalization among others [Atiemo-Obeng et al., 2004]. It has been claimed that one of the factors which contributes to the complexity of fluid-solids systems is that the rates of heterogeneous reactions depend on the surface area available rather than on the solid concentration. Thus, the complexity of these systems lies in the fact that surface area quantification is actually not so straightforward [Salmi et al., 2013]. In addition to temperature and pressure, few parameters can be determined reliably in-situ, therefore it is understandable that important challenges arise when precisely estimating the surface areas which are used for modeling solid-liquid reactions [Grénman et al., 2011]. Because of this challenge, studies concerning solid-liquid reactions rely on the proper determination or estimation of surface areas by indirect methods, based on different models, simplifications, and assumptions.

In this chapter, mathematical modeling of solid-liquid reactions were applied to limestone dissolution, external mass transfer, and chemical reaction on the surface. Diffusion mechanisms have been considered by comparing a model based purely on diffusion with a chemical reaction, and also a two-step model that considers convection. Furthermore, two different methods (explained in Chapter 3) have been applied to estimate surface areas and a surface factor has been derived to account for the non-sphericity of the particles.

4.1 Experimental method

Two methods were employed in the current work to study limestone dissolution, the free-drift (**Papers I-III**) and the pH-stat (**Paper V**) methods where implemented, both

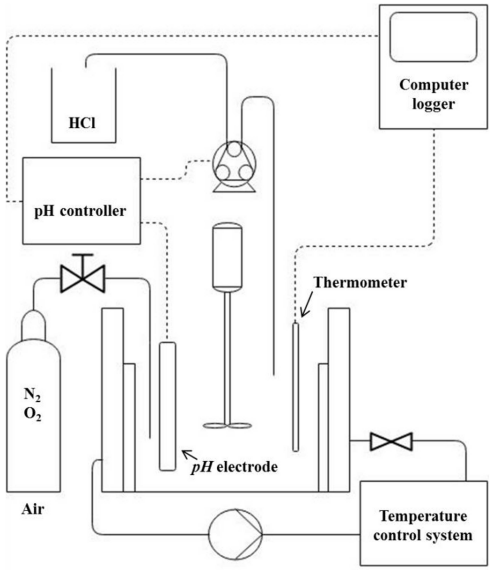

Figure 4.1: Experimental set-up; free-drift, and pH-stat method.

techniques are described by Plummer et al. [1978]. In the free-drift method limestone dissolution is assessed under a transient pH while in the pH-stat method the rates of dissolution are measured at a condition of constant pH. Measurements of pH were used in the free-drift method to assess the dissolution rates, as it has often been presented in the literature [Busenberg and Plummer, 1986], [De Blasio et al., 2012]. In addition to the pH measurements, selected samples were also withdrawn and analyzed with ICP-OES in order to assess the stoichiometry. In contrast, stoichiometry was assumed to be of 2:1 (H^+:Ca^{2+}), as reported in the literature [Chan and Rochelle, 1982], [Gage and Rochelle, 1992], [Shih et al., 2000], [Siagi and Mbarawa, 2009], and compared to the ICP-OES measurements.

The experimental set-up is presented in Figure 4.1 and was used in **Paper I** to estimate the proper stirring speed and air flow-rate under which external mass transfer was enhanced to the point that it would not limit the dissolution. In **Papers II & III**, the dissolution experiments were performed using the free-drift method. The results presented in **Paper V** also include the tests to determine the proper stirring and air-flow conditions along with the pH-stat measurements. The limestone samples were prepared as powders by crushing and grinding; a jaw crusher and vibratory disc mill were employed. After crushing and grinding, the samples were sieved into two fractions of 74-125 μm and 212-250 μm, the fractions will be referred to as small and large fractions respectively. The experimental set-up consisted of a 2L glass reactor with four equally spaced stainless-steel baffles. An electric motor (Janke & Kunkel, max power 70 W) was used to provide mechanical agitation and two type of propellers were used. A three-blade propeller (pumping down) was employed in **Papers I-III** while a 4 blade

PBT turbine (pumping down) was employed in **Paper V**. A pH electrode with a fast response time (double junction with built-in reference, epoxy VWR electrode) was used for both the free-drift and pH-stat methods and connected to a pH meter (EDT Micro 2 and temperature sensor Pt-100 RTD) with automatic temperature compensation and a resolution of 0.001 units of pH. Pressurized air was introduced and the volumetric flow was controlled by a valve while the temperature was controlled down to ± 1 °C (Thermomix 1441 B. Braun). The pH value was controlled in the pH-stat method, down to ± pH 0.1, with a pH controller (Hanna Instruments, HI 504). The calibration of the pH-meter was done by means of pH buffers at 2.00, 5.00, 7.00 and 10.00 for the free-drift method, while for the pH-stat method the pH buffers of 4.01 and 7.01 were used. All calibrations were done at room temperature (23 °C). In the pH-stat method the amount of HCl added into the reaction system was calculated from the weight loss measure by the scale (Precisa 6100 CD) on the beaker containing 0.1 M HCl. As has been mentioned above, both HCl and H_2SO_4 have been employed in limestone dissolution studies. It is important to mention however, that in the present work HCl was used rather than H_2SO_4 in order to avoid precipitation of calcium sulfate which would have interfered with the characterization of the reacted samples.

4.2 Mass transfer and chemical reaction

Mass transfer and chemical reactions are often interconnected and need to be especially considered when dealing with fluid-solid reactions where the mass transfer rates and chemical reaction rates on the solid surface are comparable. In such cases, the reaction rate constant and the mass transfer coefficient can be compared and depending on the ratio between the two, it can be concluded as to whether there is chemical reaction control, diffusion control, or a combination of both. It has been stated that certain experimental conditions can produce such hydrodynamics that the mass transfer coefficient is much

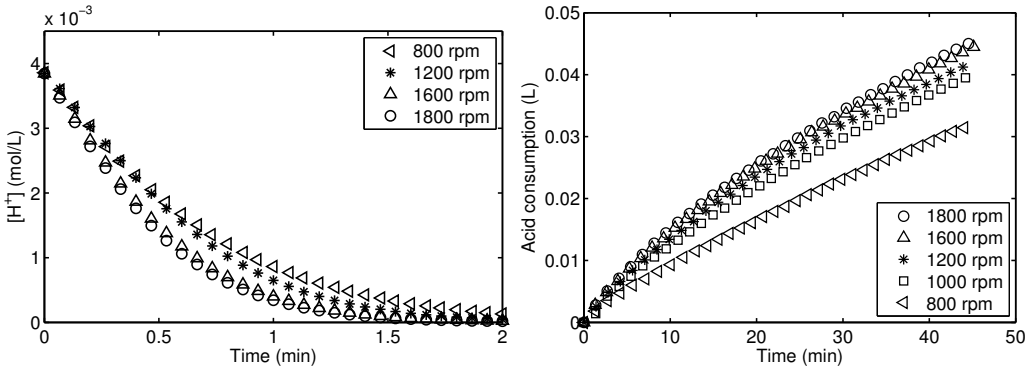

(a) Free-drift method **(b)** pH-stat method

Figure 4.2: Influence of stirring on the dissolution rate, Wolica small.

greater than the chemical reaction constant and the chemical reaction can be assumed to control the rate [Nienow, 1992]. A dimensionless parameter, Da, (the Damköhler number) can be defined as the ratio between the reaction rate constant and the mass transfer coefficient [Davis and Davis, 2012], and in the case of a first order reaction the parameter becomes $Da = \frac{k_r}{k_l}$. The concentration of the species at the surface would therefore approach zero or be approximately equal to the bulk concentration for very small and very large values of Da respectively. Assessment of the controlling role between surface reaction or mass transfer has been presented in the literature for limestone dissolution under Earth's surface [Berner, 1978]. Previously in this study, the author stated that increasing the flushing of a rock does indeed enhance dissolution, and this has also been reported earlier. However, the calculations showed that a limit could be reached after which the flushing rate was no longer the controlling mechanism, instead, the surface chemical reaction started to prevail as the controlling mechanism [Berner, 1978]. On the other hand, some studies report pH as a parameter which can indicate that limestone dissolution is limited by H^+ diffusion, i.e. for pH values of 3∼5 [Ye and Bjerle, 1994]. In the present work, both mass transfer and chemical reaction were considered, as has been mentioned. The aim was to study the hydrodynamic characteristics along with the kinetics in order to assess the controlling mechanism, as in the work by Berner [1978], rather than referring only to the H^+ concentration. The effect of mechanical stirring and air purging on the dissolution rate was assessed experimentally (**Papers I,II, V**), and the results are presented in Figures 4.2, 4.3 and 4.4. The most reactive sample, Wolica small, was employed for these tests at 50°C and 60°C in the free-drift and pH-stat methods respectively. The results in Figure 4.2 show that in both cases the rates were not influenced significantly above 1600 rpm. This stirring speed, was chosen given the technical difficulties encountered when stirring at higher rotational speeds. The results presented in Figure 4.3 were obtained for slower reaction rates than in Figure 4.2 and also for large size fraction and 20 °C.

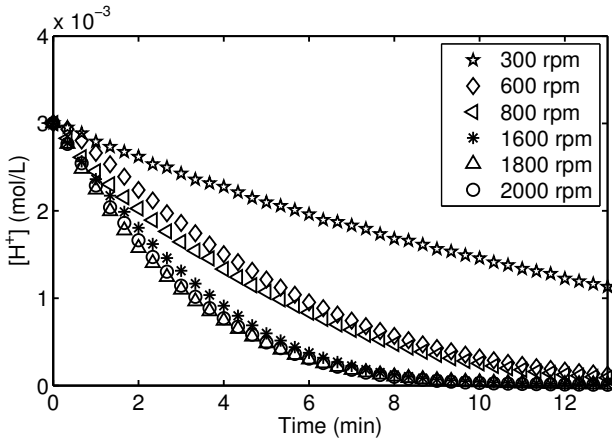

Figure 4.3: Influence of stirring, PBT Wolica sample large size fraction at 20 °C, free-drift method.

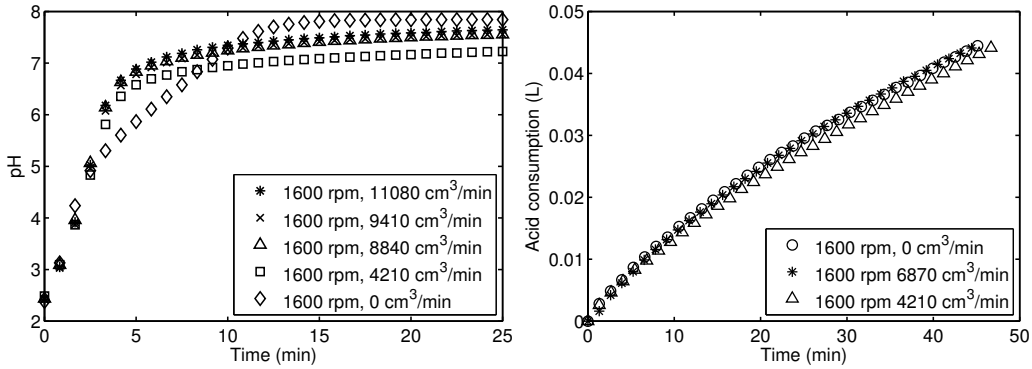

(a) Free-drift method **(b)** pH-stat method

Figure 4.4: Influence of purging on the dissolution rate, Wolica small.

It can also be observed in Figure 4.3, that above 1600 rpm no significant changes in the rates could be observed. It is important to note that the propellers were different in both cases. The smaller particles are expected to react faster, however, due to the proportionality between the mass transfer coefficient and the diameter of the particles, $k_l \propto {d_p}^{-1/3}$, it was expected that for larger particles the mass transfer would be less efficient under the similar conditions. The results in Figure 4.4 show that a flow-rate of 9410 cm^3/min and 4210 cm^3/min, for the free-drift and pH-stat methods respectively, are sufficient to ensure that the rate does not depend on higher flow-rates. It has been reported that smooth particle surfaces with an absence of etch pits present evidence for mass transport controlled dissolution [Berner, 1978]. The presence of etch pitch formation on the surface of the particles can be observed after dissolution from the SEM images presented in Chapter 3. Thus, according to this criterion, the SEM images show evidence of a chemical reaction controlled mechanism.

4.3 Modeling mass transfer

The mass transfer coefficients obtained by means of the theoretically derived Sherwood equations for the laminar and turbulent boundary layer are in good agreement with the experimentally measured values in the case of flat plates. In the case of particles (spherical), the mass transfer coefficients are estimated by semi-empirical correlations which consider both forced convection and molecular diffusion [Welty et al., 2014]. The typical Sherwood correlation, Sh, can be written according to [Welty et al., 2014],

$$Sh = Sh_o + CRe^a Sc^{1/3} \tag{4.3.1}$$

where C and a are the constants to be estimated [Welty et al., 2014]. The Sherwood equation (4.3.1), is also an analogy from heat transfer, where the Prandtl number is substituted by the Schmidt number in the Nusselt equation [Eden and Luckas, 1998].

In the case of a single spherical particle immersed in a stagnant fluid, Sh_o approaches the value of 2 under Stokes regime, and steady state. For the case of the terminal velocity-slip velocity theory a correlation of the Froessling type has been proposed in the literature [Atiemo-Obeng et al., 2004],

$$Sh = 2 + 0.44Re^{1/2}Sc^{0.38} \tag{4.3.2}$$

The Ranz and Marshall equation, which has also been employed in the literature [Levins and Glastonbury, 1972], [Eden and Luckas, 1998], can be applied when considering Kolmogoroff's theory of local isotropic turbulence [Pepe, 2001],

$$Sh = 2 + 0.6Re^{1/2}Sc^{1/3} \tag{4.3.3}$$

Equation (4.3.3) has also been implemented for the absorption zone of the WFGD scrubber [Zhu et al., 2015]. It is noteworthy to mention that Sherwood correlations of the Froessling type can be employed when the settling velocity is larger than 0.0005 m/s [Atiemo-Obeng et al., 2004]. In the present work, the settling velocity was estimated to be around 0.01 m/s, as it is reported in Chapter 5. Sherwood equations have also been derived theoretically for dense spherical particulate beds, which are operated under a steady creeping flow, i.e. low values of Reynolds and large values of Peclet. The theoretically derived equation was obtained by means of the Chilton-Colburn analogy and it has been found to be in good agreement with experimental data on the dissolution of benzoic acid spheres in water [Bird et al., 2007]. This implies that the flow pattern around an isolated spherical particle does not differ significantly when it is surrounded by other particles, especially at the surface where most of the mass transport takes place. The theoretically derived Sherwood equation which also takes into consideration the Stokes regime becomes [Bird et al., 2007],

$$Sh = 2 + 0.991(ReSc)^{1/3} \tag{4.3.4}$$

A Sherwood equation in the form an equation (4.3.4) has also been used previously for limestone dissolution studies [De Blasio et al., 2013]. It was proposed by Temkin [1977], that in cases of a sufficiently high Reynolds number, equation (4.3.1) could be re-written as [Hajek and Murzin, 2004], [Salmi et al., 2011],

$$Sh = {Re_p}^{1/2}Sc^{1/3} \tag{4.3.5}$$

The Sherwood number is calculated according to,

$$Sh = \frac{k_l d_p}{D_j} \tag{4.3.6}$$

where k_l is the mass transfer coefficient, d_p is the diameter of the particle and D_j is the diffusivity of species j. The Schmidt number, gives the ratio of momentum to mass diffusivity and also provides a way to associate the concentration boundary layer with the hydrodynamic boundary layer [Welty et al., 2014],

$$Sc = \frac{\nu}{D_j} \tag{4.3.7}$$

where ν is the kinematic viscosity of the fluid. In the literature, different Reynolds number (e.g. referred to the stirrer, the particles or the vessel) and different Sh correlations have been implemented when studying mass transfer in solid-liquid systems [Boon-Long et al., 1978]. Mainly two theories have been applied; the Kolmogoroff theory of local isotropic turbulence and the terminal velocity-slip velocity theory [Nienow, 1992]. The Reynolds number for the particles from Kolmogoroff's theory is calculated according to [Salmi et al., 2011],

$$Re_p = \left(\frac{\varepsilon d_p^4}{\nu^3} \right)^{1/3} \tag{4.3.8}$$

where ε is the mean dissipated energy. The Reynolds number for the particles from the theory of terminal velocity-slip velocity is calculated according to [Atiemo-Obeng et al., 2004],

$$Re_p = \frac{u_t d_p}{\nu} \tag{4.3.9}$$

The Kolmogoroff theory sates that under large Reynolds number, the smaller eddies that will eventually dissipate into heat because of viscous forces become independent of the motion of the bulk and are isotropic. Furthermore, this theory states that the slip velocity is proportional to the mean dissipated energy and that the diameter of the particle can be used to calculate the Reynolds number when it is smaller than the macro-scale and larger than the Kolmogoroff length scale [Levins and Glastonbury, 1972]. In other words, Kolmogoroff's theory implies that equal power inputs produce equal mass transfer coefficients [Nienow, 1975]. However, some data reported in the literature show that for a given mean dissipated energy value, the mass transfer coefficient was found to be different when the ratio of stirrer to the tank diameter increased [Levins and Glastonbury, 1972]. On the other hand, the terminal velocity-slip velocity theory assumes that the mass transfer coefficient is related to the value that would be obtained for particles moving in a fluid at their terminal (or settling) velocity [Nienow, 1975]. Thus, in the terminal velocity-slip velocity theory the settling velocity is used when calculating the Reynolds number [Atiemo-Obeng et al., 2004]. The Kolmogoroff theory allows for a connection between the power input, which is a function of stirring speed, and the mass transfer coefficient. While in contrast, the settling velocity-slip velocity theory implies equal mass transfer coefficients for different stirring speeds. Nonetheless, it has been acknowledged that despite the fact that the two theories are based on different models they can also be in agreement [Nienow, 1992]. As it has been acknowledged, describing the hydrodynamics of solid-fluid particle systems can be quite challenging [Nienow, 1975], especially because mass transfer does not depend solely on energy distribution but also on the distribution of the solids in the vessel [Levins and Glastonbury, 1972]. The Reynolds number for the vessel is calculated according to [Ibrahim and Nienow, 1995],

$$Re_v = \frac{N D_s}{\nu} \tag{4.3.10}$$

where N is the stirring speed and D_s is the diameter of the stirrer. In this study, the Reynolds number for the vessel was utilized in order to determine the minimum stirring

speed for the turbulent regime in **Paper I** [Ibrahim and Nienow, 1995]. The Zwietering [1958] correlation was used to estimate the critical suspension speed, N_{js}, and it is presented in Chapter 5. It has been suggested that above the critical suspension speed, where all particles are suspended, mass transfer can only be slightly enhanced whereas the power required increases dramatically [Zwietering, 1958], [Calderbank and Moo-Young, 1961]. The previous statement is based on the fact that $k_l \propto N^{\beta}$, where β has been found to be (experimentally) between 0.4-0.6, [Nienow, 1992], and theoretically 0.5 according to Temkin [1977]. On the other hand, the power consumed by stirring increases rapidly provided that $\varepsilon \propto N^3$. Nonetheless, the experiments in this work were performed well above N_{js} (for limestone dissolution) to assure complete suspension, homogeneous distribution of solids and as much turbulence as possible. In this work, the Reynolds number for Kolmogoroff's theory was mainly used (**Papers II-III & V**), a combination of the Kolmogoroff theory and the slip velocity-settling velocity theory was implemented in **Paper V**. The choice of using Kolmogoroff's theory was determined by the fact that it is a widely established theory and more importantly because it provides a direct link between the actual hydrodynamics of the system and the mass transfer coefficient. The combined theories allowed for the coupling of the dissipated energy, the settling velocity of the particles, and the minimum stirring speed constraint required for off-bottom suspension of particles, as reported in **Paper V**.

4.3.1 Diffusion boundary layer

The diffusion boundary layer (DBL) that is formed around the reacting limestone particles has been considered previously in the literature [Gage and Rochelle, 1992], and also in the case of the rotating disc method [Sjöberg and Rickard, 1984b]. In the work by Gage and Rochelle [1992] the DBL thickness was found to be independent of the pH. However, Liu and Dreybrod [1997] reported that the DBL thickness can be adjusted by the rotating disc method. In the present work, in Paper II, a theoretically derived, diffusion boundary layer thickness was applied when modeling the diffusion and chemical reactions on the surface in **Paper II**. The first law of Fick states that in one dimension under steady state the molar flux is given according to,

$$N_j = -D_j \frac{\mathrm{d}c}{\mathrm{d}r} \tag{4.3.11}$$

where r is the spatial dimension of the particle (assumed spherical). Subsequently the molar flow can be obtained by,

$$N_j A = 4\pi r^2 \left(-D_j \frac{\mathrm{d}c}{\mathrm{d}r}\right) \tag{4.3.12}$$

where A is the surface area which is available for diffusion transport. When considering the derivative of the spatial dimension as,

$$\mathrm{d}\left(\frac{1}{r}\right) = -r^{-2}\mathrm{d}r \tag{4.3.13}$$

After substituting equation (4.3.13) into (4.3.12), the expression for the flux becomes,

$$N_j A = 4\pi D_j \left(-D_j \frac{\mathrm{d}c}{\mathrm{d}(\frac{1}{r})} \right) \tag{4.3.14}$$

The integral of the molar flux from the radius R to the boundary layer thickness, $R+\delta$, is calculated according to,

$$N_j A \int_{1/R}^{1/(R+\delta)} \mathrm{d}\left(\frac{1}{r}\right) = 4\pi D_j \int_{c_R}^{c_\delta} \mathrm{d}c \tag{4.3.15}$$

The solution of equation (4.3.15) gives,

$$N_j A = \frac{4\pi D_j (c_\delta - c_R)}{\frac{1}{R+\delta} - \frac{1}{R}} \tag{4.3.16}$$

The mass transfer from the DBL to the particle surface, at distance R from the center, can be also expressed according to,

$$N_j A = k_l 4\pi R^2 (c_R - c_\delta) = \frac{4\pi D_j (c_\delta - c_R)}{\frac{1}{R+\delta} - \frac{1}{R}} \tag{4.3.17}$$

After re-arranging the terms in equation (4.3.17) the expression becomes,

$$\frac{k_l R}{D_j} = \left(\frac{R}{\delta} + 1 \right) \tag{4.3.18}$$

After substituting R as $\dfrac{d_p}{2}$ in equation (4.3.18),

$$\frac{k_l d_p}{D_j} = Sh = 2 \left(\frac{\frac{d_p}{2} + \delta}{\delta} \right) \tag{4.3.19}$$

Subsequently,

$$Sh = 2 + \frac{d_p}{\delta} \tag{4.3.20}$$

Finally, the diffusion boundary layer thickness becomes,

$$\delta = \frac{d_p}{Sh - 2} \tag{4.3.21}$$

From equation (4.3.20) it can be deduced that under stagnant fluid conditions, δ, approaches ∞ and thus Sh approaches the theoretical value of 2. In other words, when δ approaches ∞, Re would approach zero. The theoretically derived thickness for the DBL was implemented in the model with diffusion and chemical reaction, which is explained in the following section 4.3.2.

4.3.2 Diffusion with reaction and two-step model

Diffusion has been regarded as the rate determining step (rds) in limestone dissolution under conditions of low pH, as has been above-mentioned. In order to assess this assumption, a model considering only diffusion from the bulk into the DBL towards the particle surface and chemical reaction was considered and compared with a two-step model which also considers forced convection (**Paper II**). The equation describing the second law of Fick for non-stationary transport with diffusion and the chemical reaction for one dimension can be expressed according to,

$$\frac{\partial c_{H^+}}{\partial t} = D_{H^+}\frac{\partial^2 c_{H^+}}{\partial z^2} - k_r c_{H^+}. \tag{4.3.22}$$

where k_r is the reaction rate constant and D_{H^+} is the diffusion coefficient of the hydronium ions. In order to use equation (4.3.22), the solid was assumed as a semi-infinite body and the direction of H^+ diffusion to be uni-directional. After applying the change of variable $u = c_{H^+}e^{k_r t}$, equation (4.3.22) becomes,

$$\frac{\partial u}{\partial t} = D_{H^+}\frac{\partial^2 u}{\partial z^2} \tag{4.3.23}$$

The general solution to equation (4.3.23) is,

$$\bar{u} = Ae^{-\sqrt{\frac{p}{D_{H^+}}}z} + Be^{\sqrt{\frac{p}{D_{H^+}}}z} \tag{4.3.24}$$

where $\bar{u}$ is the newly introduced variable in the Laplace domain and p represents the frequency. The boundary conditions for both z, t and for z, p, are expressed according to,

$$z = 0, t > 0, p > 0, \bar{u} = \frac{c^o_{H^+}}{p - k_r} \tag{4.3.25}$$

$$z \to \infty, t > 0, p > 0, \bar{u} = 0 \tag{4.3.26}$$

where $c^o_{H^+}$ is the concentration of H^+ at the border of the boundary layer, or at the bulk. At a position which is far from the boundary layer, H^+ tends to zero. Equation (4.3.24) is solved by using the boundary conditions in (4.3.25) and (4.3.26) to find A, B and after anti-transforming the solution from the Laplace domain to the z and t domain, the solution becomes,

$$c_{H^+}(z,t) = \frac{c^o_{H^+}}{2}\left(e^{-\sqrt{\frac{k_r}{D_{H^+}}}\delta}\operatorname{erfc}\left(\frac{\delta}{2\sqrt{D_{H^+}t}} - \sqrt{k_r t}\right) + e^{\sqrt{\frac{k_r}{D_{H^+}}}\delta}\operatorname{erfc}\left(\frac{\delta}{2\sqrt{D_{H^+}t}} + \sqrt{k_r t}\right)\right) \tag{4.3.27}$$

where δ is the DBL thickness which is estimated by applying equation (4.3.21). A similar equation has been presented in the literature for limestone dissolution, however the direction of the diffusion was considered from the particle towards the bulk and the theory of penetration was implemented [De Blasio, 2010].

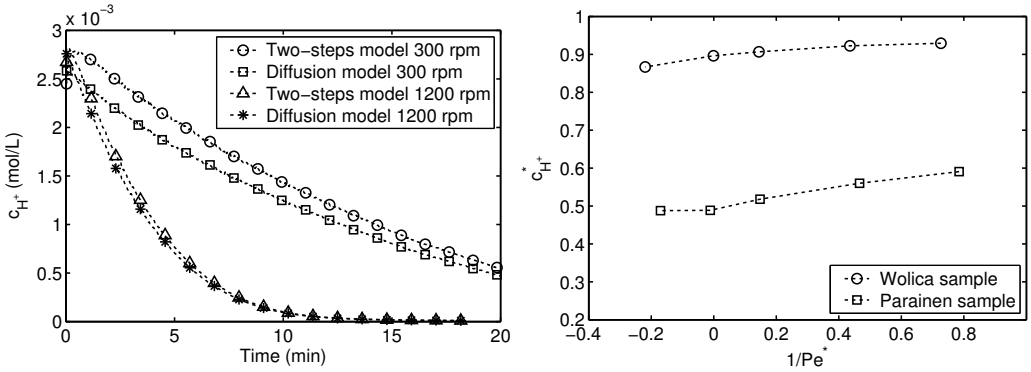

(a) Model comparison **(b)** Convection and Diffusion

Figure 4.5: Model comparison: diffusion with chemical reaction and two-steps model.

Equation (4.3.27) can be used to estimate the concentration of H^+ at a distance δ from the bulk as a function of time, erfc is the complementary error function. However, only diffusion as the mass transport phenomenon has been considered in the model above. A two-step model with first order chemical reaction can be used to estimate the concentration at the solid-liquid interface by estimating k_r after calculating k_l from equation (4.3.3). The estimation of the mass transfer coefficient, k_l, through the Ranz and Marshall equation considers molecular diffusion as well as forced convection [Welty et al., 2014]. The concentration at the interface is calculated according to,

$$c^i_{\mathrm{H}^+} = \frac{k_l c_{H^+}}{k_r + k_l} \tag{4.3.28}$$

where $c^i_{\mathrm{H}^+}$ is the concentration at the solid surface or solid-liquid interface. An example that compares the concentration at the interface found by the two-steps model (equation (4.3.28)) and the diffusion model with chemical reaction (equation (4.3.27)) is presented in Figure 4.5 (a). In order to assess which mass transport phenomenon is dominant, it is important to consider the Peclet number, which is the ratio between the convective and the diffusive transport,

$$Pe = ReSc = \frac{uL}{D_j} \tag{4.3.29}$$

When the convective transport is predominant, i.e. under a turbulent regime, Pe becomes large and diffusion through the DBL might be the rds. However, when Pe is small it implies that also the effect of convective forces as rds might be relevant. This is important since, as it has been reported, in the industry processes are seldom operated under uniform solid distribution or high turbulence given that usually the operating stirring speed is around N_{js} [Tamburini et al., 2013]. A modified Peclet number was introduced in this work and it will explained in more details in Chapter 5.

The introduced Pe for the just suspended speed, Pe^*,is defined according to,

$$Pe^* = \frac{u_t H_L}{D_{es}} \tag{4.3.30}$$

where H_L is the liquid height of the vessel and D_{es} is the relative axial solid dispersion coefficient. Furthermore, a dimensionless concentration, $c^*_{H^+}$ was defined as the ratio between the concentration estimated by the two-steps model and the concentration estimated by the diffusion model with a chemical reaction. The results for the dimensionless concentration as a function of the modified Peclet number are presented in Figure 4.5 (b). The results indicate that when the process is operated at the just suspended condition, N_{js} or $\frac{1}{Pe^*} = 0$, convection may contribute by 10% or up to 50% depending on sample type. Figure 4.5 (a) shows that the two models deviate at low stirring speeds but tend to approach at a high stirring speed. Thus, the results suggest that the convective effect is under estimated by the purely based diffusion model.

4.4 Kinetic modeling

A fundamental aspect of kinetic modeling is determining how certain parameters affect the rates of the reaction or the reactions under study. One of the most important parameters studied is the effect of temperature on the reaction rate. One of the first descriptions of the effect of temperature on the rate constant was given by Arrhenius. The proposed theory assumed that there is an equilibrium between "reactive" and normal "molecules". This law addresses the fact that the effect of temperature on a reaction cannot be explained solely by the effect on the translational energy of the molecules [Arnaut et al., 2006]. The Arrhenius equation is expressed according to [Arnaut et al., 2006],

$$k_r = k_I \mathrm{e}^{\left(\frac{-E_a}{R_g T}\right)} \tag{4.4.1}$$

where k_I is the pre-exponential factor, E_a is the activation energy and R_g is the universal gas constant. The activation energy and the pre-exponential factor can be assumed as being independent from the temperature, as it has been assumed in this work, however, it is know that k_I can also be affected by temperature to some extent [Arnaut et al., 2006]. The following modified Arrhenius equation which minimizes the correlation between the pre-exponential factor and the activation energy was used in this work [Grénman, 2010],

$$k_r = k_I \mathrm{e}^{\frac{-E_a}{R_g}\left(\frac{1}{T} - \frac{1}{T_{mean}}\right)} \tag{4.4.2}$$

The use of the modified Arrhenius model, equation (4.4.2), has been acknowledged to be more efficient than using the original form, equation (4.4.1) [Buzzi-Ferraris and Manenti, 2009]. Other modifications of the original equation have also been proposed in the literature by Buzzi-Ferraris and Manenti [2009], with the objective of balancing the estimated parameters.

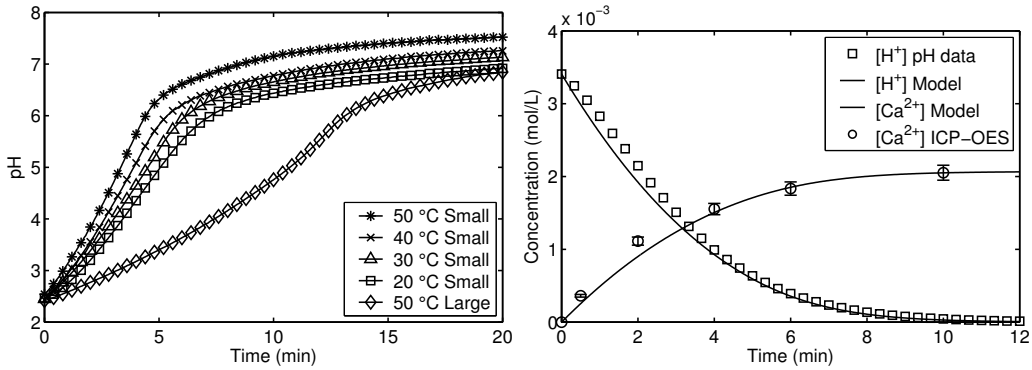

(a) pH vs. time Parainen

(b) Data and model Wolica

Figure 4.6: pH as a function of time, for small size fraction (20, 30, 40, 50 ° C), and large fraction (50 °C), and the modeling results for Wolica large (20 °C).

The chemical kinetics of limestone dissolution was investigated in the present work by assessing the effect that temperature has on the reaction rate constant. Partly because the apparent activation energy is assumed as an intrinsic characteristic of the absorbent and also because knowing the temperature dependence of the reaction is necessary for developing simulation and optimization models, such as the one presented in Chapter 6.

4.4.1 Free-drift method

A model which was able to accurately describe the studied pH region in the free-drift experiments was developed and presented in **Paper III**. The Langmuir adsorption isotherm was implemented to the adsorption on the solid surface under the following assumptions [Noll et al., 1991],

- Monomolecular layer adsorption
- Equal affinity of each binding site for the hydronium ions
- No lateral interaction among adsorbed H^+
- Localized adsorption, i.e. no movement of adsorbate on the surface

The adsorption isotherm is described by the coverage of H^+ according to,

$$\Theta_{H^+} = \frac{K_{ad} c_{\mathrm{H}^+}}{1 + K_{ad} c_{\mathrm{H}^+}} \tag{4.4.3}$$

where K_{ad} is the adsorption constant which is temperature dependent following a vant Hoff equation of the type [Noll et al., 1991],

$$K_{ad} = K_{ad}^{o} \mathrm{e}^{\frac{-\Delta H_{ad}}{R_g T}} \tag{4.4.4}$$

where ΔH_{ad} is the heat of adsorption and K^{o}_{ad} is a frequency factor. It is important to note that determining the heats of adsorption in the liquid phase has been acknowledged to be rather challenging and that often low values have been reported [Builes et al., 2013], [Hsieh et al., 2008]. Thus, in the present work the heats of adsorption were assumed to be low enough that the effect of temperature is more prominent on the reaction rate constant, k_r, than on K_{ad}. The rate equations can be expressed according to,

$$\frac{\mathrm{d}c_{\mathrm{s}}}{\mathrm{d}t} = -k''_{tot} SA c_{\mathrm{H^+}} \left(1 - \frac{K_{ad} c_{\mathrm{H^+}}}{1 + K_{ad} c_{\mathrm{H^+}}}\right) = \frac{1}{1.647} \frac{\mathrm{d}c_{\mathrm{H^+}}}{\mathrm{d}t} \tag{4.4.5}$$

$$\frac{\mathrm{d}c_{Ca^{2+}}}{\mathrm{d}t} = k''_{tot} SA c_{\mathrm{H^+}} \left(1 - \frac{K_{ad} c_{\mathrm{H^+}}}{1 + K_{ad} c_{\mathrm{H^+}}}\right) = \frac{1}{1.647} \frac{\mathrm{d}c_{\mathrm{HCO_3^-}}}{\mathrm{d}t} \tag{4.4.6}$$

where k''_{tot} is the overall reaction constant expressed according to , [Sjöberg and Rickard, 1985], [MacInnis and Brantley, 1992],

$$\frac{1}{k''_{tot}} = \frac{1}{k_l} + \frac{1}{k_r} \tag{4.4.7}$$

The surface area available for reaction, SA, is calculated according to,

$$SA = SSA_{BET} MM_s c_s \tag{4.4.8}$$

where SSA_{BET} is the surface area estimated by means of Nitrogen adsorption and MM_s is the molar mass of the solid sample. Equations (4.4.5) and (4.4.6) are ordinary differential equations (ODE) which were solved numerically in order to estimate the model parameters, i.e. Ea, k_I and K_{ad}. Non-linear regression analysis was employed by using MODEST software by means of the backward differences method [Leis and Kramer, 1988]. The experimental data, including concentration as a function of time and temperature values, were combined and the parameter data fitting algorithm minimized the sum of squared errors according to,

$$Q = \| \mathbf{c_{exp}} - \mathbf{c_{exp}} \|_2 \tag{4.4.9}$$

where $\mathbf{c_{exp}}$ and $\mathbf{c_{est}}$ are the vectors of H^+ experimental and estimated concentrations respectively. Equation (4.4.9) is minimized by means of the Simplex-Levenberg-Marquardt method. It is noteworthy to mention that equation (4.4.9) was applied after assuming that the errors were normally distributed and the variance was constant over the whole experimental domain. The parameter data fitting procedures, which are explained in this chapter are actually non-linear programming (NLP) problems, where the objective function is given by the sum of errors between the model and the data. Sensitivity analysis of the solution to the dynamic problem was done and the shape of the objective function and the contour plot were analyzed in order to rule out correlation among the parameters (**Paper III**). Furthermore, the values of the Hessian matrix were evaluated and the matrix was found to be a positive semi-definite which indicates that at least a local minimum was obtained. The parameter estimation in this work was done numerically, however, equations (4.4.5) and (4.4.6) can also be solved analytically by assuming

a constant SSA_{BET}, and then the analytical solutions become,

$$\frac{1}{c_{H^+}} - K_{ad}\ln(c_{H^+}) = \lambda t - K_{ad}\ln(c_{H_o^+}) + \frac{1}{c_{H_o^+}} \tag{4.4.10}$$

$$\frac{1}{c_s} - \gamma K_{ad}\ln(c_s) = \gamma\lambda t - \gamma K_{ad}\ln(c_{s_o}) + \frac{1}{c_{s_o}} \tag{4.4.11}$$

$$\left(\frac{1}{c_{H_o^+} - \gamma c_{Ca^{2+}}}\right) - K_{ad}\ln\left(c_{H_o^+} - \gamma c_{Ca^{2+}}\right) = \lambda t + \frac{1}{c_{H_o^+}} - K_{ad}\ln\left(c_{H_o^+}\right) \tag{4.4.12}$$

$$\left(\frac{1}{c_{H_o^+} - \gamma c_{HCO_3^-}}\right) - K_{ad}\ln\left(c_{H_o^+} - \gamma c_{HCO_3^-}\right) = \lambda t + \frac{1}{c_{H_o^+}} - K_{ad}\ln\left(c_{H_o^+}\right) \tag{4.4.13}$$

where γ is the stoichiometric coefficient equal to 1.647, $c_{H_o^+}$, c_{s_o} are the initial hydronium ion concentration and solid concentration respectively. The constant λ is estimated according to,

$$\lambda = k''_{tot} SSA_{BET} MM_s \tag{4.4.14}$$

The results for the estimated parameters are presented in Table 4.1, for the small (s.) and large (l.) size fractions. The temperature dependence on the dissolution rates is presented for the small size fraction of the Parainen sample (plus one case for the large fraction) in Figure 4.6 (a). Furthermore, an example of the rates as a function of pH and the modeling results are presented in Figure 4.6 (b).

Table 4.1: Estimated kinetic parameters, free-drift method.

Sample	Ea (kJ/mol)	kI (L/m^{2}s)	Kad (L/mol)	R^2 (%)	error$_{Ea}$ (%)
Wolica s.	21.27	0.1156	880.3	99.5	1.1
Wolica l.	15.98	0.0389	880.3	99.1	1.0
Parainen s.	16.45	0.3932	354.2	99.3	2.0
Parainen l.	17.89	0.2541	354.2	99.2	1.0

The fit of the model to the experimental data seems satisfactory and the apparent activation energy values concur with previously reported results under similar conditions [Alkattan et al., 1998], [Gledhill and Morse, 2006]. Apparent activation energy values of around 25 (kJ/mol) have been previously presented in the literature as evidence for rates under mass transfer control [Sjöberg and Rickard, 1984b]. However, in the current work, experimental evidence has shown that external mass transfer, through mechanical agitation, could not be enhanced beyond the studied conditions and thus chemical reaction should be the rate limiting phenomena. The zeta potential, ζ, of calcium carbonate has been measured and its dependence on pH has been presented in the literature [Moulin and Roques, 2003]. Thus, an electrical double layer which is dependent on pH could be hindering the approach of the hydronium ions towards the surface, and this might be the reason why low apparent activation energies are found even under enhanced hydrodynamic conditions. Values of the zeta potential reported in the literature have been plotted as a function of pH in Figure 4.7.

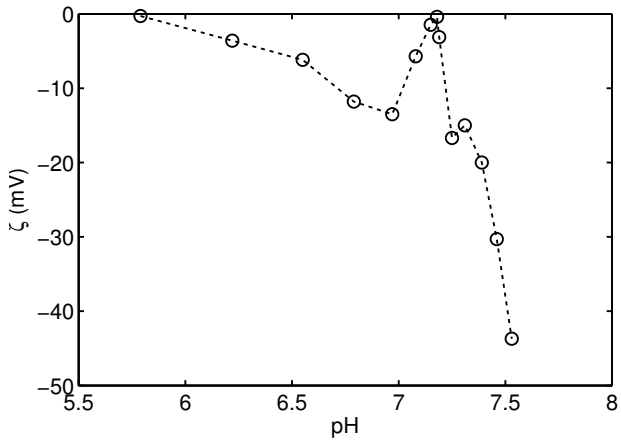

Figure 4.7: Zeta potential as a function of pH, reported in the literature [Moulin and Roques, 2003].

4.4.2 pH-stat method

Semi-batch experiments were performed with the pH-stat method (**Paper V**), the pH was controlled by an On-OFF control strategy, and an example of an experimental run is presented in Figure 4.8.

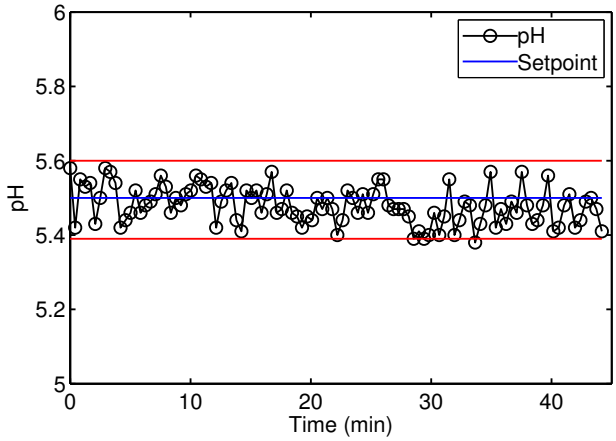

Figure 4.8: pH-stat influence of stirring run for Wolica small, 60 °C, at 1400 rpm.

The system can be modelled according to,

$$\frac{\mathrm{d}c_{\mathrm{s}}}{\mathrm{d}t} = r_{\mathrm{s}} - \frac{c_{\mathrm{s}}}{V}\frac{\mathrm{d}V}{\mathrm{d}t} \tag{4.4.15}$$

$$\frac{\mathrm{d}V}{\mathrm{d}t} = \dot{Q}_{in} - \dot{Q}_{out} \tag{4.4.16}$$

where r_s is the reaction rate of the solid, Q_{in} and Q_{out} are the volume flow of acid being pumped into the system and the liquid being evaporated, respectively. The volume flow of acid coming in is estimated according to [Plummer et al., 1978],

$$\dot{Q}_{in} = -2\frac{r_s V}{c_{\mathrm{HCl}}} \tag{4.4.17}$$

A surface factor, which has been previously defined as a roughness factor [Sing, 1985], was introduced as the ratio between the specific surface area measured by Nitrogen adsorption ($SSA_{real,o}$) and the specific surface area when the particles were be spherical ($SSA_{real,o}$). The surface factor, $S_{f,o}$ is defined according to,

$$S_{f,o} = \frac{SSA_{real,_o}}{SSA_{PSD,_o}} \tag{4.4.18}$$

The concentration of the solid phase can be related to the diameter of the particle, if the particles were ideal spheres according to [Grénman et al., 2011],

$$\frac{c_{\mathrm{s}}}{c_{\mathrm{s,o}}} = \frac{v_{\mathrm{s}}}{v_{\mathrm{s,o}}} = \frac{\pi 6 {d_p}^3}{\pi 6 {d_{p,o}}^3} \tag{4.4.19}$$

where v_{s} is the volume of the particle. Subsequently, when solving for d_p,

$$d_p = d_{p,o}\sqrt[3]{\frac{c_{\mathrm{s}}}{c_{\mathrm{s,o}}}} \tag{4.4.20}$$

The introduced surface factor takes into consideration the non-sphericity of the particles which is evident due to surface roughness (shown in the SEM images in Chapter 3). Thus, the diameter of the particles, for ideal spheres, can be related to the solid concentration and the dynamic specific surface area with the introduced correction becomes,

$$SSA_{real} = S_{f,o}\frac{6}{\rho_{\mathrm{s}}}\sum_{i=1}^{i_{max}}\frac{z_i}{d_{p,i,o}}\frac{1}{\sqrt[3]{\frac{c_{\mathrm{s}}}{c_{\mathrm{s,o}}}}} \tag{4.4.21}$$

The mass transfer coefficient can be estimated by using equation (4.3.5), provided there are turbulent conditions. The PSD and the correction for non-spherical particles is thus implemented,

$$k_l = \frac{D_j^{2/3}\varepsilon^{1/6}}{\nu^{1/6}}\left(\frac{1}{N_s}\right)^{1/3}\sum_{i=1}^{i_{max}}\frac{z_i}{d_{p,i,o}^{1/3}}\frac{1}{\left(\frac{c_{\mathrm{s}}}{c_{\mathrm{s,o}}}\right)^{1/9}} \tag{4.4.22}$$

where N_s is the shape factor, 1 for spherical particles, and is defined as the inverse of the surface factor. The total reaction constant is obtained from substituting equation (4.4.22) into equation (4.4.7) and becomes,

$$k_{tot} = \frac{\frac{D_j^{2/3}\varepsilon^{1/6}}{\nu^{1/6}}\left(\frac{1}{N_s}\right)^{1/3}\sum_{i=1}^{i_{max}}\frac{z_i}{d_{p,i,o}^{1/3}}\frac{1}{\left(\frac{c_{\mathrm{s}}}{c_{\mathrm{s,o}}}\right)^{1/9}}k_r}{\frac{D_j^{2/3}\varepsilon^{1/6}}{\nu^{1/6}}\left(\frac{1}{N_s}\right)^{1/3}\sum_{i=1}^{i_{max}}\frac{z_i}{d_{p,i,o}^{1/3}}\frac{1}{\left(\frac{c_{\mathrm{s}}}{c_{\mathrm{s,o}}}\right)^{1/9}} + k_r} \tag{4.4.23}$$

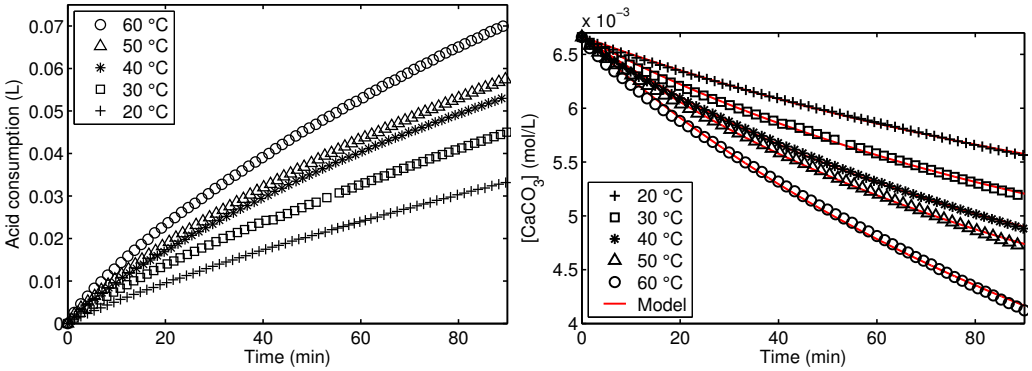

(a) Effect of temperature Wolica

(b) Modeling results Wolica

Figure 4.9: Concentration as a function of time, for Wolica small (20, 30, 40, 50, 60 °C), and modeling results.

Equations (4.4.15) and (4.4.16) be re-written to include the reaction rate according to,

$$\frac{\mathrm{d}c_\mathrm{s}}{\mathrm{d}t} = -k_{tot} S_{f,o} SSA_{real} MM_\mathrm{s} c_\mathrm{s} \left(c_{\mathrm{H}^+}^{\infty\ \alpha} - c_{Ca^{2+}} C_{eq} \right)$$
$$- \frac{2}{c_\mathrm{HCl}} S_{f,o} SSA_{real} MM_\mathrm{s} c_\mathrm{s}^2 \left(c_{\mathrm{H}^+}^{\infty\ \alpha} - c_{Ca^{2+}} C_{eq} \right) + \frac{c_\mathrm{s}}{V} b_{flow} \dot{Q}_{out} \tag{4.4.24}$$

$$\frac{\mathrm{d}V}{\mathrm{d}t} = \frac{2V}{c_\mathrm{HCl}} k_{tot} S_{f,o} SSA_{real} MM_\mathrm{s} c_\mathrm{s} \left(c_{\mathrm{H}^+}^{\infty\ \alpha} - c_{Ca^{2+}} C_{eq} \right) - b_{flow} \dot{Q}_{out} \tag{4.4.25}$$

where α is the order of reaction, C_{eq} is the pseudo equilibrium constant. The ODE system, equations (4.4.24) and (4.4.25) were solved numerically in MATLAB by means of a numerical method for non-stiff differential equations, which solved the unconstrained minimization problem. The estimated parameters where k_r, C_{eq}, which were also estimated by minimizing the objective function in equation (4.4.9). The effect of temperature on the Wolica sample in the pH-stat method is presented in Figure 4.9 (a) while the fit of the model to the solid concentration is presented in Figure 4.9 (b). The model describes the data in an accurate manner with regression coefficients above 99 % when modeling the concentration and 95 % when modeling the volume. The modified Arrhenius equation, (4.4.2), was also utilized in order to estimate the apparent activation energies which were 21 ±2 (kJ/mol) and 30 ± 3 (kJ/mol) for the Wolica and Parainen samples respectively. The results in terms of logarithmic values of the initial rates calculated at 25 °C give -6 log(mol/m^2s), which is in accordance with literature values found between -5 and -6 log(mol/m^2s) at pH 5.5 [Brantley et al., 2008]. Furthermore, the results in the pH-stat method are in agreement with the values found for the Wolica sample in the free-drift method. Nonetheless, in the case of the Parainen sample, the apparent activation energies found by the two methods differ to some extent. As it has been previously reported, different activation energies have also been measured at different

values of pH. Therefore, as mentioned above, it is suggested that the change in the zeta potential might have some influence on the apparent activation energies measured.

CHAPTER 5

Solid-liquid dynamics

The modeling of kinetic and mass transfer phenomena is of paramount importance to obtain reliable parameters which can be utilized when developing optimization models, such as the one presented in Chapter 6. As has been explained previously in Chapter 4, the conditions required to accurately study the dissolution reaction cannot be emulated under industrial operations due to obvious technical limitations. Thus, in this work an Electrical Resistance Tomography (ERT) was adopted in order to study the dynamics of suspending solids in stirred vessels under conditions of high solid concentration, which approach the industrial application. The minimum suspension speed required to assure an off-bottom condition or the critical suspension speed, N_{js}, has been calculated by means of a correlation, and was used in **Papers I-IV**. Inert particles (glass beads) were used when studying the solid-liquid dynamics with the ERT method, and two size fractions having 138 μm and 385 μm as their mean diameter were employed. The diameter that a glass bead particle would have in order to have the same settling velocity of the small size fraction of the Wolica sample was considered when sieving the glass bead particles.

5.1 Settling velocity

The settling velocity of a particle in a fluid is an important parameter that can be used as a constant value when studying different solid-liquid suspension systems. The terminal settling velocity, u_t, can be calculated after applying a balance of forces that act on a particle that has reached its settling velocity. The forces involved are: the weight, the buoyancy, and the drag forces. In order to estimate the drag force, the drag coefficient C_D can be calculated by means of the correlation by Schiller and Naumann [1933],

$$C_D = \frac{24}{Re_p}\left(1 + 0.15{Re_p}^{0.687}\right) \tag{5.1.1}$$

Table 5.1: Glass bead diameters having u_t of limestone particles.

Sample	ρ (kg/m^3)	Mean d_p (μm)	Equivalent glass bead d_p (μm)	u_t (m/s)
Wolica s.	2703	111	119	0.01
Wolica l.	2703	268	288	0.04

The balance of forces acting on the particle, i.e. drag, buoyancy, and weight, gives the following expression for the settling velocity,

$$u_t = \sqrt{\frac{4 d_p g \left(\rho_s - \rho_l\right)}{3 \rho_l C_D}} \tag{5.1.2}$$

where g stands for the acceleration of gravity, ρ_s and ρ_l are the solid and liquid phase densities respectively. The inert glass bead particles had a density of 2500 (kg/m^3). Equation (5.1.2) was used to calculate the equivalent diameters of the glass beads, presented in Table 5.1. A corrected settling velocity equation for dense system was introduced by Gidaspow [1994],

$$u_t = \sqrt{\frac{4 d_p g \left(\rho_s - \rho_l\right)}{3 \rho_l C_D (1-\varphi)^{-1.65}}} \tag{5.1.3}$$

where ϕ is the volumetric fraction of solids, Equation (5.1.3) was employed in **Paper IV & V**.

5.2 Complete suspension of solids

The knowledge of the minimum stirring speed at which all particles are suspended (N_{js}), also defined as complete suspension, is an important parameter which is crucial for applications where agitation of solid particles immersed in liquid are adopted. It is important to clarify, however, that complete suspension of solids does not imply directly homogeneous distribution. Determining the N_{js} value is important because it gives information about the stirring speed under which the surface area of the solid particles available for reaction with the liquid phase is maximized. Several experimental methods for characterizing the N_{js} value have been presented in the literature over the years. A review of some of these methods has been presented by Jafari et al. [2012] who applied Gamma-Ray Densitometry to measure N_{js}. One of the most commonly applied techniques consists in visual observation of the off-bottom suspension of the particles [Zwietering, 1958]. The correlation which has been extensively applied was derived from the experimental results in the research work of Zwietering [1958],

$$N_{js} = S \left(g \frac{\rho_s - \rho_l}{\rho_l} \right)^{0.45} (d_p)^{0.2} (X_{mass})^{0.13} (\nu)^{0.1} (D_s)^{-0.85} \tag{5.2.1}$$

where S is a dimensionless parameter which is dependent on the system geometry and X_{mass} is the fraction of solid in suspension (%). Equation (5.2.1) and the method of

Zwietering [1958] have been widely applied mainly because they are rather simple and non-intrusive methods. The Zwietering visual method consists in visual observation of the particles in order to determine when the particles do not rest on the bottom for more than 1-2 seconds. Nonetheless, it has been acknowledged that the method loses accuracy in the case of higher solid loadings [Jafari et al., 2012]. More sophisticated as well as more complex methods have also been presented to assess the N_{js} values, some examples are: the Doppler effect at the bottom of the vessel, a decrease in the count rate from a radioactive tracer, and pressure changes at the bottom of the vessel [Jafari et al., 2012]. In the present work the correlation by Zwietering was used to estimate the critical suspension speed in **Paper I-III, V**, while the correlation and the visual criterion were used in **Paper IV**.

5.3 Electrical resistance tomography

Different methods have been developed and adopted when studying solid-fluid dynamics in stirred tanks. Optical methods such as Particle Image Velocimetry (PIV) have been applied successfully to study dilute suspensions in solid-liquid systems [Montante et al., 2012]. Furthermore, a range of tomographic techniques including nucleonic transmission, nucleonic emission, optical interferometry, electrical capacitance, electrical impedance, and electrical resistance have been adopted for solid-liquid mixing in the lab on a pilot plant scale [Williams, 1995]. Electrical Resistance Tomography (ERT) is a considerably inexpensive and robust technique that has been applied widely for research and development. The technique has already been applied to the study of mixing processes, solid-liquid filtration processes, hydrocyclone performance, as well as measurement and control of bubble columns [Bolton and Primrose, 2005]. It has been claimed that ERT can be advantageous with respect to other methods because it allows for a non-intrusive study of opaque processes when optically-based sensors are unsuitable [Williams, 1995]. Moreover, some authors have acknowledged that this technique has the potentiality of validating complex computational fluid dynamic (CFD) models [Mann et al., 2001]. Other tomographic methods have been regarded as unsafe, and much slower than ERT, which has been stated to be another advantage of this technique [Ricard et al., 2005a]. The application of ERT to the study of chemical processes has been present since the early 1990s. Although commercially available instruments have only been available recently, it also demonstrates the stage of development of the technique. In the literature, several studies where ERT has been applied for gas-liquid systems have been presented, some examples include: the work by Mann et al. [1997] and more recently the work by Montante and Paglianti [2015]. In addition, solid-liquid systems have been widely investigated by this technique, some examples include the work by Hosseini et al. [2010], Ricard et al. [2005b] and the study by Harrison et al. [2012].

5.3.1 ERT experimental method

The ERT method consists in providing a constant alternating current through the periphery of the vessel and measuring the surface potentials Kotre [1989].

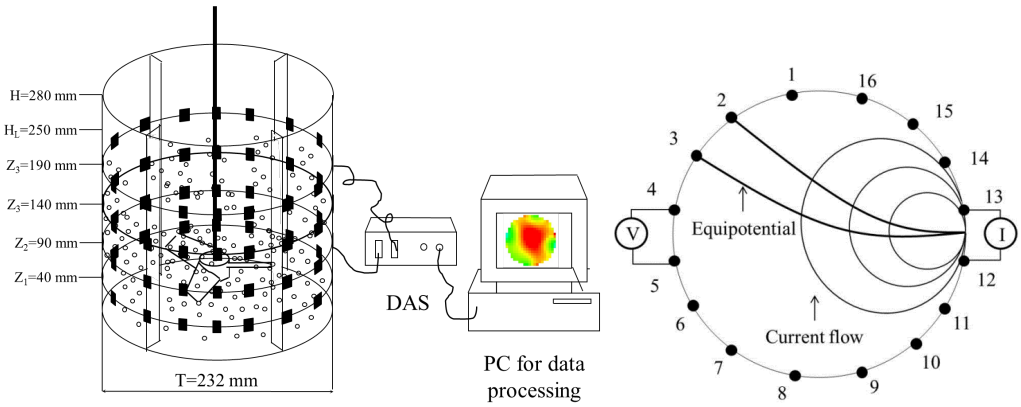

(a) Experimental set-up **(b)** Adjacent strategy

Figure 5.1: Electrical Resistance Tomography (ERT) experimental set-up, and measurement strategy.

Subsequently, an image reconstruction algorithm is applied to the potential measurements in order to obtain a two dimensional "slice" of the plane. When multiple panels are adopted, it is possible to obtain a 3-D spatial dimension which can be extended to 4 dimensions if a transient process is investigated [Mann et al., 2001], [Kagoshima and Mann, 2005]. The data collection strategy has been acknowledged to be a factor of great importance when reconstructing the conductivity distribution inside the vessel. The most important strategies are: the adjacent, opposite, diagonal and conducting boundary strategies [Dickin and Wang, 1996]. The adjacent measuring strategy was employed in this work and it is presented in Figure 5.1 along with the experimental set-up composed of the vessel, the electrodes and the Data Acquisition System (DAS). In the adjacent strategy, a current is applied through two neighboring electrodes at a time, while the potential is measured by another pair of electrodes. The procedure is afterwards repeated by injecting a current from the following pair of electrodes and measuring the voltages until the combinations are all fulfilled. This procedure has the advantage of being suitable for fast image reconstruction. Nonetheless, one disadvantage is that the current distribution is not completely uniform because the current travels mainly along the periphery of the vessel [Dickin and Wang, 1996]. The reconstructed tomogram is divided into a mesh of 20×20 pixels, from which 316 pixels lie inside the circular tomogram. The spatial resolution of the ERT method has been reported to be 5% the diameter of the vessel [Holden et al., 1998]. The 5% resolution is the theoretical value, however, the actual resolution also depends on the type of object which is being imaged [Stanley, 2006]. Another important aspect of the ERT method regards the reconstruction algorithm used to produce the tomograms from the potential measurements. The ERT system ITS 2000 by Industrial Tomography Ltd. was adopted in this work. The ITS 2000 is comprised of the electrodes, the DAS system shown in Figure 5.1, and software which employs the linearized (non-iterative) back projection algorithm.

Table 5.2: Experimental conditions ERT.

Mean d_p (μm)	X_{mass} (%)	N (rpm)	Type of impeller
138	24;43	500-900, step: 100 rpm	PBT
385	24-43, step: 0.05	500-900, step: 100 rpm	PBT
385	24-43, step: 0.05	500-900, step: 100 rpm	A310

The aforementioned algorithm is qualitative, which makes the reconstruction procedure quite fast. The qualitative back projection algorithm can be applied in one step which is an advantage with respect to some of the quantitative algorithms that require much more computational effort [Wang et al., 1999].

In this study a Plexiglass vessel was employed with standard geometry, a flat bottom, and four equally-spaced baffles. A set of 16 stainless steel electrodes were fixed to the vessel wall comprising four planes. The impeller shaft was covered with rubber lining in order to reduce interference with the current and the impeller was positioned between the first and second plane. Two types of impellers, which are commonly adopted for solid suspension were employed: a Lightnin A310 impeller and a 6-bladed 45° Pitched Blade Turbine (PBT) pumping downwards. The solid phase was composed of inert particles, glass beads, which were sieved into two size fractions having mean diameters of 138 μm and 385 μm. As was mentioned in section 5.1, the small size fraction was sieved in order to have a diameter approaching the equivalent diameter for the Wolica small sample as presented in Table 5.1. The liquid phase was composed of 10.6 L of de-mineralized water with 5 g of dissolved NaCl in order to increase the conductivity of the continuous phase, which is necessary for accurate measurements [Stanley, 2006]. A variety of conditions were investigated with both impellers by combining different stirring speeds, particle size, and the fraction of solids in suspension. The different experimental conditions which were studied are presented in Table 5.2.

5.3.2 ERT results

The degree of solid mixing inside the stirred reactor was assessed from the change in conductivity with respect to the continuous phase. In the present work a qualitative algorithm was applied, thus, the measured conductivity was set as one (1) for the continuous phase and zero (0) for the dispersed phase. An example of the averaged (over the plane) dimensionless conductivity for 600 acquisitions is presented in Figure 5.2 (a). The solid concentration distribution was obtained by means of the Maxwell correlation [Harrison et al., 2012],

$$X_v = \frac{\sigma_l - \sigma_m}{\sigma_l + 0.5\sigma_m} \tag{5.3.1}$$

where X_v is the solid volume fraction, σ_m and σ_l are the slurry and the liquid conductivities respectively. The volume fractions were normalized with respect to the mean volume fraction as also presented by Hosseini et al. [2010].

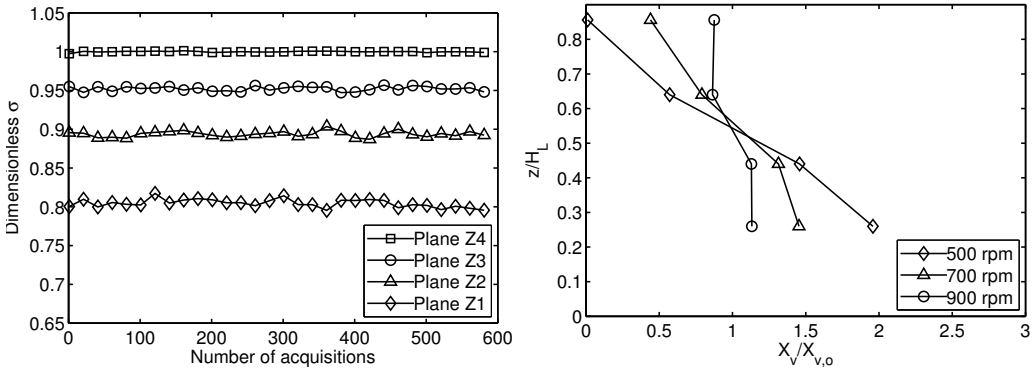

(a) Dimensionless mean conductivity **(b)** Axial solid concentration

Figure 5.2: Dimensionless mean conductivity (a) 500 rpm, X_{mass}=24 %, d_p=385 μm, PBT (b), Axial solid profile X=43 % and d_p=138 μm.

An example of the dimensionless concentration profiles for different stirring speeds and the normalized height is presented in Figure 5.2 (b). The axial concentration profiles as the one shown in Figure 5.2 (b) are also known as the "belly plot" [Ricard et al., 2005b]. The results show how at higher stirring speeds the solids approach an homogeneous distribution which would imply a vertical line with the $X_v/X_{v,o}$ approaching 1.

The ERT data allows for the calculation of a parameter which can assess the degree of mixing; such parameter is also known as the mixing index, MI. The mixing index has often been defined in terms of the Relative Standard Deviation (RSD) of the solid concentration [McKee et al., 1995], [Williams, 1995] The homogeneity across the vessel volume has been assessed as well [Hosseini et al., 2010]. The index MI which was derived by Williams et al. [1996]. The overall mixing index, MI_m, is calculated according to,

$$MI_m = \frac{\sum_{z=1}^{q} MI_z}{q} \tag{5.3.2}$$

where q is the number of planes, and the mixing index for the plane, MI_z, which is calculated according to [Williams et al., 1996],

$$MI_z = \frac{1}{\overline{\sigma_i}} \sqrt{\left(\frac{\sum_{k=1}^{n} (\sigma_k - \overline{\sigma}_i)^2}{n-1} \right)} \tag{5.3.3}$$

where $\overline{\sigma}_i$ is the mean conductivity averaged across the plane and σ_k is the conductivity in each pixel. The overall mixing index provides information on the degree of homogeneity with respect to each plane and gives information on radial distribution. A total mixing index, MI_{tot} was introduced in this work,

$$MI_{tot} = \frac{1}{\overline{\sigma}} \sqrt{\left(\frac{\sum_{k=1}^{p} (\sigma_k - \overline{\sigma})^2}{p-1} \right)} \tag{5.3.4}$$

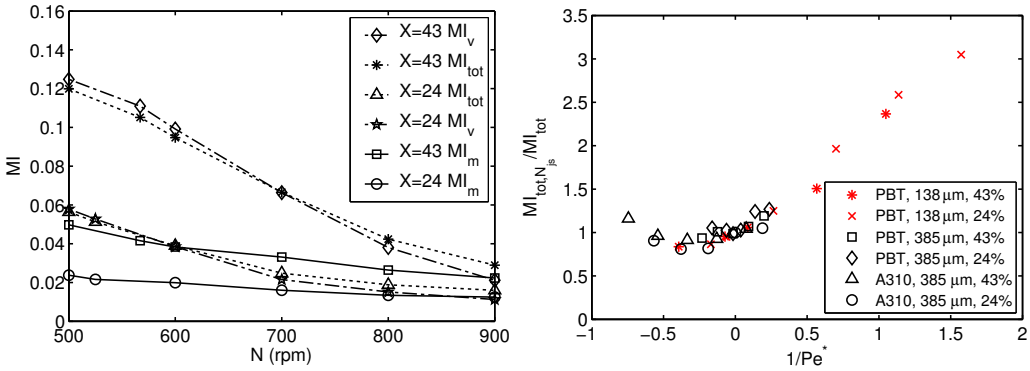

(a) Mixing Indexes **(b)** Modified Peclet

Figure 5.3: Mixing Indexes (a) for d_p=138 μm, PBT, and modified Peclet Number (b).

where p is the total number of pixels inside the vessel volume, which amounts to 1264, and $\overline{\sigma}$ is the conductivity averaged over the whole volume. The MI_{tot} is defined as the RSD with respect to an overall mean value considering each of the pixels investigated. Furthermore, a fourth mixing index can be obtained by combining the RSD concept and the Homogeinity index by Hosseini et al. [2010],

$$MI_v = \frac{1}{\overline{\sigma}} \sqrt{\left(\frac{\sum_{k=1}^{q} (\overline{\sigma}_i - \overline{\sigma})^2}{q-1} \right)} \tag{5.3.5}$$

where $\overline{\sigma}$ is the mean conductivity averaged over the whole volume and $\overline{\sigma}_i$ is the mean conductivity averaged over the plane. A comparison between the aforementioned mixing indexes is presented in Figure 5.3 (a). The results presented in Figure 5.3 (a) show that increasing the impeller speed increases homogeneity, since a completely homogeneous dispersion would give an RSD approaching zero. The increase of N decreases MI_m slowly when actually MI_v and MI_{tot} decrease more markedly. This result concurs with the observation by Harrison et al. [2012] where it was stated that MI_m assesses mainly radial distribution. Thus, the MI_m index fails to account for the lack of homogeneity in the axial direction which is definitely the case at 500 rpm for the small size fraction.

The energy required for suspending the solids up to a height Δh per unit volume is a function of the solid, liquid and mixture densities (ρ_{m}) as well as the solid to liquid mass ratio according to,

$$E_r \propto (\rho_{\mathrm{s}} - \rho_{\mathrm{l}}) g \Delta h \frac{X_{mass}}{1 + X_{mass}} \frac{\rho_{\mathrm{m}}}{\rho_{\mathrm{s}}} \tag{5.3.6}$$

Subsequently, Δh is proportional to the power number, N_p, and the pumping number, N_Q, of the system according to,

$$\Delta h \propto \frac{N_p}{N_Q} N^2 D_s^2 \frac{1 + X_{mass}}{X_{mass}} \frac{\rho_{\mathrm{s}}}{g(\rho_{\mathrm{s}} - \rho_{\mathrm{l}})} \tag{5.3.7}$$

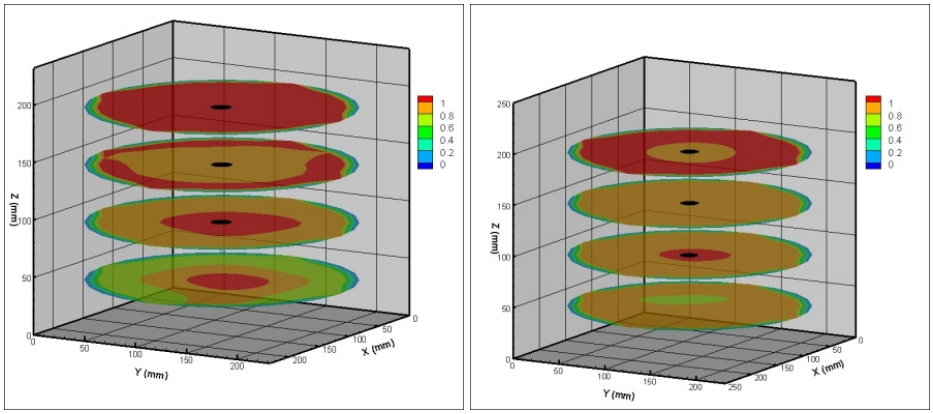

(a) 500 rpm, X_{mass}=43% **(b)** 900 rpm, X_{mass}=0.24%

Figure 5.4: Dimensionless condictivity tomograms, A310, d_p=385 μm, (a) 500 rpm, X_{mass}=43%, and (b) 900 rpm, X_{mass}=24%.

The MI_{tot} evaluated at the N_{js} was correlated to the ratio between H_L and Δh in **Paper IV**. Moreover, the modified Peclet number, Pe^*, which was presented in this work and already discussed in Chapter 4 can be calculated according to,

$$Pe^* = \frac{u_t H_L}{D_{es}} \tag{5.3.8}$$

where the relative axial dispersion for the solid phase is defined as,

$$D_{es} = b(N - N_{js})D_s^2 \tag{5.3.9}$$

where b is the dimensionless constant that depends on the type of impeller. The approach presented in this work allowed for a correlation between the mixing index at the just suspended condition and the modified Peclet number as it is shown in Figure 5.3 (b). This result allows for links between the different operating conditions and the degree of mixing in the vessel.

In this work it was possible to utilize the data provided by the ERT system in a variety of ways, however, the main objective of the method is to image the inside of the vessel. Examples of the 2D tomograms presented of the small and large size fractions under different conditions are presented in Figures 5.4 and 5.5. The dimensionless conductivity tomograms can provide information on how the solids are distributed both radially and axially. For instance, a more pronounced axial gradient can be observed in Figure 5.4 (a) than in Figure 5.5 (a). Where, on the other hand a homogeneous dispersion, visually confirmed, was attained in the case of Figure 5.5 (b). Moreover, the shape of the interface between the slurry and the clear liquid was also reproduced from the ERT data.

The so-called iso-surfaces of the dimensionless conductivities of 0.9 are presented in Figure 5.6. The value for the conductivity used to recreate the iso-surfaces was chosen as

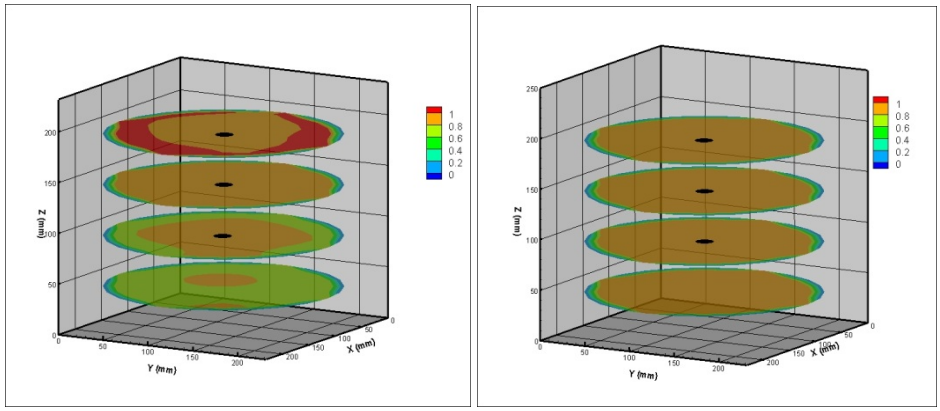

(a) 500 rpm, X_{mass}=43% **(b)** 900 rpm, X_{mass}=0.24%

Figure 5.5: Dimensionless condictivity tomograms, PBT, d_p=138 μm, X_{mass}=43%, (a) 500 rpm, and (b) 900 rpm.

0.9 since it was also found previously to be sufficient for air-water systems. The shape of the interface which was obtained from the results on the two upper planes for the runs at the N_{js} were also visually confirmed. An important result presented in Figure 5.6 is that the shape of the interface is highly dependent on the size of the dispersed phase. In the case of the finer size fraction, the interface is mainly flat with a maximum at the center of the vessel. While for the large size fraction, the interface has a conical shape with its vertex close to the impeller. This effect was expected to be induced by the centrifugal forces acting on the particles and it is dependent on particle size.

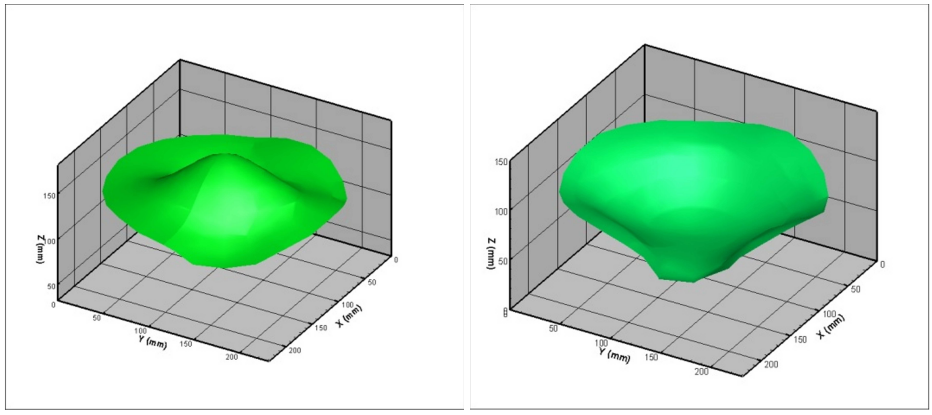

(a) Small particles glass beads **(b)** Large particles, glass beads

Figure 5.6: Iso-surface of dimensionless conductivity equal to 90%, PBT, Xv= 0.43, N=N_{js}, for (a) d_p=138 μm, and (b) d_p=385 μm.

CHAPTER 6

Process optimization

Some studies presented in the literature have focused on optimizing WFGD systems, either by minimizing operating costs or by increasing the removal efficiency [Frandsen et al., 2001], [Warych and Szymanowski, 2001], [Gutiérrez Ortiz et al., 2006], [Hrastel et al., 2007] and [Zhong et al., 2008]. However, these approaches have been mostly empirical and so far deterministic (or non-deterministic) optmization methods have not often been applied directly to WFGD. In the work by Cristóbal et al. [2012], a mixed integer non-linear programming (MINLP) model was developed in order to minimize pollution in coal combustion after combining different technologies including FGD. In the current work, the objective was to utilize the information obtained by detailed modeling in order to optimize the energy consumption of a study-case by means of deterministic global and local optimization.

6.1 Optimization preliminaries

Deterministic and non-deterministic optimization plays an important role in today's industrialized and globalized world. In the process industry especially, optimization has become more important since it provides a robust tool for improving a process whether by making it more efficient or by minimizing the operating costs. One practical large-scale industrial example is the solution produced for the production planning in the stainless steel industry [Karelahti et al., 2011]. Another noteworthy example is the minimization of the running costs required to operate pumps in process industries. For instance, in the pulp and paper industry where 10-20% of the energy of the process is consumed solely by the pumping systems. Therefore, optimization algorithms have been developed which allow for the optimal selection of the pumps configuration which helps in minimizing the pumping energy consumption [Westerlund et al., 1994]. Many examples can be found in the literature, and another classical problem that has been tackled is the optimization of heat exchanger networks.

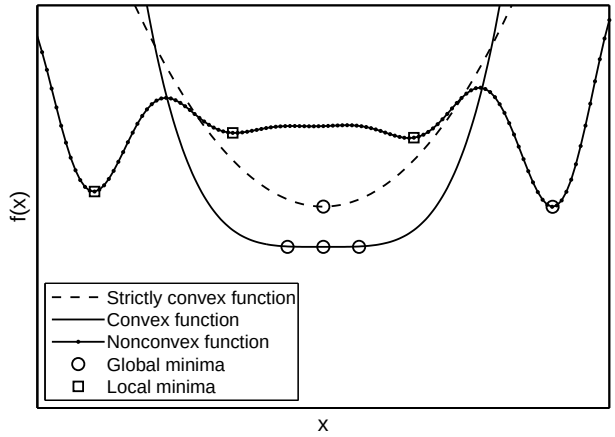

Figure 6.1: Examples illustrating convex and nonconvex functions.

6.1.1 Convexity condition

The first-order convexity condition implies that for a function f which is differentiable, the tangent of a convex function will underestimate the function [Lundell, 2009]. The second-order condition for convexity, requires the function f to be twice differentiable, that is, that the Hessian or second derivative $\nabla^2 f(\mathbf{x})$ exists at every point in **dom** f. Thus, $f(\mathbf{x})$ is convex having a positive semidefinite Hessian if and only if [Boyd and Vandenberghe, 2004],

$$\nabla^2 f(\mathbf{x}) \geq 0. \tag{6.1.1}$$

The illustrations of a strictly convex, a convex, and nonconvex functions are presented in Figure 6.1. These examples show that a nonconvex function will have several local minima and one global minimum. Thus, when solving a nonconvex problem it is possible to find a solution that is a local minimum but is not yet the best possible solution, as in the nonconvex example of Figure 6.1, where three local minima are shown. However, if the problem is strictly convex, the found solution is guaranteed to be the best possible one. In the case of a function which is convex, but not strictly convex, more than one value of x will provide the same best objective value of $f(x)$, this is also shown in Figure 6.1.

Many Non Linear Programming (NLP) problems, including MINLP encountered in industry do not fulfill the condition given by equation (6.1.1). Thus, this implies that solving the problem will not guarantee finding the best solution, or in other words, the solution might be a local minimum. Thereafter, an important part of research in optimization has been devoted to developing tools and methods that guarantee global optimality even in the case of nonconvex problems. One approach that has been applied to tackle this problem has been the use of convex approximations for the nonconvex problem. The basis of these methods rely on the application of a relaxation to the original nonconvex problem and subsequently applying existing algorithms for

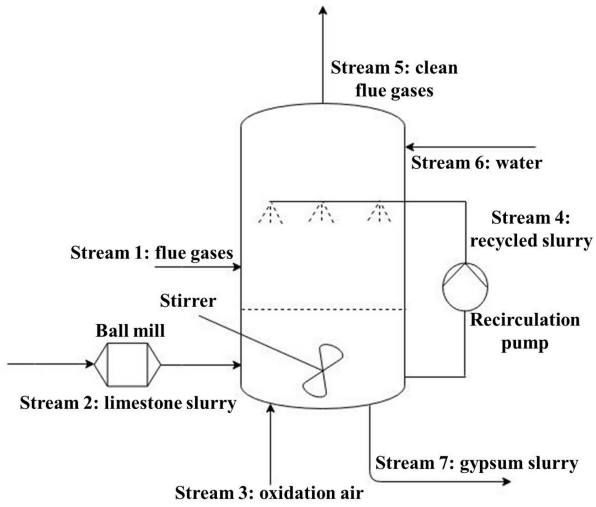

Figure 6.2: WFGD scrubber flow diagram

convex optimization to solve the approximated problem [Lundell, 2009]. As examples of algorithms which are commonly employed for solving convex problems are the well-known Outer-Approximation (OA) algorithm by Duran and Grossmann [1986] and the Extended Cutting Plane (ECP) algorithm by Westerlund and Pettersson [1995]. In this work, the ANTIGONE solver by Misener and Floudas [2014] which is a global solver that employs underestimators as the convexification strategy was used when searching for the global optimum of the optimization problem. In addition to the underestimators, other convexification techniques involving the manipulation of the diagonal and off-diagonal elements of the Hessian matrix have been developed. Furthermore, more details on the use of convex underestimators and on the convexification techniques can be found in the works of Lundell [2009] and Skjäl [2014].

6.2 Optimization of the case-study

A variety of studies and models concerning limestone dissolution have been presented in the literature, as mentioned in Chapter 2. Analogously, different models have been applied when studying the absorption of SO_2 in the WFGD spray towers. The two-film theory has been applied in the models presented by Olausson et al. [1993], Warych and Szymanowski [2001] and Dou et al. [2009]. The penetration theory has been adopted in the work by Gerbec et al. [1995]. Furthermore, a CFD model featuring the Euler-Euler approach was developed and presented by Gómez et al. [2007]. In the work by Zhong et al. [2008], the influence of combining different spray levels to the desulfurization efficiency was modelled. Moreover, a detailed CFD simulation of the oxidation tank has been presented by Keskinen et al. [2002], with the aim of optimizing the design parameters of the reaction tank.

Table 6.1: Case study parameters.

Inlet flue gas (wet)	1800000
Reaction tank volume (m^3).	2143.1
Inlet slurry weight composition (%)	16.6
Liquid to gas ratio (L/G) (L/Nm^3)	3.06≤L/G≤15
Flue gas outlet relative humidity (Φ) (%)	27.3
Ca to S ratio (Ca/S)	0.9≤L/G≤1.05
Temperature, stream 2 (°C)	38
Temperature, stream 3 (°C)	100
Temperature, stream 6 (°C)	7.25
Removal efficiency (E_f) (%)	93.817
Pressure, stream 1 (kPa)	104.4
Pressure, stream 3 (kPa)	191.3
Pressure, stream 5 (kPa)	101.3

In the present work, an optimization model for a case-study of a WFGD plant in Finland was developed by taking into consideration the parameters determined in Chapter 4. The absorption of SO_2 was modelled by coupling it to the efficiency requirement, since this work was mainly devoted to limestone dissolution. The overall chemical reaction of the WFGD scrubber is presented in Equation (2.2.11). A flow diagram of the counter-current scrubber that was considered in this optimization is depicted in Figure 6.2 while the parameters of the case study are presented in Table 6.1.

The removal efficiency was calculated according to [Gutiérrez Ortiz et al., 2006],

$$E_f = 1 - \frac{y_{\mathrm{SO_{2,out}}}}{y_{\mathrm{SO_{2,in}}}} \tag{6.2.1}$$

The NLP problem can be formulated according to,

$$\begin{aligned} &\text{minimize} && f(\mathbf{x}) \\ &\text{subject to} && h(\mathbf{x}) = 0 \\ &&& g(\mathbf{x}) \leq 0 \\ &&& x_k^L \leq x_k \leq x_k^U, \quad k \in \{1, 2, \ldots, 9\} \end{aligned} \tag{6.2.2}$$

where $f(\mathbf{x})$ is the objective function, that is estimated as the sum of the power consumed by each operating unit: milling, stirring and pumping. The linear and non-linear equality constraints are represented by $h(\mathbf{x})$ while $g(\mathbf{x})$ are the non-linear inequality constraints, x_k^L and x_k^U are the lower and upper bounds of the variables respectively. The model is comprised of five equality constraints, from which three are non-linear, and three non-linear inequality constraints. The objective function, $f(\mathbf{x})$, is calculated according to,

$$P_{tot} = P_{Mill} + P_{Stirr} + P_{Pump} \tag{6.2.3}$$

Table 6.2: Solution for the consumed power.

Power consumed	Wolica sample	Parainen Sample
Milling (kW)	**443.9**	**827.85**
Stirring (kW)	46.8	16.7
Pumping (kW)	652.6	649.5
Total (global solution) (kW)	1143.4	1494.1
Total (local solution) (kW)	1154.8	1494.16
Milling for $d_{p,80}$=44μm (kW)	**886.5**	**1254.7**

The power required for the milling unit, P_{Mill}, is described according to,

$$P_{Mill} = \left(\frac{10W_I}{\sqrt{d_{p,80}}} - \frac{10W_I}{\sqrt{d_{f,80}}} \right) \frac{\dot{m}_2}{0.9072} \tag{6.2.4}$$

where W_I is the Bond work index, and it is dependent on the type of rock, i.e. depending on the geological background of the sample. The power for milling, equation (6.2.4), is calculated according to Bond's law. The $d_{p,80}$ and $d_{f,80}$ are the diameters of the particles of the product and the feed respectively, where 80% of the material is finer [Rhodes, 1998]. The diameter of the feed was taken as 19 mm according to the literature [Stultz and Kitto, 2005]. The power consumed by stirring is assumed to be directly proportional to the mean dissipated energy, even though it is known that only a fraction of the motor power goes to stirring [Hajek and Murzin, 2004]. The power for stirring can be estimated according to,

$$P_{Stirr} = 5N_{p,side}N_{opt}^3 D_{opt}^5 \rho_7 \tag{6.2.5}$$

where $N_{p,side}$ is the power number for side-entering stirrers, D_{opt} is the diameter of the scrubber stirrers and ρ_7 is the density of stream 7 in Figure 6.2. The study-case features 5 side entering stirrers, so that the power consumed by stirring is obtained by multiplying the power required per stirrer times 5. The power which is consumed by the pumps is proportional to the volumetric flow of the recycled slurry [Gutiérrez Ortiz et al., 2006] and can be estimated according to,

$$P_{Pump} = \left(\frac{1}{\eta} \right) L \left(g\rho_7 H_{abs} \left(1 + \frac{\Delta P_{loss}}{\Delta P_{Pump}} \right) \right) \left(\frac{1}{3600} \right) \tag{6.2.6}$$

where η is the pump efficiency, taken as 0.6, L is the volumetric flow of recycled slurry, H_{abs} is the absorber height and $\frac{\Delta P_{loss}}{\Delta P_{Pump}}$ is the ratio between the pressure losses in the pipe and the pressure loss due to height.

The five equality constraints, $h(\mathbf{x})$, are comprised of the molar balances, $CaCO_3$ and H_2O, the design equation of the reaction tank, the energy balance, and the condition for the saturation pressure (stream 5). The reaction tank was modeled as a continuously stirred tank reactor (CSTR), as it has been previously assumed in the literature [Olausson

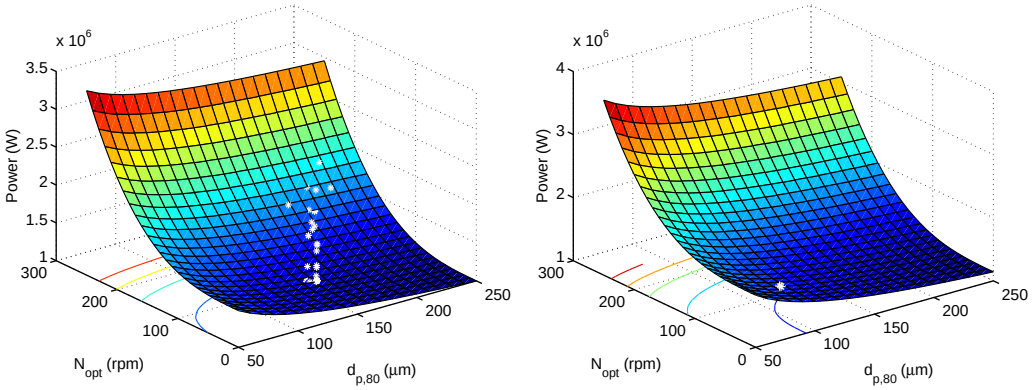

(a) Wolica **(b)** Parainen

Figure 6.3: Objective function for Wolica, and Parainen as a function of 2 variables: N_{opt} and d_p, the rest of the variables were kept constant.

et al., 1993], [Brogren and Karlsson, 1997]. Furthermore, the gas phase was assumed to behave as ideal; a common assumption found in the literature [Eden and Luckas, 1998], [Zhong et al., 2008], [Zhu et al., 2015].

The five equality constraints are expressed according to:

The molar flow balances,

$$\dot{n}_{\mathrm{CaCO_3},2} - \dot{n}_{\mathrm{SO_2},1} E_f - \dot{n}_{\mathrm{CaCO_3},7} = 0 \tag{6.2.7}$$

$$\dot{n}_{\mathrm{H_2O},1} + \dot{n}_{\mathrm{H_2O},2} + \dot{n}_{\mathrm{H_2O},6} - 2\dot{n}_{\mathrm{SO_2},1} E_f - \dot{n}_{\mathrm{H_2O},5} - \dot{n}_{\mathrm{H_2O},7} = 0 \tag{6.2.8}$$

The design equation,

$$\left(\frac{k_l k_r}{k_l + k_r}\right) SSAc_{\mathrm{CaCO_3},2}(1-X) MM_s \left(\left(10^{-pH}\right)^{\alpha} - 10^{-pH^{eq}}\right) V_{opt} - \dot{n}_{\mathrm{SO_2},1} E_f = 0 \tag{6.2.9}$$

The saturation condition with the three-term Antoine equation [Sinnott, 2005],

$$\frac{P_5 \dot{n}_{\mathrm{H_2O},5}}{\dot{n}_5} - \Phi \mathrm{e}^{A_{sat} - \frac{B_{sat}}{C_{sat}+T_5}} = 0 \tag{6.2.10}$$

The energy flow balance,

$$\sum \dot{H}_{m,in} - \sum \dot{H}_{m,out} - \Delta \dot{H}_{reaction} = 0 \tag{6.2.11}$$

where X corresponds to the conversion, V_{opt}, is the volume of the reaction tank, k_l is calculated by substituting equation (4.3.6) into equation (4.3.3). Furthermore, k_r is calculated by substituting the apparent activation energies and the pre-exponential factors obtained by the pH-stat method into equation (4.4.2). The enthalpies H_m of every stream, m, are calculated by integrating the polynomials of the heat capacities. The inequality constraints are expressed according to:

The residence time condition,

$$\tau - \frac{V_{opt}}{L + \dot{Q}_7} \leq 0 \tag{6.2.12}$$

The entropy flow balance,

$$\sum \dot{S}_{m,in} - \sum \dot{S}_{m,out} \leq 0 \tag{6.2.13}$$

The condition for minimum stirring speed,

$$\sqrt[3]{\frac{\varepsilon_{opt} V_{opt}}{5 N_{p,side} {D_{opt}}^5}} - N_{opt} \leq 0 \tag{6.2.14}$$

where ε_{opt} is the dissipated energy and it is estimated by combining the terminal velocity-slip velocity and Kolmogoroff's theories together. The settling velocity which is required for estimating ε_{opt} was calculated from equation (5.1.3). The Antoine parameters, the polynomials for the heat capacities, and the standard entropies where obtained from the literature [Sinnott, 2005], [Brewer, 1982].

In this work a local solver and a global solver were used to minimize the objective function according to equation (6.2.2). The "fmincon" function for constrained optimization featuring the "interior-point" algorithm was used in MATLAB. On the other hand, the ANTIGONE solver in GAMS was used as the global solver. The BARON solver was also implemented, but the convergence was much slower than ANTIGONE. The solution to the power consumption is presented in Table 6.2. The objective function has been plotted as a 3D surface in Figures 6.3 and 6.4 by fixing seven variables and changing two at a time. The minimum value for the unconstrained problem is obtained when moving towards larger particle diameters and lower stirring speeds in Figure 6.3.

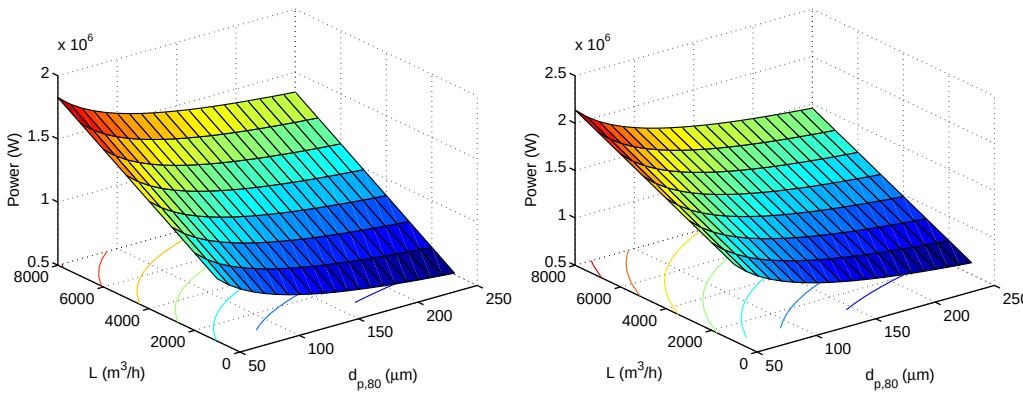

(a) Wolica **(b)** Parainen

Figure 6.4: Objective function for Wolica, and Parainen as a function of 2 variables: L and d_p, the remaining variables were kept constant.

A similar case is observed for Figure 6.4, where the best value is obtained by moving towards larger particle size and smaller flows for the recycled slurry.

The present NLP model is a nonconvex problem because of the existence of nonlinear equality constraints such as $h(\mathbf{x}) = 0$ [Biegler, 2010]. Therefore, as has been previously mentioned, the nonconvexity implies the possibility of finding a local solution. Nonetheless, the problem can be convexified by different convexification techniques, which allows for the problem to be solved globally. Hence, there was motivation to use a deterministic global optimization algorithm such as the one implemented in the ANTIGONE solver to guarantee a global solution. The local solver however, performs quite well for this problem as can be seen from the results presented in Table 6.2. A random initialization procedure was employed for the local solver by assessing whether the different (random) starting points would provide different feasible solutions. The criterion for terminating the algorithm was based on the number of iterations and the initial vector of variables was estimated according to,

$$\mathbf{x}^o = rand\left(\mathbf{x}^U - \mathbf{x}^L\right) + \mathbf{x}^L \tag{6.2.15}$$

where *rand* is a variable between 0 and 1. The behavior of the solution found for the objective function for both samples is presented in Figure 6.5. After only 100 iterations, the local solver was able to provide solutions which were worse with respect to the global solver only by 1% or below. Moreover, the choice of sample seems to complicate the solution of the problem as it can be seen in Figure 6.5. The solutions obtained by means of the random initialization procedure have been included as white stars in Figure 6.3. Moreover, as can be appreciated especially in the case of the Wolica sample, the local solver found feasible solutions which provided relatively poor values of the objective function. These solutions are given by higher values of (L), and it is for that reason that the solutions move within a vertical axis (z) without too much scattering in the x and y axes. On the other hand, as has been mentioned previously, the local solver identified

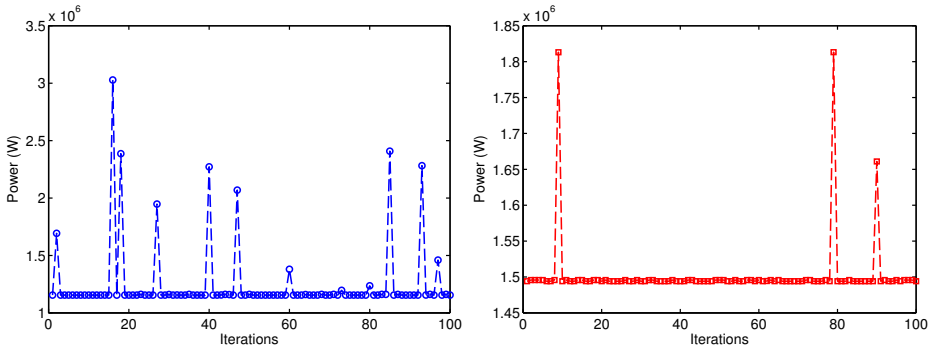

(a) Wolica **(b)** Parainen

Figure 6.5: Local solver solutions for 100 iteration, both samples.

the solution much faster for the Parainen sample, therefore the white points represented in Figure 6.3 (b) are closely grouped within one region.

CHAPTER 7

Conclusions

Limestone dissolution has been widely studied under a variety of topics, including Wet Flue Gas Desulfurization (WFGD). Nonetheless, some unanswered questions remain. The main objective of the present work was to revisit limestone dissolution by means of mathematical modeling based on detailed experimental and characterization information. The sample characterization was obtained by means of Nitrogen adsorption, particle size distribution, and ICP-OES. EDX supported the experimental results and served as a basis for the model development. A systematic experimental procedure was developed which allowed the performance of experiments in a regime which was not purely controlled by mass transfer. As a result of the procedures, a model that features a chemical reaction coupled with mass transfer was developed and successfully applied to a region of transient pH. In addition to which, a surface factor was introduced which allowed for the dynamic calculation of the specific surface area as a function of the concentration and with a correction for the non-sphericity of the samples. The obtained parameters, i.e. the apparent activation energies, concur with values presented previously in the literature and also indicate the possible formation of an electrical double layer which depends on the pH value. Further study of the change of zeta potential as a function of pH would thus be deemed to be highly valuable. The solid-liquid dynamics of dense systems like those present in the industrial WFGD scrubber were investigated. As a result, a modified Peclet number was introduced which was also adopted when comparing the model based on Fick's second law with chemical reaction and diffusion versus a two-step model featuring also forced convection. Furthermore, the parameters which were determined experimentally were employed in optimizing a case study of a WFGD scrubber in Finland. Moreover, the optimization results indicate that the systematic experimental approach and the application of a mathematical optimization model can help in understanding the performance of different raw-materials in the actual process. In addition, the results show how these different parameters can be adjusted as a function of a sample in order to minimize the power consumption of the process.

7.1 Contributions to the field of science

Based on this work, the mechanisms of diffusion can indeed limit limestone dissolution, as suggested by the results of **Paper II**. In that paper, experiments with very low stirring rates, i.e. $N<N_{js}$, presented mass transfer limitation. However, this behavior depends on the power input, stirring speed and reactor configurations. According to the results presented here, the limitations by diffusion do not depend solely on pH, which is an important remark. Another important aspect that is noteworthy, is that the use of SSA estimated through N_2 adsorption, provides values of the rate constant that are smaller than when implementing SSA estimated through PSD. This result is due to the fact that SSA estimated by N_2 adsorption is at least one order of magnitude larger than when employing only PSD values which assume smooth spherical surfaces. Furthermore, it has been stated that the mass transfer coefficient does not increase greatly for $N>N_{js}$, or that operating at N_{js} is enough for industrial purposes. The experimental part of this work showed that the rate depended on stirring up to $N>2N_{js}$. However, the optimization results confirmed that, from an operating point of view, it is necessary to operate at a stirring speed that maximizes the surface area exposed for reaction; given that the power consumed by stirring is proportional to N^3.

The following list summarizes the aspects that were considered after the literature review along with the proposed solutions and results of this work.

- pH has often been referred to as a variable used to indicate mass transfer or chemical reaction control. In this work, a regime that allowed to study kinetics where the rate of stirring did not affect significantly the dissolution rate was achieved, independently of the pH value. Furthermore, there was also experimental evidence shown by the SEM images supporting chemical reaction as the controlling mechanism.

- Diffusion has been pointed out as the limiting factor at low values of pH. As a result of this work it was found that diffusion can indeed be the limiting factor depending on the hydrodynamic conditions. On the other hand, in an industrial operation, convection mechanisms should be considered as well.

- In the literature, surface of reaction has been successfully modeled as smooth spherical particles, although, the SEM images show particle morphology to be irregular. In this work, a correction factor was introduced in order to account for the non-sphericity of the particles.

- The typical experimental conditions for limestone dissolution studies present dilute solid-liquid suspensions which could present a limitation when attempting to scale up of the process. In this work, dense solid-liquid suspensions as the one present in WFGD scrubbers were considered and investigated by process tomography.

- Little to few approaches in the literature were found that implemented deterministic or non-deterministic optimization models to improve the WFGD scrubber

performance. In this work a preliminary NLP model was developed and implemented.

7.2 Future work and recommendations

It has been stated previously, that the different grinding technologies produce pulverized samples with different surfaces and morphologies. Thus, this aspect should be investigated, in order to determine, the link between comminution and reaction rate. Furthermore, stochastic approaches could also be applied for modeling limestone dissolution.

The optimization can be developed further, for example by means of process synthesis approach:

- By including the nozzle configuration and the pump system
- By considering different types of comminution technologies such as ball mill, rolls crusher and hammer mill
- By developing a superstructure with different possible configurations of the process

The items mentioned above, would introduce integer variables which are more difficult to solve since the problem becomes a mixed integer non linear programming (MINLP) problem. The difficulty of solving MINLP problems, both convex and non convex, lays in the fact that these problems are combinatorial problems.

Bibliography

J. Ahlbeck, T. Engman, S. Fältén, and M. Vihma. A method for measuring the reactivity of absorbents for wet flue gas desulfurization. *Chemical Engineering Science*, 48(20):3479–3484, 1993. [15]

J. Ahlbeck, T. Engman, S. Fältén, and M. Vihma. Measuring the reactivity of limestone for wet flue-gas desulfurization. *Chemical Engineering Science*, 50(7):1081–1089, 1995. [16, 17]

M. Alkattan, E. H. Oelkers, J.-L. Dandurand, and J. Schott. An experimental study of calcite and limestone dissolution rates as a function of ph from- 1 to 3 and temperature from 25 to 80 °C. *Chemical Geology*, 151(1):199–214, 1998. [16, 45]

T. Allen. *Particle Size Measurement, Vol. 2*. Chapman & Hall, London, 1997. [28]

N. E. Altun. Assessment of marble waste utilization as an alternative sorbent to limestone for SO_2 control. *Fuel Processing Technology*, 128:461–470, 2014. [15]

L. G. Arnaut, S. J. Formosinho, and H. Burrows. *Chemical kinetics: from molecular structure to chemical reactivity*. Elsevier, Amsterdam, 2006. [16, 42]

V. A. Atiemo-Obeng, W. R. Penney, and P. Armeante. *Handbook of industrial mixing: science and practice*, chapter Solid-liquid mixing, pages 543–584. John Wiley & Sons, New Jersey, 2004. [31, 36, 37]

P. Barton and T. Vatanatham. Kinetics of limestone neutralization of acid waters. *Environmental Science & Technology*, 10(3):262–266, 1976. [14, 16]

R. A. Berner. Rate control of mineral dissolution under earth surface conditions. *American Journal of Science*, 278(9):1235–1252, 1978. [14, 34, 35]

L. T. Biegler. *Nonlinear programming: concepts, algorithms, and applications to chemical processes*, volume 10. SIAM, Philadelphia, 2010. [68]

R. B. Bird, W. E. Stewart, and E. N. Lightfoot. *Transport Phenomena, Revised Second Edition*. Wiley, New York, 2007. [36]

I. Bjerle and G. T. Rochelle. Limestone dissolution from a plane surface. *Chemical Engineering Science*, 39(1):183–185, 1984. [15]

D. L. Black, M. Q. McQuay, and M. P. Bonin. Laser-based techniques for particle-size measurement: a review of sizing methods and their industrial applications. *Progress in Energy and Combustion Science*, 22(3):267–306, 1996. [29]

G. T. Bolton and Ken M. Primrose. An overview of electrical tomographic measurements in pharmaceutical and related application areas. *AAPS PharmSciTech*, 6(2):E137–E143, 2005. [53]

S. Boon-Long, C. Laguerie, and J. P. Couderc. Mass transfer from suspended solids to a liquid in agitated vessels. *Chemical Engineering Science*, 33(7):813–819, 1978. [37]

S. Boyd and L. Vandenberghe. *Convex Optimization*. Cambridge university press, Cambridge, 2004. [62]

S. L. Brantley, J. D. Kubicki, and A. F. White. *Kinetics of water-rock interaction*, volume 168. Springer, New York, 2008. [48]

R. V. Bravo, R. F. Camacho, V. M. Moya, and L. A. I. García. Desulphurization of SO_2–N_2 mixtures by limestone slurries. *Chemical Engineering Science*, 57(11):2047–2058, 2002. [13]

L. Brewer. Thermodynamic values for desulfurization process. In *ACS Symp. Ser*, number 188, pages 1–39, 1982. [67]

C. Brogren and H. T. Karlsson. A model for prediction of limestone dissolution in wet flue gas desulfurization applications. *Industrial & Engineering Chemistry Research*, 36(9):3889–3897, 1997. [11, 66]

S. R. Brown, R. F. DeVault, and P. J. Williams. Determination of wet fgd limestone reactivity. *Electric Power*, 2010:1–8, 2010. [15]

S. Brunauer, P. H. Emmett, and E. Teller. Adsorption of gases in multimolecular layers. *Journal of the American Chemical Society*, 60(2):309–319, 1938. [26]

S. Builes, S. I. Sandler, and R. Xiong. Isosteric heats of gas and liquid adsorption. *Langmuir*, 29 (33):10416–10422, 2013. [44]

E. Busenberg and L. N. Plummer. A comparative study of the dissolution and crystal growth kinetics of calcite and aragonite. In *Studies in Diagenesis*, volume 1578, pages 139–168. US Geol. Surv. Bull, 1986. [14, 24, 32]

G. Buzzi-Ferraris and F. Manenti. Kinetic models analysis. *Chemical Engineering Science*, 64(5): 1061–1074, 2009. [42]

P. H. Calderbank and M. B. Moo-Young. The continuous phase heat and mass-transfer properties of dispersions. *Chemical Engineering Science*, 16(1):39–54, 1961. [38]

P. K. Chan and G. T. Rochelle. Limestone dissolution: effects of pH, CO_2 and buffers modeled by mass transfer. In *ACS Symp. Ser*, volume 188, pages 75–97, 1982. [15, 16, 18, 32]

H.-J. Chang. *Economics: the user's guide*. Bloomsbury Publishing USA, USA, 2014. [2]

B. Coto, C. Martos, J. L. Peña, R. Rodríguez, and G. Pastor. Effects in the solubility of $CaCO_3$: Experimental study and model description. *Fluid Phase Equilibria*, 324:1–7, 2012. [14]

J. Cristóbal, G. Guillén-Gosálbez, L. Jiménez, and A. Irabien. Optimization of global and local pollution control in electricity production from coal burning. *Applied Energy*, 92:369–378, 2012. [61]

M. E. Davis and R. J. Davis. *Fundamentals of Chemical Reaction Engineering*. Courier Corporation, Boston, 2012. [34]

C. De Blasio. *Reactive Dissolution of Sedimentary Rocks in Flue Gas Desulfurization. Modeling and Experimental Investigation.* PhD thesis, Process Design and Systems Engineering , Department of Chemical Engineering, Åbo Akademi University, 2010. [19, 40]

C. De Blasio, E. Mäkilä, and T. Westerlund. Use of carbonate rocks for flue gas desulfurization: Reactive dissolution of limestone particles. *Applied Energy*, 90(1):175–181, 2012. [15, 26, 32]

C. De Blasio, C. Carletti, T. Westerlund, and M. Järvinen. On modeling the dissolution of sedimentary rocks in acidic environments. an overview of selected mathematical methods with presentation of a case study. *Journal of Mathematical Chemistry*, 51(8):2120–2143, 2013. [36]

K. D. Demadis, Z. Anagnostou, and H. Zhao. Novel calcium carboxyphosphonate/polycarboxylate inorganic- organic hybrid materials from demineralization of calcitic biomineral surfaces. *ACS Applied Materials & Interfaces*, 1(1):35–38, 2008. [14]

F. Dickin and M. Wang. Electrical resistance tomography for process applications. *Measurement Science and Technology*, 7(3):247, 1996. [54]

B. Dou, W. Pan, Q. Jin, W. Wang, and Y. Li. Prediction of SO_2 removal efficiency for wet flue gas desulfurization. *Energy Conversion and Management*, 50(10):2547–2553, 2009. [11, 63]

M. A. Duran and I. E. Grossmann. An outer-approximation algorithm for a class of mixed-integer nonlinear programs. *Mathematical Programming*, 36(3):307–339, 1986. [63]

D. Eden and M. Luckas. A heat and mass transfer model for the simulation of the wet limestone flue gas scrubbing process. *Chemical Engineering Technology*, 21(1):56–60, 1998. [15, 35, 36, 66]

C. Fischer, R. S. Arvidson, and A. Lüttge. How predictable are dissolution rates of crystalline material? *Geochimica et Cosmochimica Acta*, 98:177–185, 2012. [14]

A. Franco and A. R. Diaz. The future challenges for “clean coal technologies": joining efficiency increase and pollutant emission control. *Energy*, 34(3):348–354, 2009. [1]

J. B. W. Frandsen, S. Kiil, and J. E. Johnsson. Optimisation of a wet fgd pilot plant using fine limestone and organic acids. *Chemical Engineering Science*, 56(10):3275–3287, 2001. [15, 61]

L. Fusi, A. Monti, and M. Primicerio. Determining calcium carbonate neutralization kinetics from experimental laboratory data. *Journal of Mathematical Chemistry*, 50(9):2492–2511, 2012. [16]

C. L. Gage and G. T. Rochelle. Limestone dissolution in flue gas scrubbing: effect of sulfite. *Journal of the Air & Waste Management Association*, 42(7):926–935, 1992. [15, 32, 38]

M. Gautelier, E. H. Oelkers, and J. Schott. An experimental study of dolomite dissolution rates as a function of ph from- 0.5 to 5 and temperature from 25 to 80 °C. *Chemical Geology*, 157(1): 13–26, 1999. [16]

P. K. Gbor and C. Q. Jia. Critical evaluation of coupling particle size distribution with the shrinking core model. *Chemical Engineering Science*, 59(10):1979–1987, 2004. [27]

M. Gerbec, A. Stergaršek, and R. Kocjančič. Simulation model of wet flue gas desulphurization plant. *Computers & Chemical Engineering*, 19:283–286, 1995. [63]

O. Gibert, J. de Pablo, J. Luis Cortina, and C. Ayora. Evaluation of municipal compost/limestone/-iron mixtures as filling material for permeable reactive barriers for in-situ acid mine drainage treatment. *Journal of Chemical Technology and Biotechnology*, 78(5):489–496, 2003. [14]

D. Gidaspow. *Multiphase flow and fluidization: continuum and kinetic theory descriptions*. Academic press, San Diego, 1994. [52]

R. Gill. *Modern Analytical Geochemistry: an introduction to quantitative chemical analysis techniques for Earth, environmental and materials scientists*, chapter Electron beam methods, pages 215–234. Routledge, Harlow, 1997. [20, 22]

D. K. Gledhill and J. W. Morse. Calcite dissolution kinetics in Na–Ca–Mg–Cl brines. *Geochimica et Cosmochimica Acta*, 70(23):5802–5813, 2006. [16, 45]

A. Gómez, N. Fueyo, and A. Tomás. Detailed modelling of a flue-gas desulfurisation plant. *Computers & Chemical Engineering*, 31(11):1419–1431, 2007. [63]

H. Grénman. *Solid-liquid reaction kinetics. Experimental aspects and model development*. PhD thesis, Laboratory of Industrial Chemistry and Reaction Engineering , Department of Chemical Engineering, Åbo Akademi University, 2010. [42]

H. Grénman, M. Ingves, J. Wärnå, J. Corander, D. Yu Murzin, and T. Salmi. Common potholes in modeling solid–liquid reactions–methods for avoiding them. *Chemical Engineering Science*, 66 (20):4459–4467, 2011. [31, 47]

S. M. A. Guelli U. Souza, F. B. F. Santos, A. A. Ulson de Souza, and F. Vidal Barrero. Limestone dissolution in flue gas desulfurizationŮexperimental and numerical study. *Journal of Chemical Technology and Biotechnology*, 85(9):1208–1214, 2010. [9]

F. J. Gutiérrez Ortiz, F. Vidal, P. Ollero, L. Salvador, V. Cortés, and A. Gimenez. Pilot-plant technical assessment of wet flue gas desulfurization using limestone. *Industrial & Engineering Chemistry Research*, 45(4):1466–1477, 2006. [9, 12, 61, 64, 65]

J. Hajek and D. Yu Murzin. Liquid-phase hydrogenation of cinnamaldehyde over a ru-sn sol-gel catalyst. 1. evaluation of mass transfer via a combined experimental/theoretical approach. *Industrial & Engineering Chemistry Research*, 43(9):2030–2038, 2004. [36, 65]

S. T. L. Harrison, R. Stevenson, and J. J. Cilliers. Assessing solids concentration homogeneity in rushton-agitated slurry reactors using electrical resistance tomography (ERT). *Chemical Engineering Science*, 71:392–399, 2012. [53, 55, 57]

P. J. Holden, M. Wang, R. Mann, F. J. Dickin, and R. B. Edwards. Imaging stirred-vessel macromixing using electrical resistance tomography. *American Institute of Chemical Engineers. AIChE Journal*, 44(4):780, 1998. [54]

S. Hosseini, D. Patel, F. Ein-Mozaffari, and M. Mehrvar. Study of solid–liquid mixing in agitated tanks through electrical resistance tomography. *Chemical Engineering Science*, 65(4):1374–1384, 2010. [53, 55, 56, 57]

C. Hoşten and M. Gülsün. Reactivity of limestones from different sources in turkey. *Minerals engineering*, 17(1):97–99, 2004. [15, 24]

I. Hrastel, M. Gerbec, and A. Stergaršek. Technology optimization of wet flue gas desulfurization process. *Chemical Engineering & Technology*, 30(2):220–233, 2007. [3, 9, 61]

C.-T. Hsieh, W.-S. Fan, and W.-Y. Chen. Impact of mesoporous pore distribution on adsorption of methylene blue onto titania nanotubes in aqueous solution. *Microporous and Mesoporous Materials*, 116(1):677–683, 2008. [44]

S. Ibrahim and A. W. Nienow. Power curves and flow patterns for a range of impellers in newtonian fluids-40-less-than-re-less-than-5x10 (5). *Chemical Engineering Research & Design*, 73(5):485–491, 1995. [37, 38]

R. Jafari, P. A. Tanguy, and J. Chaouki. Characterization of minimum impeller speed for suspension of solids in liquid at high solid concentration, using gamma-ray densitometry. *International Journal of Chemical Engineering*, 2012:1–15, 2012. [52, 53]

L. Järvinen. *Surface studies of limestones and dolostones: characterisation using various techniques and batch dissolution experiments with hydrochloric acid solutions*. PhD thesis, Geology and Mineralogy, Faculty of Science and Engineering, Åbo Akademi University, 2015. [15, 19, 21]

L. Järvinen, J. A. Leiro, F. Bjondahl, C. Carletti, and O. Eklund. XPS and SEM study of calcite bearing rock powders in the case of reactivity measurement with hcl solution. *Surface and Interface Analysis*, 44(5):519–528, 2012. [19, 20, 24]

L. Järvinen, J. Leiro, F. Bjondahl, C. Carletti, T. Lundin, K. Gunnelius, J.-H. Smått, and O. Eklund. Characterisation of dolomites before and after reactivity measurement with hcl solution. *Surface and Interface Analysis*, 47(2):284–294, 2015. [20]

M. Kagoshima and R. Mann. Interactions of precipitation and fluid mixing with model validation by electrical tomography. *Chemical Engineering Research and Design*, 83(7):806–810, 2005. [54]

J. Kaminski. Technologies and costs of SO_2–emissions reduction for the energy sector. *Applied Energy*, 75(3):165–172, 2003. [9]

J. Karelahti, P. Vainiomäki, and T. Westerlund. Large scale production planning in the stainless steel industry. *Industrial & Engineering Chemistry Research*, 50(9):4893–4906, 2011. [61]

K. I. Keskinen, V. Alopaeus, J. Koskinen, T. Kinnunen, H. Pitkänen, J. Majander, and U. Wärnström. Cfd simulation of the oxidation tank reactor of a wet flue gas desulfurization process. In *2002 AIChe Annual Meeting, Indianapolis, IN*, 2002. [63]

S. Kiil, M. L. Michelsen, and K. Dam-Johansen. Experimental investigation and modeling of a wet flue gas desulfurization pilot plant. *Industrial & Engineering Chemistry Research*, 37(7): 2792–2806, 1998. [15]

C. V. King and C. L. Liu. The rate of solution of marble in dilute acids. *Journal of the American Chemical Society*, 55(5):1928–1940, 1933. [16]

C. J. Kotre. A sensitivity coefficient method for the reconstruction of electrical impedance tomograms. *Clinical Physics and Physiological Measurement*, 10(3):275, 1989. [53]

A. Lancia, D. Musmarra, and F. Pepe. Mass transfer between a fixed bed of limestone particles and acid solutions. *Industrial & Engineering Chemistry Research*, 36(9):3859–3865, 1997. [15]

D. Langmuir. Stability of calcite based on aqueous solubility measurements. *Geochimica et Cosmochimica Acta*, 32(8):835–851, 1968. [14]

J. R. Leis and M. A. Kramer. Algorithm 658: Odessa–an ordinary differential equation solver with explicit simultaneous sensitivity analysis. *ACM Transactions on Mathematical Software (TOMS)*, 14(1):61–67, 1988. [44]

O. Levenspiel. *Chemical Reaction Engineering, 1999*. JohnWiley, NewYork, New York, 1999. [15, 22]

D. M. Levins and J. R. Glastonbury. Application of kolmogorofff's theory to particleŮliquid mass transfer in agitated vessels. *Chemical Engineering Science*, 27(3):537–543, 1972. [36, 37]

Z. Liu and W. Dreybrod. Dissolution kinetics of calcium carbonate minerals in H_2O–CO_2 solutions in turbulent flow: The role of the diffusion boundary layer and the slow reaction $H_2O + CO_2 = H^+ + HCO_3^-$. *Geochimica et Cosmochimica Acta*, 61(14):2879–2889, 1997. [38]

K. Lund, H. S. Fogler, and C. C. McCune. Acidization–I. the dissolution of dolomite in hydrochloric acid. *Chemical Engineering Science*, 28(3):691–IN1, 1973. [14, 24]

A. Lundell. *Transformation Techniques for Signomial Functions in Global Optimization*. PhD thesis, Department of Mathematics, Åbo Akademi University, 2009. [62, 63]

Andreas Lüttge, Rolf S Arvidson, and Cornelius Fischer. A stochastic treatment of crystal dissolution kinetics. *Elements*, 9(3):183–188, 2013. [14]

I. N. MacInnis and S. L. Brantley. The role of dislocations and surface morphology in calcite dissolution. *Geochimica et Cosmochimica Acta*, 56(3):1113–1126, 1992. [14, 44]

S. E. Manahan. *Environment Chemistry*. CRC Press LLC, New York, seventh edition, 1999. [2]

R. Mann, F. J. Dickin, M. Wang, T. Dyakowski, R. A. Williams, R. B. Edwards, A. E. Forrest, and P. J. Holden. Application of electrical resistance tomography to interrogate mixing processes at plant scale. *Chemical Engineering Science*, 52(13):2087–2097, 1997. [53]

R. Mann, S. Stanley, D. Vlaev, E. Wabo, and K. Primrose. Augmented-reality visualization of fluid mixing in stirred chemical reactors using electrical resistance tomography. *Journal of Electronic Imaging*, 10(3):620–629, 2001. [53, 54]

S. L. McKee, R. A. Williams, and A. Boxman. Development of solid–liquid mixing models using tomographic techniques. *The Chemical Engineering Journal and The Biochemical Engineering Journal*, 56(3):101–107, 1995. [56]

R. Misener and C. A. Floudas. Antigone: algorithms for continuous/integer global optimization of nonlinear equations. *Journal of Global Optimization*, 59(2-3):503–526, 2014. [63]

G. Montante and A. Paglianti. Gas hold-up distribution and mixing time in gas-liquid stirred tanks. *Chemical Engineering Journal*, 279:648–658, 2015. [53]

G. Montante, A. Paglianti, and F. Magelli. Analysis of dilute solid–liquid suspensions in turbulent stirred tanks. *Chemical Engineering Research and Design*, 90(10):1448–1456, 2012. [53]

J. W. Morse. Dissolution kinetics of calcium carbonate in sea water; III, a new method for the study of carbonate reaction kinetics. *American Journal of Science*, 274(2):97–107, 1974. [15, 18]

J. W. Morse and R. S. Arvidson. The dissolution kinetics of major sedimentary carbonate minerals. *Earth-Science Reviews*, 58(1):51–84, 2002. [14, 16]

J. W. Morse, R. S. Arvidson, and A. Lüttge. Calcium carbonate formation and dissolution. *Chemical Reviews*, 107(2):342–381, 2007. [14]

P. Moulin and H. Roques. Zeta potential measurement of calcium carbonate. *Journal of Colloid and Interface Science*, 261(1):115–126, 2003. [45, 46]

A. W. Nienow. Agitated vessel particle-liquid mass transfer: a comparison between theories and data. *The Chemical Engineering Journal*, 9(2):153–160, 1975. [37]

A. W. Nienow. *Mixing in the process industries*, chapter The mixer as a reactor: liquid/solid systems, pages 394–410. Butterworth-Heinemann, Oxford, 1992. [34, 37, 38]

K. E. Noll, Gounaris V., and Wain-Sun H. *Adsorption technology for air and water pollution control*. CRC Press, Chelsea, Michigan, 1991. [26, 43]

S. Olausson, M. Wallin, and I. Bjerle. A model for the absorption of sulphur dioxide into a limestone slurry. *The Chemical Engineering Journal*, 51(2):99–108, 1993. [11, 63, 65]

F. Pepe. Dissolution of finely ground limestone particles in acidic solutions. *Industrial & Engineering Chemistry Research*, 40(23):5378–5385, 2001. [15, 16, 36]

T. D. Perry IV, O. W. Duckworth, T. A. Kendall, S. T. Martin, and R. Mitchell. Chelating ligand alters the microscopic mechanism of mineral dissolution. *Journal of the American Chemical Society*, 127(16):5744–5745, 2005. [14]

L. N. Plummer and E. Busenberg. The solubilities of calcite, aragonite and vaterite in CO_2–H_2O solutions between 0 and 90 °C, and an evaluation of the aqueous model for the system $CaCO_3$–CO_2–H_2O. *Geochimica et Cosmochimica Acta*, 46(6):1011–1040, 1982. [14, 17]

L. N. Plummer, T. M. L. Wigley, and D. L. Parkhurst. The kinetics of calcite dissolution in CO_2–water systems at 5 degrees to 60 degrees C and 0.0 to 1.0 atm CO_2. *American Journal of Science*, 278(2):179–216, 1978. [14, 15, 16, 32, 47]

M. J. Rhodes. *Introduction to particle technology*. John Wiley & Sons, Norfolk, U.K., 1998. [28, 65]

F. Ricard, C. Brechtelsbauer, Y. Xu, C. Lawrence, and D. Thompson. Development of an electrical resistance tomography reactor for pharmaceutical processes. *The Canadian Journal of Chemical Engineering*, 83(1):11–18, 2005a. [53]

F. Ricard, C. Brechtelsbauer, X. Y. Xu, and C. J. Lawrence. Monitoring of multiphase pharmaceutical processes using electrical resistance tomography. *Chemical Engineering Research and Design*, 83 (7):794–805, 2005b. [53, 56]

E. Ruiz-Agudo, C. V. Putnis, C. Jiménez-López, and C. Rodriguez-Navarro. An atomic force microscopy study of calcite dissolution in saline solutions: the role of magnesium ions. *Geochimica et Cosmochimica Acta*, 73(11):3201–3217, 2009. [15]

T. Salmi, H. Grénman, J. Wärnå, and D. Yu Murzin. Revisiting shrinking particle and product layer models for fluid–solid reactions–from ideal surfaces to real surfaces. *Chemical Engineering and Processing: Process Intensification*, 50(10):1076–1084, 2011. [36, 37]

T. Salmi, H. Grénman, J. Wärnå, and D. Yu Murzin. New modelling approach to liquid–solid reaction kinetics: From ideal particles to real particles. *Chemical Engineering Research and Design*, 91(10):1876–1889, 2013. [31]

L. Schiller and A. Naumann. Über die grundlegenden berechnungen bei der schwerkraftaufbereitung. *Z. Ver. Dtsch. Ing*, 77(12):318–320, 1933. [51]

J. Schott, E. H. Oelkers, P. Bénézeth, Y. Goddéris, and L. François. Can accurate kinetic laws be created to describe chemical weathering? *Comptes Rendus Geoscience*, 344(11):568–585, 2012. [15]

J. H. Seinfeld. *Atmospheric chemistry and physics of Air Pollution*. John Wiley & Sons, USA, 1986. [2]

S. Shafiee and E. Topal. An econometrics view of worldwide fossil fuel consumption and the role of us. *Energy Policy*, 36(2):775–786, 2008. [1, 2]

S.-M. Shih, J.-P. Lin, and G.-Y. Shiau. Dissolution rates of limestones of different sources. *Journal of Hazardous Materials*, 79(1):159–171, 2000. [15, 17, 32]

Z. O. Siagi and M. Mbarawa. Dissolution rate of south african calcium-based materials at constant ph. *Journal of hazardous materials*, 163(2):678–682, 2009. [15, 32]

K. Sing. The use of nitrogen adsorption for the characterisation of porous materials. *Colloids and Surfaces A: Physicochemical and Engineering Aspects*, 187:3–9, 2001. [26]

K. S. W. Sing. Reporting physisorption data for gas/solid systems with special reference to the determination of surface area and porosity (recommendations 1984). *Pure and applied chemistry*, 57(4):603–619, 1985. [26, 28, 47]

R. K. Sinnott. *Coulson & Richardson's chemical engineering, vol. 6*, volume 6. Elsevier, 2005. [66, 67]

E. L. Sjöberg. A fundamental equation for calcite dissolution kinetics. *Geochimica et Cosmochimica Acta*, 40(4):441–447, 1976. [16]

E. L. Sjöberg and D. Rickard. The influence of experimental design on the rate of calcite dissolution. *Geochimica et Cosmochimica Acta*, 47(12):2281–2285, 1983. [16, 18]

E. L. Sjöberg and D. T. Rickard. Calcite dissolution kinetics: surface speciation and the origin of the variable ph dependence. *Chemical Geology*, 42(1):119–136, 1984a. [17]

E. L. Sjöberg and D. T. Rickard. Temperature dependence of calcite dissolution kinetics between 1 and 62 °C at pH 2.7 to 8.4 in aqueous solutions. *Geochimica et Cosmochimica Acta*, 48(3): 485–493, 1984b. [16, 38, 45]

E. L. Sjöberg and D. T. Rickard. The effect of added dissolved calcium on calcite dissolution kinetics in aqueous solutions at 25 °C. *Chemical Geology*, 49(4):405–413, 1985. [15, 44]

A. Skjäl. *On the Use of Convex Underestmiunder in Global Optimization*. PhD thesis, Department of Natural Sciences, Åbo Akademi University, 2014. [63]

R. K. Srivastava, W. Jozewicz, and C. Singer. SO_2 scrubbing technologies: a review. *Environmental Progress*, 20(4):219–228, 2001. [3]

S. J. Stanley. Tomographic imaging during reactive precipitation in a stirred vessel: Mixing with chemical reaction. *Chemical Engineering Science*, 61(24):7850–7863, 2006. [54, 55]

S. C. Stultz and J. B. Kitto. *Steam: its generation and use*. Babcock & Wilcox, Barberton, Ohio, 2005. [1, 2, 3, 12, 13, 65]

B. Sun, Q. Zhou, X. Chen, T. Xu, and S. Hui. Effect of particle size in a limestone–hydrochloric acid reaction system. *Journal of Hazardous Materials*, 179(1):400–408, 2010. [15, 27]

A. Tamburini, A. Cipollina, G. Micale, A. Brucato, and M. Ciofalo. CFD prediction of solid particle distribution in baffled stirred vessels under partial to complete suspension conditions. *Chem. Eng. Trans*, 32:1447–1452, 2013. [41]

F. W. Tegethoff, J. Rohleder, and E. Kroker. *Calcium carbonate: from the Cretaceous period into the 21st century*. Springer Science & Business Media, Berlin, 2001. [10, 11]

M. I. Temkin. Transfer of dissolved matter between a turbulently moving liquid and particles suspended in it. *Kinetika i Kataliz*, 18:493–496, 1977. [36, 38]

A. J. Toprac and G. T. Rochelle. Limestone dissolution in stack gas desulfurization. a mass-transfer model is shown to predict the the measured dissolution rates with less than 30% error. *Environmental Progress*, 1(1):52–58, 1982. [15, 18, 27]

N Ukawa, T. Takashina, N. Shinoda, and T. Shimizu. Effects of particle size distribution on limestone dissolution in wet fgd process applications. *Environmental Progress*, 12(3):238–242, 1993. [3, 15, 27]

V. Vestreng, G. Myhre, H. Fagerli, S. Reis, and L. Tarrasón. Twenty-five years of continuous sulphur dioxide emission reduction in europe. *Atmospheric Chemistry and Physics*, 7(13):3663–3681, 2007. [2, 3]

M. Wallin and I. Bjerle. A mass transfer model for limestone dissolution from a rotating cylinder. *Chemical Engineering Science*, 44(1):61–67, 1989. [15]

F. N. Walsh. *Modern Analytical Geochemistry: an introduction to quantitative chemical analysis techniques for Earth, Environmental and Materials Scientists*, chapter Inductively coupled plasma-atomic emission spectrometry (ICP-AES), pages 41–66. Routledge, Harlow, 1997. [25]

M. Wang, F. J. Dickin, and R. Mann. Electrical resistance tomographic sensing systems for industrial applications. *Chemical Engineering Communications*, 175(1):49–70, 1999. [55]

J. Warych and M. Szymanowski. Model of the wet limestone flue gas desulfurization process for cost optimization. *Industrial & Engineering Chemistry Research*, 40(12):2597–2605, 2001. [61, 63]

J. Welty, Gregory L. Rorrer, and D. G. Foster. *Fundamentals of Momentum, Heat and Mass Transfer*. Wiley Global Education, New York, 2014. [15, 35, 36, 41]

T. Westerlund and F. Pettersson. An extended cutting plane method for solving convex minlp problems. *Computers & Chemical Engineering*, 19:131–136, 1995. [63]

T. Westerlund, F. Pettersson, and I. E. Grossmann. Optimization of pump configurations as a minlp problem. *Computers & Chemical Engineering*, 18(9):845–858, 1994. [61]

B. B. Williams, J. L. Gidley, J. A. Guin, and R. S. Schechter. Characterization of liquid-solid reactions. hydrochloric acid-calcium carbonate reaction. *Industrial & Engineering Chemistry Fundamentals*, 9(4):589–596, 1970. [14, 15]

R. A. Williams. Tomographic imaging for modelling and control of mineral processes. *The Chemical Engineering Journal and The Biochemical Engineering Journal*, 59(1):71–85, 1995. [53, 56]

R. A. Williams, X. Jia, and S. L. McKee. Development of slurry mixing models using resistance tomography. *Powder Technology*, 87(1):21–27, 1996. [56]

G. Xiang, G. Rui-tang, D. Hong-lei, L. Zhong-yang, and C. Ke-fa. Dissolution rate of limestone for wet flue gas desulfurization in the presence of sulfite. *Journal of Hazardous Materials*, 168(2): 1059–1064, 2009. [15, 16]

Z. Ye and I. Bjerle. A numerical method for determination of particle size distribution of limestone based on ph-stat measurement. *Powder Technology*, 79(3):273–277, 1994. [27, 34]

Y. Zhong, X. Gao, Wang H., Z.-Y. Luo, M.-J. Ni, and K.-F. Cen. A model for performance optimization of wet flue gas desulfurization systems of power plants. *Fuel Processing Technology*, 89(11): 1025–1032, 2008. [11, 61, 63, 66]

J. Zhu, S.-C. Ye, J. Bai, Z.-Y. Wu, Z.-H. Liu, and Y.-F. Yang. A concise algorithm for calculating absorption height in spray tower for wet limestone–gypsum flue gas desulfurization. *Fuel Processing Technology*, 129:15–23, 2015. [36, 66]

T. N. Zwietering. Suspending of solid particles in liquid by agitators. *Chemical Engineering Science*, 8(3):244–253, 1958. [38, 52, 53]

Appendices

Notation

Variables and parameters

A : surface area of reaction (m^2)
A_{sat}, B_{sat}, C_{sat} : parameters of the Antoine equation
a : dimensionless coefficient, Sherwood equation
b : dimensionless constant for calculating the relative axial dispersion coefficient
c : concentration (mol/L)
c_{exp} : experimental concentration (mol/L)
c_{est} : estimated concentration (mol/L)
$c_{Ca^{2+}}$: calcium ion concentration in the bulk (mol/L)
$c_{CO_3^{2-}}$: carbonate ion concentration, at the solid-liquid interface (mol/L)
$c^*_{H^+}$: dimensionless concentration
c_{H^+} : hydronium ion concentration (mol/L)
$c_{HCO_3^-}$: bicarbonate ion concentration (mol/L)
c_s : solid concentration (mol/L)
C_D : drag coefficient
C_{eq} : pseudo equilibrium constant
D_s : impeller diameter (m)
D_{es} axial dispersion coefficient
D_j : mass diffusivity of species j (m^2)
D_{opt} : impeller diameter, optimization (m)
$d_{f,80}$: particle diameter for which 80% of the feed is finer (μm)
d_p : particle diameter (μm)
$d_{p,80}$: diameter for which 80% of the product is finer (μmm)
Ea : apparent activation energy (kJ/mol)
E_f : removal efficiency
E_r : energy required for particle suspension (J/m^3)
F : cumulative density function
g : acceleration of gravity (m^2/s)
$\dot{H}_m$: enthalpy flow of stream m (kJ/h)
H_L : height of liquid (m)
k_l : liquid phase mass transfer coefficient (m/s)
k_r : chemical reaction constant (L/m^2s)
k_{tot} : total rate constant (L/m^2s)
k''_{tot} : Langmuir model total rate constant (L/m^2s)
k_I : pre-exponential factor (L/m^2s)

K_{eq} : equilibrium constant (mol/L)
K_{ad} : adsorption constant (L/mol)
L : recycled slurry flow rate (m^3/h)
$\dot{m}$: mass flow (kg/h)
MM : molar mass (g/mol)
MI_m : overall mixing index
MI_tot : total mixing index
MI_v : volumetric mixing index
MI_z : mixing index per plane
$\dot{n}$: molar flow (kmol/h)
n : number of pixels in the plane
N : stirring speed (1/s)
N_j : flux of species m (mol/m^2 s)
N_{js} : stirring speed for the just suspended condition
N_{opt} : stirring speed, optimization (rpm)
$N_{settling}$: stirring speed for particle settling, optimization (1/s)
N_p : power number
$N_{p,side}$: power number, optimization
N_s : shape factor
p : variable of the Laplace space
Pa : Peclet number
$Pe*$: modified Peclet number
P_{unit} : power consumed in evry unit, i.e. milling stirring, pumping (W)
q : number of planes
Q : residual sum of squares
$\dot{Q}_{in}$: inlet volume flow (L/s)
$\dot{Q}_{outlet}$: outlet volume flow (L/s)
r : spatial dimension
$rand$: random variable
Re_p : Reynolds number of the particles
Re_v : Reynolds number for the vessel
R : radius of the particle (m)
R_g : universal gas constant (J/mol K)
S : parameter for the Zwietering correlation
SA : surface area per volume (m^2/L)
$\dot{S}_m$: entropy flow of stream m (kJ/K h)
Sc : Schmidt number
S_f : surface factor
$S_{f,o}$: surface factor for the initial condition
Sh : Sherwood number
SA : surface area available for reaction (m^2/L)
SSA_{BET} : specific surface area measured by nitrogen adsorption (m^2/g)
SSA_{PSD} = specific surface area measured by particle size distribution (m^2/g)
SSA_{real} =specific surface area of real particle (m^2/g)
t : time (s)
T : temperature (°C)
T_{mean} : reference mean temperature of the modified Arrhenius equation (K)

u : new variable in the variable change $u = c_{H^+} e^{k_r t}$
u_t : particle terminal settling velocity (m/s)
$\bar{u}$: the introduced variable change in the Laplace domain, second law of Fick
v : adsorbed weight, BET equation
v_m : weight of monolayer adsorbed gas, BET equation
v_s : particle volume
V : reactor volume (L)
V_{opt} : reactor volume (m^3)
X : conversion
X_v : volumetric solid fraction
$X_m ass$: solid fraction (mass)
W_I : Bond work index (kWh(μm)1/2/short ton)
$\mathbf{x}$: vector of optimization variables
y_{SO_2} : SO_2 composition in the stream
z : spatial dimension, Fick equation
z_i : fraction of particles of size i

Indexes

i : sub-index, size class, plane
in : sub-index
j : sub-index, species index
k : sub-index, variable index, pixel
L : super-index, lower bound
m : sub-index, stream number, 1,2,. . . ,7
o : sub-index, initial values
o : super-index, value at the interface
out : sub-index
U : super-index, upper bound

Greek letters

α : power for the reaction rate equation
γ : stoichiometric parameter 1.647
δ : diffusion boundary layer thickness (m)
δh: slurry height (m)
ΔH_{ad} : heat of adsorption (kJ/Kmol)
$\Delta H_{reaction}$: enthalpy of reaction (kJ/h)
ΔP : pressure loss (kPa)
ε : mean dissipated energy (W/kg)
ε_{opt} : mean dissipated energy, optimization (W/kg)
Θ_{H^+} : surface coverage of H^+
ρ = density of stream (kg/m3)
σ_1 : parameter of the Normal distribution, variance = σ_1^2
σ_2 : parameter of the Log-normal distribution

σ_{BET} : the effectively occupied area in the complete monolayer
σ_l : liquid conductivity
σ_m slurry conductivity
$\overline{\sigma}$: mean conductivity averaged over the whole volume
$\overline{\sigma_i}$: mean conductivity averaged over the plane i
σ_k : conductivity of the pixel k
λ : constant for the analytical solution of the ODE system (L/mol s)
μ_1 : parameter of the Normal distribution, mean
μ_2 : parameter of the Log-normal distribution
ν : kinematic viscosity of the liquid (m^2/s)
Φ : relative humidity
φ : volumetric fraction of solids
η : pump efficiency
τ : residence time (h)
ζ : zeta potential (mV)

ISBN 978-952-12-3281-7

Painosalama Oy
Åbo 2015